ICFO – Institut de Ciències Fotòniques

UPC – Universitat Politècnica de Catalunya

Transparent surfaces based on ultrathin materials with tailored optical and biological functionalities

Christina Graham

Thesis advisor: Prof. Valerio Pruneri

PhD Thesis- 2023

ABSTRACT

The properties of ultrathin materials present exciting opportunities to develop multifunctional surfaces. In addition, the use of plastic and thin glass as transparent substrates has the potential to extend the use of ultrathin materials beyond conventional substrates and provide vital advancements to existing and emerging technologies across a wide range of sectors. One of the main challenges facing next-generation transparent substrates is the substantially reduced temperature processing window which is not compatible with materials requiring high fabrication temperatures. This thesis describes the development of fabrication techniques to obtain ultrathin materials on low thermal budget transparent substrates to create surfaces with advanced optical and biological functionalities. More specifically, this thesis describes:

- A novel, low temperature transfer technique onto flexible substrates for ultrathin materials such as graphene, MoS_2 and nanostructured metals that were previously grown at a much higher temperature. The universality of the method extends the use of these ultrathin materials to a wide range of technologically relevant substrates such as cover glass for display modules and polymeric substrates for next generation foldable and bendable electronics.
- A novel approach to naturally increase electrical conductivity of transparent surfaces based on graphene, without the need of post-treatment, electrical gating or high temperatures. Notably, the method achieves a conductivity of comparable magnitude or greater than what is reported in previous studies. Furthermore, the increase in electrical conductivity is realised simply by utilizing an ion-exchanged substrate, a technologically relevant transparent glass substrate that is widely used in touch screen displays (e.g. smart phones).
- A low temperature metal dewetting technique to obtain transparent antimicrobial nanostructured coatings on a cover

glass substrate for display modules. The durability of the coatings was evaluated under conditions designed to simulate real-world use cases such as capacitive touch displays. The results show that the coatings were capable of substantially retaining optical properties of the underlying substrate, such as haze, neutral colour, and visible light transmission, as well as retaining antimicrobial properties after repeated contact with external objects such as, for example, when wiping with a towel or cloth, or touching with human fingers.

The results of this thesis demonstrate the implementation of ultrathin and nanostructured materials, such as graphene and nanostructured metals onto a wide range of technologically relevant transparent substrates, by methods that are industrially scalable and compatible with low temperature processing. At the same time, surfaces are engineered with advanced optical and biological functionalities that are relevant for applications such as transparent electrodes and antimicrobial coatings.

RESUMEN

Les propietats dels materials ultratins presenten oportunitats interessants per desenvolupar superfícies multifuncionals. A més, l'ús de plàstic i vidre fi com a substrats transparents té el potencial d'estendre l'ús de materials ultrafins més enllà dels substrats convencionals i proporcionar avenços vitals a les tecnologies existents i emergents en una àmplia gamma de sectors. Un dels principals reptes als quals s'enfronten els substrats transparents de nova generació és la finestra de processament de temperatura substancialment reduïda que no és compatible amb els materials que requereixen altes temperatures de fabricació. Aquesta tesi descriu el desenvolupament de tècniques de fabricació per obtenir materials ultrafins en substrats transparents de baix pressupost tèrmic per crear superfícies amb funcionalitats òptiques i biològiques avançades. Més concretament, aquesta tesi descriu:

- Una nova tècnica de transferència de baixa temperatura en substrats flexibles per a materials ultraprims com el grafè, MoS_2 i metalls nanoestructurats que anteriorment es conreaven a una temperatura molt més alta. La universalitat del mètode estén l'ús d'aquests materials ultratins a una àmplia gamma de substrats tecnològicament rellevants com el vidre de coberta per a mòduls de visualització i substrats polimèrics per a la propera generació electrònica plegable i doblegable.
- Un nou enfocament per augmentar de forma natural la conductivitat elèctrica de superfícies transparents basades en el grafè, sense necessitat de posttractament, portes elèctriques o altes temperatures. En particular, el mètode aconsegueix una conductivitat de magnitud comparable o més gran que el que s'informa en estudis anteriors. A més, l'augment de la conductivitat elèctrica es realitza simplement mitjançant l'ús d'un substrat intercanviat d'ions, un substrat

de vidre transparent tecnològicament rellevant que s'utilitza àmpliament en pantalles tàctils (p. ex. telèfons intel·ligents).

- Una tècnica de dewetting de metall de baixa temperatura per obtenir recobriments nanoestructurats antimicrobians transparents en un substrat de vidre de coberta per mòduls de visualització. La durabilitat dels recobriments es va avaluar en condicions dissenyades per simular casos d'ús del món real com ara pantalles tàctils capacitives. Els resultats mostren que els recobriments eren capaços de retenir substancialment les propietats òptiques del substrat subjacent, com ara la boirina, el color neutre i la transmissió de llum visible, així com retenir les propietats antimicrobianes després de contacte repetit amb objectes externs com, per exemple, quan es cableja amb una tovallola o un drap, o tocar amb els dits humans.

Els resultats d'aquesta tesi demostren l'aplicació de materials ultraprims i nanoestructurats, com el grafè i els metalls nanoestructurats en una àmplia gamma de substrats transparents tecnològicament rellevants, per mètodes que són industrialment escalables i compatibles amb el processament de baixes temperatures. Al mateix temps, les superfícies estan dissenyades amb funcionalitats òptiques i biològiques avançades que són rellevants per a aplicacions com elèctrodes transparents i recobriments antimicrobians.

FUNDING

The authors acknowledge financial support from the Spanish Ministry of Economy and Competitiveness through the “Severo Ochoa” Programme for Centres of Excellence in R&D (CEX2019-000910-S) [MCIN/ AEI/10.13039/501100011033] and the project TUNA-SURF (PID2019-106892RB-I00), from Fundació Privada Cellex, Fundació Mir-Puig, and from Generalitat de Catalunya through the CERCA programme, from AGAUR 2021 SGR 01458.

ACKNOWLEDGEMENTS

I would like to express my deepest gratitude to all those without whom this work would not have been be possible.

To my supervisor Valerio Pruneri. I would need to dedicate an entire page in thanks but, as you taught me to keep to the point, I would simply say that you have made my experience as PhD student in your group one I always remember as positive, supportive and motivating.

I would like to thank the thesis committee members F. Pelayo Garcia De Arque, Todd St Clair and Ilaria Mannelli for providing valuable input and improving the thesis.

A special thanks to Corning Incorporated who have been the largest collaborator on the work described in this thesis. In particular to Prantik Mazumder for your help and continued suggestions to improve the quality of my research throughout all of the projects within my PhD.

Wageesha Senaratne and all those in the R&D team at Corning Incorporated who helped consolidate the antimicrobial project. I thoroughly enjoyed this work and I am especially grateful for your support, teaching, and for performing some of the analysis that helped to steer the experiments in a productive direction. Despite being on another continent, it was a great pleasure and easy to work with you.

To the electronic workshop led by José Carlos, and the mechanical workshop led by Xavi Menino.

Miriam Marchena, who was a role model to me during my first years. She helped me to write the first and third papers, and above all was always extremely supportive. I learned a lot from you.

Bruno Paulillo, for teaching me good working practices for nanofabrication. In addition, continued guidance and input in

designing the experiments, interpreting results and planning the course of work. In addition, to reviewing the papers. I learnt a lot!

The Opto group was fantastic, so friendly, welcoming and happy to be around. Despite many people coming and going over the 4 years, the sense of family remained strong. There are some members of the I would like to express special thanks.

To the original office 256 Rinu, Rafa and Miriam. A part from making the office a fun place, I would like to express special thanks to Rinu, for teaching me your expertise on thin films and to Miriam, for teaching me graphene, CVD and MoS_2. To my 2nd office 256, Nacho, Luis and Lorenzo. We were working on different projects but nonetheless, I always appreciated our office talks.

Daniel Martinez, you are the group expert in the electrical characterisation. I am extremely thankful for your unending assistance and tips in performing electrical measurements.

Alessia Mezzadrelli, for being a great team mate on the antimicrobial project. I am really happy that you will continue this work.

Vittoria Finazzi, no amount of acknowledgement would be sufficient. We are more than lucky to have you.

To the nanofabrication lab staff, Javi Perez, Paula Diaz, Luis Enrique, Johan Osmond. I spent probably the largest amount of time in the clean room and it was not uncommon to have problems large and small. I would like to acknowledge the amount of work that goes into making the clean room work 24/7. For continued training on the use of equipment and maintenance of equipment.

The IT department. I spent a good amount of time working from home to write papers and the thesis and many times encountered problems with connecting to my remote workstation.

Thanks to Anne, Ingrid Laia, Mery and Mireia and all those who are in the HR department.

To the front Desk team, especially Raul.

To the purchasing department. Besides from processing all the purchases needed in the lab, I spent a lot of time sending samples to the US. This task was made very easy and enjoyable by Santi and Front desk.

Maintenance team, Carlos Dengra and Núria Segú.

Finally, to my dear friends in Barcelona. I am so happy to have settled here.

LIST OF PEER-REVIEWED PUBLICATIONS

Journal Articles

C. Graham *et al*. (2020) ´´NaCl substrates for high temperature processing and transfer of ultrathin materials´´ Scientific Reports, 10, 7253.

C. Graham et al. (2023) ´´High and stable n-doping of graphene on ion-exchanged glass”, 2D Materials. 10 035037

Journal articles under review

C. Graham *et al*. (2023) ´´Durable, transparent and antimicrobial nanostructured surfaces on glass´´ (Under review)

Patent Applications

C. Graham, V. Pruneri, W. Senaratne, D. Thelen ID33460 ‘’Antimicrobial surface with high transparency and durability using discontinuous metal islands’’

CONTENTS

LIST OF FIGURES

LIST OF TABLES

NOMENCLATURE

µH: Charge carrier mobility
2D: two dimensions
3D: three dimensions
AC: Alternating current
AFM: Atomic Force Microscope
Ag: silver
AgNW: silver nanowire
AR: anti-reflection
Au: gold
B: Magnetic field
C1, C2: Geometrical factor for Rs calculation
CBM: Conduction band maxium
Cu DNPs: Copper dewetted nanoparticles
CNP: Charge neutrality point
CNT: carbon nanotubes
CVD: Chemical Vapor Deposition
DC: Direct Current
DI: deionized
E: Electric field
EPA: Environmental Protection Agency
FET: Field effect transistor
F_L: Lorentz force
FWHM: Full Width at Half Maximum
HOMO: highest occupied molecular orbital
HTA: high temperature annealing
I: Current
I_{12}: Current injected from contact 1 to 2
I_{14}: Current injected from contact 1 to 4
I_{23}: Current injected from contact 2 to 3
I_{2D}: Intensity of the 2D Raman peak
I_{34}: Current injected from contact 3 to 4
I_D: Intensity of the D Raman
I_G: Intensity of the G Raman
IR: infrared
ITO: indium doped tin oxide
LED: Light emitting diodes
LUMO: Lowest unoccupied molecular orbital
NaCl: Sodium Chloride
NA: numerical aperture
NIR: near infrared
NWs: Nanowires
n_S: Charge carrier density

PEDOT: Poly (3, 4-ethylenedioxythiophene)
PAA: Polyamic acid
PDMS: Polydimethylsiloxane
PET: polyethylene terephthalate
PI: Polyimide
PMMA: Poly(methyl methacrylate)
PS: Polystyrene
PSS: poly (styrene sulfonate)
PVD: Physical Vapor Deposition
PVP: poly(vinylpyrrolidone)
q$_e$: Electron charge (1.602·10-19 C) xiv
R: reflection
RMS: Root Mean Square
R$_{12,34}$: Resistance. Voltage measured in contacts 3-4. Current injected from contact 1-2
R$_{14,23}$: Resistance. Voltage measured in contact 2-3. Current injected from contact 1-4
R$_{23,14}$: Resistance. Voltage measured in contact 1-4. Current injected from contact 2-3
R$_{34,12}$: Resistance. Voltage measured in contact 1-2. Current injected from contact 3-4
$\boldsymbol{Rs}$: Sheet resistance
RT: Room temperature
RTA: rapid thermal annealing
SDG: Soda lime glass
SEM: Scanning Electron Microscopy
t: Thickness
T: Transmission
T$_F$: Film transmittance without substrate contribution
T$_g$: Glass transition temperature
TC: Transparent conductor
TE: Transparent electrode
TCO: Transparent Conducting Oxide
TiO$_2$: titanium oxide
$\boldsymbol{TS}$: Substrate transmission
$\boldsymbol{T}\mathbf{TC}$: TC transmission
$\boldsymbol{T}\mathbf{TOT}$: Total transmission
UTMF: ultrathin metal films
UV: Ultraviolet
V: Voltage
V$_{12}$: Voltage, measured in contact 1-2
V$_{14}$: Voltage, measured in contact 1-4
V$_{23}$: Voltage, measured in contact 2-3
V$_{34}$: Voltage measured in contact 3-4
VBM: Valence band minimum
V$_G$: Charge neutrality point
V$_H$: Hall voltage
WCA: Water contact angle

XPS: X-ray photoelectron spectroscopy
ZnO: Zinc Oxide

λ: Wavelength
ρ: Resistivity

CHAPTER 1

1.1 Introduction

The field of ultrathin materials has come a long way since the first exfoliation of graphene, oxides and metals. Thanks to improved growth and processing techniques it is now possible to obtain high quality ultrathin materials, including graphene and nanometer thick metals on a large scale, offering the possibility to create multifunctional transparent surfaces with anti-reflective, electrically conductive, self-cleaning and antimicrobial properties, to name a few. Furthermore, doping and nanostructuring techniques, provide the means to create transparent ultrathin surfaces with advanced functionalities including electrical and electro-optical tunability and tailored light-matter interactions. To this end, ultrathin materials have been used to add functionality to transparent surfaces applied towards products in the display, photovoltaic and coating industries. However, despite their impressive success, the huge potential of ultrathin materials remains to be fully realised.

One of the fundamental challenges is that existing growth and processing techniques often do not facilitate scalability at an industrial level. There is a need to develop mass-scalable methods of surface modification at the nanoscale. A second challenge concerns engineering specific material properties by methods that are reliable, repeatable, economic, stable and outperform existing solutions. For example, high electrical conductivity and optical transparency, are properties required by transparent conductors (TCs). Ultrathin materials such as graphene have been recognized as potential candidates in next generation TCs, though challenges remain in improving conductivity to levels that can compete with the existing state-of-the-art. Finally, the advent of flexible electronics has driven the need to innovate the growth, processing and transfer of ultrathin materials that traditionally require high temperatures or whose properties are not fully compatible with respect to the substrate. This would enable a host of functional surfaces on a wide class of substrates.

In this regard, the main objective of this thesis is to design and develop transparent surfaces with advanced functionalities for optical and biological applications based on ultrathin materials. The functionalities include transparent electrodes and antimicrobial properties. The ultrathin materials include graphene, MoS_2, and nanometer thick metals which can also be nanostructured.

The specific objectives of this thesis are:

(i) Develop scalable techniques to transfer 2D materials, such as graphene and MoS_2 and nanostructured metals onto transparent flexible substrates at low temperatures
(ii) Find the optimum substrate-graphene combination for increasing doping and the electrical conductivity of transparent surfaces.
(iii) Use ultrathin metals and subsequent nanostructuring for increasing the antimicrobial activity of transparent surfaces

1.2 Thesis Outline

The thesis is organised into six chapters:

Chapter 2 provides a brief review of ultrathin materials properties, including graphene, 2D transition-metal dichalcogenides, and nm scale metallic nanostructures, together with some theoretical background on the growth mechanism of 2D materials, and their electrical and optical properties. The characterization methods used to analyse and optimize the modified transparent surfaces are also included. Finally, the electrical and biological applications of 2D materials are summarised with a focus on transparent electrodes and transparent antimicrobial surfaces.

Chapter 3 is dedicated to the optimisation of low temperature fabrication and processing techniques for 2D materials and nanostructured metals. The first section describes the deposition, growth and nanostructuring techniques utilised in this work. The second section includes a study of a system of Copper dewetted nanoparticles (Cu DNPs) fabricated on low strain point transparent glass substrates. The dewetting conditions and UTMF precursor thickness were optimised for obtaining maximum transparency in the visible region. A complete theoretical and experimental analysis of the morphological and optical properties of the samples as a function of dewetting temperature is also presented. The third section describes a novel growth and processing technique which enables high thermal processing materials e.g. MoS_2 and metallic nanostructures to be obtained on low strain point substrates such as polyethylene terephthalate (PET). A full optical and morphological characterisation of the as grown and transferred materials is provided. The techniques presented in this chapter represent important innovations as they are universal and not limited by the underlying substrate. In such a way this work opens up the possibility to obtain a host of functional electrooptical and biological surfaces on flexible substrates.

Chapter 4 focuses on tuning the electrical functionality of a transparent surface made of graphene. The first section includes a review of the state-of-the-art doping techniques and the challenges regarding the implementation of doped graphene into real-world devices. The second section investigates a novel and scalable method of inducing ultrahigh n-doping of graphene by utilising a transparent ion-exchanged glass substrate. The fabrication and electrical characterisation of graphene devices is described and a doping mechanism is proposed. The innovations described in Chapter 4 and, specifically the ability to achieve high, relatively stable, and tunable graphene doping on low-cost, industry-standard materials, pave the way for the practical realization of many envisioned applications of graphene such as transparent electrodes for touch screens and organic light-emitting diodes, where the reduction of sheet resistance is crucial. The results of this work are also important for applications requiring strong and tunable n-doping, such as microelectronics, photodetectors, photovoltaics, low work function tunable electrodes and sensors.

Chapter 5 is dedicated to the development of transparent antimicrobial (AM) surfaces on cover glass substrates for display and touchscreen applications. The first section reviews the state-of-the-art techniques to impart AM functionality into transparent substrates. This also includes an overview of the existing commercially available solutions. The second section describes the optimisation of the metallic nanostructures developed in Chapter 3 to realise transparent coatings with AM functionality that are also durable and long lasting. The coatings are easy to clean, maintain their AM functionality, optical and wetting properties over a long period of time, whilst also being fabricated in a way that is industrially scalable. A full characterisation of the samples is provided. It is anticipated that the results of this work will be useful in many applications of technological interest such as touch-enabled public displays.

Chapter 6 summarizes the main results of this thesis, and gives a brief outlook on potential future developments.

CHAPTER 2

Ultrathin materials overview

Ultrathin materials are defined as materials which have a large lateral size (up to a few micrometres and larger), but whose thickness is only single- or a few-atoms thick (typically less than 10 nm). This dimensionality confers a range of intrinsic extraordinary physical, electronic and optical properties as electrons are confined to two dimensions. Furthermore, being atomically thick, these materials have unmatched mechanical flexibility and optical transparency and large specific surface areas making them compelling for the fabrication of highly flexible and transparent electronic/optoelectronic devices. In addition to their remarkable intrinsic properties, 2D materials are also highly tunable by the application of a gate voltage, strain and external electric field. This enables material properties to be dynamically tuned to suit the application or environment. The following sections provide an overview of the fundamental properties, characterisation techniques and applications of ultrathin materials, focussing mainly on graphene, MoS_2 and nanostructured metals, their characterisation and implementation and transparent optical and biological applications.

2.1 Graphene and 2D materials

Arguably the most famous of the 2D materials is graphene, a single layer of carbon atoms arranged in a honeycomb lattice structure, as shown in Figure 1a. From an optoelectronics standpoint, it is both electrically conductive and optically transparent, two properties rarely found together, making it a natural candidate for next-generation transparent conductors (TCs). Graphene first attracted significant attention after 2004, when Novoselov and Geim isolated it in monolayer form, using a scotch tape exfoliation method. They also demonstrated its electrical field effect transistor behaviour [1]. Graphene's outstanding properties were further outlined in later studies [2–4], including the demonstration of the room temperature quantum Hall effect [5] and high room temperature carrier mobility [6] which eventually led to Novoselov and Geim being awarded the Nobel Prize in Physics in 2010 [7,8].

These remarkable phenomena arise due the unique bonding structure of graphene. The sp^2 hybridised orbitals of the carbon atoms support sigma (σ) and pi (π) bonding components as shown in Figure 1b. The σ bond is formed in the x-y plane when two sp^2 hybridised orbitals of adjacent carbon atoms overlap. The π bond is formed in the z plane where two p_z orbitals of two adjacent carbon atoms overlap. The electrons in the σ bonds are held strongly and give graphene its mechanical strength, whilst electrons in π bonds are held weakly, and delocalise above and below the plane of bonded carbon atoms and are responsible for its excellent thermal and electrical conductivities.

The hexagonal arrangement of carbon atoms gives rise to a unique band structure where the valence and conduction bands touch each other at the so-called Dirac point or charge neutrality point (CNP) [9], Figure 1c. At the Dirac point the density of states (DOS) is zero and by this definition, graphene is referred to as a zero-band gap semiconductor or a zero-overlap semimetal. Under neutral conditions, when graphene is undoped the Fermi level (E_F) lies at the meeting point of the bands and the intrinsic charge carrier concentration (n_S) is, in principle, zero. Close to the Dirac point, the charge carriers have a linear relationship between energy and momentum. This linearity considers the charge carriers as massless Dirac fermions [2,10], which are described by the relativistic Dirac equation rather than the non-relativistic Schrodinger equation. The carriers travel at a relativistic Fermi velocity, v_F = $c/300$, where c is the speed of light in vacuum. The injection of charge carriers, denoted n_s (electrons or holes), through, for example electrical gating or chemical doping, results in a square-root shift in the Fermi energy with respect to the value at the Dirac point according to Eq. 2.1

$$E_F = \hbar v_F k_F = \hbar v_F \sqrt{\pi n_S} \tag{2.1}$$

where $\hbar$ is the reduced Planck constant and $k_F = \sqrt{\pi n_s}$ is the Fermi wave vector. Moreover, given the linear dispersion and vanishing density of states at the Dirac point, only a moderate increase in n_s is required to induce substantial changes in E_F. This is in contrast to other semiconductor materials whose band structure can be considered parabolic for very low energies and $E_F \propto n_s$.

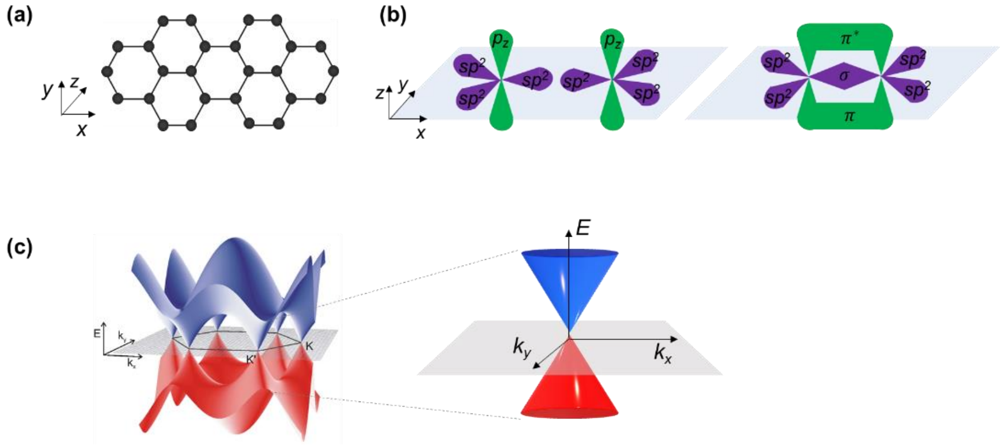

Figure 1 (a) Graphene structure showing planar hexagonal arrangement of carbon atoms. (b) Bonding scheme of graphene in which two carbon atoms contribute one electron each from each sp_2 orbital to form a σ bond. The remaining single electrons in the p_z orbitals of the two carbon atoms combine to form a π-bond. (c) 3D-graphic of graphene band structure with K and K’ Dirac points. Zoom area shows the zero-bandgap of graphene where valence band (bottom) and conduction band (top) meet. The graphic has been adapted from reference [6].

Tunable electronic properties of graphene

Charge carriers can be induced into graphene by the electrostatic field effect or by chemical means. For electrostatic doping, an electrical bias is applied to the graphene. The typical device structure for achieving the field effect is the field effect transistor (FET). Recently, transparent Graphene FET devices have been demonstrated in which the graphene channel is patterned on a transparent substrate, such as quartz or borosilicate, and is surrounded by the source and drain electrodes, made of another transparent conducting material or graphene [11]. The gate electrode is separated from the graphene channel by a thin insulating layer, typically made of silicon dioxide (SiO_2), aluminium oxide (Al_2O_3), hafnium dioxide (HfO_2), silicon nitride (Si_3N_4) or hexagonal boron nitride (hBN). This configuration resembles a capacitor with the gate electrode and the graphene acting as the two plates of the capacitor. The application of voltage to the gate electrode induces an electric field in the insulating layer that causes charges to accumulate on the graphene as a function of the applied gate voltage (V_G). The carrier density, n_s, is tuned electrostatically with the application of a gate voltage. The change in n_s as a function of V_G translates to a change in the resistance of the graphene device (as shown in Figure 2) and can be measured across the source and drain contacts. With the applied gate voltage (V_G), the resistance of the graphene changes as the number and type of charge carriers change from p-type at negative voltages to n-type at positive voltages. When n_s approaches zero, graphene shows a finite maximum resistance at the charge neutrality point (CNP), due to the absence of a band gap. At the Dirac Point, graphene exhibits a minimum conductivity, which is approximately on the order of magnitude $4e^2/\hbar$. The charge carrier density is related to the electrical conductivity (σ) by the Eq. 2.2:

$$\sigma \approx \mu e n_s \tag{2.2}$$

where μ is the carrier mobility and e is the elementary charge. n_s is determined by the doping level. The carrier mobility is affected by the electron scattering by lattice vibrations, lattice defects for example holes, impurities, wrinkles and grain boundaries. Whilst suspended graphene has a mobility in the order of ~10^6 $cm^2/V\cdot s$ [4,12], the mobility of supported graphene is limited by several factors including its interaction with substrate phonons, charged impurities and lattice defects. Nonetheless, graphene still exhibits a room temperature mobility that far surpasses most conventional semiconductors, recently reaching values up to 350,000 $cm^2/V\cdot s$ [13] for a hexagonal boron nitride (hBN) encapsulated device.

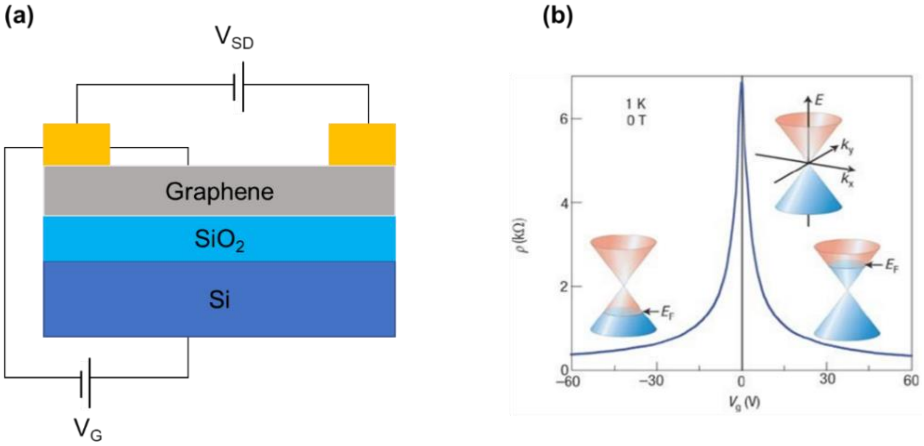

Figure 2 A typical two-probe graphene device (Graphene FET) that can be electrostatically tuned. b) Ambipolar field effect in graphene, taken from Ref[6]. The plot is resistivity as a function of gate voltage (V_G). The insets show its conical low-energy spectrum E(k), indicating changes in the position of the Fermi energy EF with changing gate voltage V_G. Positive (negative) V_G induces electrons (holes), respectively.

Optical properties of graphene

The zero-band gap nature of graphene gives it exceptional optical properties [14–16]. In the undoped state, graphene is characterized by its universal optical conductivity, $\sigma_{uni} = \pi e^2/2h$, where e is the electronic charge and h is Planck´s constant. This gives rise to the well-known universal absorption of 2.3 % in the region from visible to near-IR frequencies. When electrically doped, an optical gap opens up which is proportional to the applied bias voltage [17–19].

2.1.1 Transition metal dichalcogenides: MoS_2

Beyond graphene, one group of 2D materials that has amassed great attention is transition metal dichalcogenides (TMDs). These materials combine the ultrathin nature of graphene with exceptional semiconductor properties. In Chapter 3 of this thesis, MoS_2 was chosen as a prototypical 2D material for the development of a novel transfer process that enables high thermal processing materials to be obtained on low strain point flexible substrates. The following section describes the structural, electrical and optical properties of MoS_2 and its applications.

Structure

Bulk TMDs, with the general formula MX_2, consist of vertically stacked sheets where each 3-atom thick sheet consists of a layer of transition metal atoms, M, such as molybdenum (Mo) or tungsten (W), between two planes of chalcogen atoms, X, such as sulphur (S) or selenium (Se), as shown in Figure 3a. The atoms within each layer of TMDs are held together by covalent bonds, while vertical layers are held together by weaker van der Waals interactions. The layers can be arranged in a variety of polytypes, which vary in stacking orders and metal atom coordination, the most energetically favourable being the 2H phase.

Optical and vibrational properties

In the 2H-polytype, both bulk and few layer MoS_2 exhibit semiconducting behaviour, with an indirect band gap transition in which the valence band maximum (VBM) and conduction band minimum (CBM) are located at the Γ point and Λ points of the of the Brillouin zone, respectively. With decreasing layer number, both the CBM and VBM shift toward the K point, resulting in a direct band gap of 1.9 eV for monolayer MoS_2 [20] as shown in Figure 3b. The change in the band structure with layer number is due to quantum confinement and the resulting change in hybridization between p_z orbitals on S atoms and d orbitals on Mo atoms [21].

This transition to a direct band gap is significant as photons with an energy higher than the bandgap can be efficiently absorbed and emitted, and is therefore able to reach significantly higher quantum yields than bilayer and bulk devices [20]. TMD monolayers are also extraordinary light absorbers. MoS_2 can absorb up to 5–10% incident light at visible frequencies in a thickness of less than 1 nm, thus achieving one order of magnitude higher visible light absorption than GaAs.

Moreover, compared with classical direct-bandgap semiconductors, MoS_2 can offer additional advantages in the context of optoelectronics because of its optical transparency (~ 91% for monolayer in the visible range) and mechanical flexibility [22–24].

Together these outstanding properties make MoS_2 an ideal candidate for optoelectronic applications with primary progress demonstrated in field-effect transistors [25,26], light-emitting diodes [27], sensing [28], atomically thin photodetection platforms [29,30] and flexible electronics [31,32]. Most notable examples have included the demonstration of up to a 10% absorption of sunlight for monolayer MoS_2 [33]. Chapter 3 of this thesis demonstrates the growth of MoS_2 on a novel substrate that enables its subsequent transfer to flexible substrates.

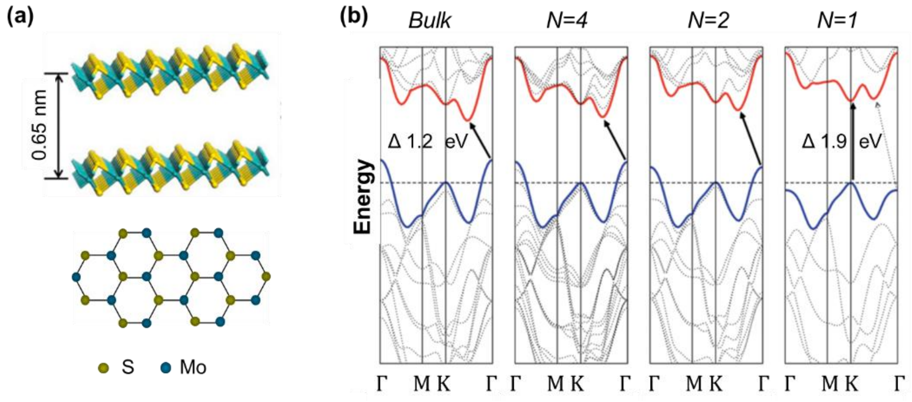

Figure 3 (a) Chemical structure of two layers of MoS_2 (b) Energy dispersion (energy versus wavevector k) in bulk, quadrilayer (4L), bilayer (2L) and monolayer (1L) MoS_2 from left to right, where *N* indicates the number of layers. The horizontal dashed line represents the energy of a band maximum at the K point. The red and blue lines represent the conduction and valence band edges, respectively. The solid arrows indicate the smallest energy transitions. There is an indirect transition for bulk and few-layer crystals that becomes a direct transition for a monolayer MoS_2. Adapted from Reference [34]

2.1.2 hBN and layered 2D materials

Among other 2D materials, hexagonal boron nitride (hBN) is notable. It shares the same honeycomb structure as graphene, but with a distinction where the sublattice symmetry is disrupted by the substitution of boron and nitrogen atoms at the A and B sublattice positions, respectively. It has a wide band gap (5−6 eV) making it an insulator [35]. It has good thermal conductivity (751 /m·K) and is regarded as a good candidate for dielectric layer in conjunction with Si/SiO_2 substrate or direct growth substrate because of its atomically flat surface and the lack of dangling bonds and charge impurities at the surface [36–39]. hBN is also used as an encapsulation layer for other 2D materials due to its impermeability, chemical inertness, and thermal stability [40–42]. In addition to the extraordinary fundamental properties that arise at low dimensions, the ability to combine or stack isolated 2D materials into multilayer heterostructures gives rise to artificial materials which often reveal unusual properties and new physical phenomena [43,44].

2.2 Ultrathin metal films and nanostructures

Similarly, ultrathin metal films (UTMFs), with thicknesses below 10 nm, are another class of materials which produce interesting electrical and optical properties (e.g. high optical transmittance, high conductivity and low sheet resistance and strong plasmons [45]) at low thickness. Moreover, their deposition on a wide variety of substrates (e.g. rigid and flexible) [46,47] makes them attractive in a number of optoelectronics applications including transparent conductors [48,49], photovoltaics [50], low emissivity windows [51], infrared absorbers [52], plasmonic meta-surfaces [53], and point-of-care biosensors [54] to name a few. This thesis is concerned with nanostructured UTMFs, which are obtained after thermal annealing treatments of UTMFs < 5 nm thickness. The following sections describe the processes of UTMF growth, their subsequent nanostructuring and applications.

2.2.1 Ultrathin Metal Film (UTMF) growth

The ultrathin films (UTMFs) in this thesis were grown by sputtering, a technique which will be described in Section 3.2.2. The growth of ultrathin films follows three stages (1) nucleation, (2) coalescence (3) thickness accumulation. During nucleation, incoming particles interact and adhere to the substrate forming nucleation sites. During coalescence, the nucleation sites grow to form interconnected islands. At this stage the film shows a high roughness and inhomogeneity. Further deposition increases the thickness of the material until a uniform film is obtained. The interaction energy between the incoming particles and the uncovered substrate surface and existing particles determines the growth mechanism, which determines the final properties of the film such as surface roughness and electrical conductivity.

According to the criteria developed by Bauer [55], there are three different growth modes that can be observed in the nucleation stage. The modes, presented in Figure 4, depend on the surface free energy of the substrate ($\gamma_{\text{substrate}}$), the free energy of the interface ($\gamma_{\text{interface}}$), and the free energy of the film (γ_{film}). Under equilibrium conditions, the growth mode is determined by the so-called wetting factor, ϕ, which is influenced by the competition between the surface and interface energies:

$$\Phi = \gamma_{\text{film}} + \gamma_{\text{interface}} - \gamma_{\text{substrate}} \tag{2.3}$$

If the interaction between the deposited atoms and the substrate is stronger than the interaction between the adjacent deposited atoms ($\Phi < 0$), a complete wetting of the substrate is observed leading to the formation of a uniform, layer-by-layer (or Frank-Van der Merwe) growth (Figure 4c). In most cases, the free energy of the interface is larger than the substrate free energy ($\Phi > 0$). Under these conditions, the adjacent incoming particles interact more strongly with each other than with the substrate leading to a 3D island like (or Volmer-Weber) growth (Figure 4a). A third hybrid growth mode, known as the Stanski-Krastanov mode, arises during the crossover from 2D to 3D growth, which occurs above a critical thickness when the free energy relation switches from: $\gamma_{film} + \gamma_{interface} \leq \gamma_{substrate}$ to $\gamma_{film} + \gamma_{interface} > \gamma_{substrate}$. This is shown in Figure 4b.

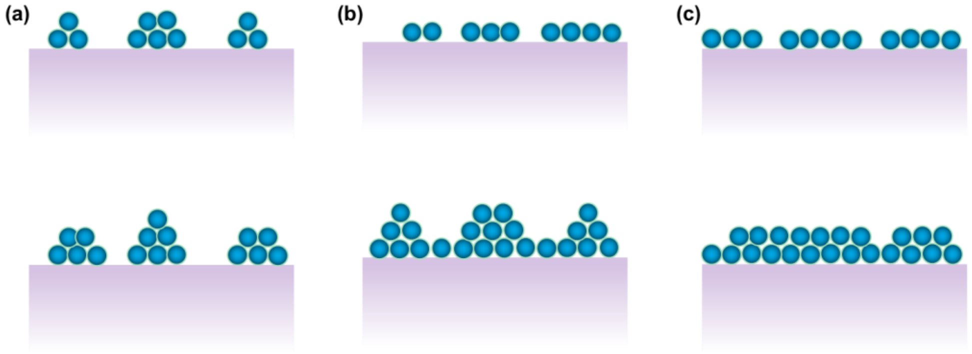

Figure 4 Schematics of three kinds of thin-film growth modes. a) Volmer-Weber mode (3D island growth). b) Stranski-Krastanov mode (layer plus island growth). c) Frank-van der Merve mode (layer-by-layer growth).

The efficient adhesion of the UTMF on dielectric or semiconductor substrates is essential in applications and research within plasmonics, metamaterials, 2D materials and nano-electronics. Noble metals such as gold, silver and copper are often used for these applications, however they adhere poorly to the substrate, leading to phenomena like island-formation, delamination, peeling, and time-dependent device performance deterioration.

A technique widely employed to improve adhesion and suppress the 3D growth modes of UTMFs is seeded growth. This relies on the deposition of an ultrathin seed layer onto the growth substrate that dramatically changes the wetting factor (Φ) and subsequent growth of UTMFs thereby reducing their percolation thickness, that is the thickness at which the UTMF becomes physically connected and electrically conductive [56–59]. Seeded growth is particularly useful for improving the adhesion between metals and oxide substrates such as glass. In this thesis, titanium (Ti) is used for the seed layer for the deposition of gold contacts and Cu UTMFs in Chapter 4 and Chapter 5, respectively.

From a thermodynamics point of view a criterion for good adhesion between a metal film and an oxide substrate is that the metal must be oxygen negative to react chemically with the oxide surface, to form a strong covalent oxide bond. In other words, when the enthalpy of formation (ΔH_f^{Θ}) for the metal oxide is less than that of SiO_2, it indicates a favorable condition for the formation of a covalent oxide bond between the metal and the oxygen atoms in the glass. In this context, enthalpy of formation (ΔH_f^{Θ}) for titanium oxide (TiO) < ΔH_f^{Θ} silicon dioxide (SiO_2) < ΔH_f^{Θ} copper oxide (CuO) and therefore, Ti would favorably form an oxide layer with the glass while Cu would not due to the improved oxide forming ability of the Ti seed layer with the glass [60]. In this thesis, 1-3 nm of Ti is deposited as a seed in order to achieve the optimum gradation from TiOx at the glass interface to fully metallic at the Ti/Cu or Ti/Au interface such that a good adhesion between Ti and metal is obtained.

2.2.2 Nanostructured UTMFS

UTMFs deposited through physical vapour deposition are generally unstable or metastable in the as-deposited state. When provided with sufficient thermal energy, the activation barrier for atomic diffusion is overcome and mass transport and capillary forces drive the film to agglomerate (dewet) into nanoparticles, Figure 5 [61]. This process can occur well below the metal’s melting temperature, which maintains the dewetted material in the solid-state and permits the use of various materials as a substrate. Dewetting typically starts on defects, holes, contamination sites or directly from the edges of the substrate. From there, it expands over the hole formation until it breaks up into nanoparticles. By changing the dewetting process parameters including for example, time and temperature, initial UTMF thickness or chamber atmosphere, it is possible to tailor the resulting dewetted nanoparticles’ shape, size and coverage of the underlying substrate. The kinetics and thermodynamics of the metal dewetting process is described in detail in reference [62]. The tunable properties of dewetted UTMFs are demonstrated in Chapter 3 for a transparent surface.

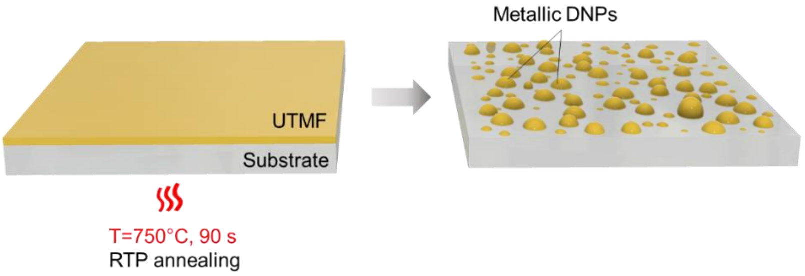

Figure 5 Representation of the solid-state dewetting process. A uniform thin film self-assembles into isolated islands when rapidly heated. The initial UTMF thickness, annealing temperature and the duration of thermal treatment, together with the material composition of the film, will affect the distribution and size of the nanoparticles.

Optical properties of nanostructured metals

For noble metals, such as Au and Cu, the Drude model [63,64] gives a good description of the dielectric constant in the near-IR region, but it breaks down in the visible to near-UV due to the onset of interband transitions from lower-lying d-bands to the sp-hybridized conduction bands. The onset of the interband transitions is at ~2.1 eV for Cu [65]. The interband transitions give a frequency dependent damping, and can be included in the dielectric function by adding additional Lorentzian terms. The Lorentz–Drude dielectric model is then given by the combination of the Drude component and Lorenzian contribution. Sub-wavelength sized NPs also have additional damping effects that arise from scattering of electrons with the surface of the NP.

Localised surface plasmon resonance

Localised surface plasmon resonance (LSPR) is an outstanding optical property of metallic nanoparticles. When light is incident on a metal nanoparticle that has a size smaller or comparable to the incident light wavelength, it exerts a force on the conduction electrons. This causes them to move towards the NP surface. This movement of negative charge induces an electric dipole and creates an electric field inside the NP (also known as the restoring field) [68]. LSPR is the resonant collective oscillation of conduction electrons with respect to immobilized positive ion cores, as depicted in Figure 6a. The resonance frequency of metallic NPs corresponds typically to UV–Vis light and consequently, the LSPRs lead to absorption bands in this region of the spectrum. At the LSPR wavelength, due to the charge separation at the surface of the nanoparticle a strongly enhanced electric field is generated locally around the nanoparticle (Figure 6b). There are large regions where the electric field generated by the NP is opposite to that of the light, leading to destructive interference and light extinction beyond the NP volume.

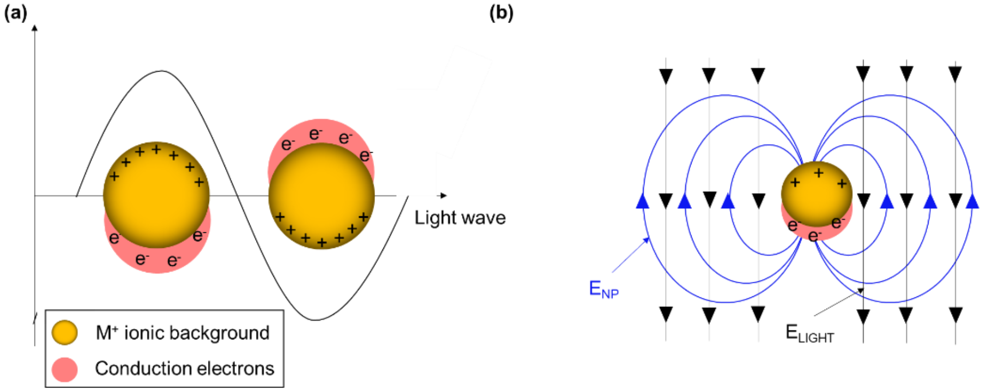

Figure 6 (a) Illustration of electric fields of incident light and those generated by the electron oscillations near the NP. Yellow shaded region indicated M^+ ionic background. (b) Schematic drawing of the interaction of an electromagnetic radiation with a nanoparticle. It generates a dipole that oscillates in resonance with the electric field of the incident light as well as a strong confined electric field at the nanoparticle surface.

The efficiency with which NPs extinguish light is given by the extinction cross section, σ_{ext}, which is the sum of the absorption and scattering cross sections. Light absorption has an exponential dependence with σ meaning that a small increase in σ leads to a huge light extinction. A light beam propagating though a medium containing NPs decays in intensity according to Eq. 2.4:

$$I(x) = I_0 \cdot \exp(-C \cdot \sigma_{ext} \cdot x) \tag{2.4}$$

where *C* is the number of NPs per unit volume, σ_{ext} is the extinction cross section and *x* is the distance travelled. This underpins the advantage of LSPR since the cross sections are much larger (up to 10 times their diameter of the NP) than compared with other optical transitions, for example interband transitions.

Effects of NP size, shape, dispersion and surrounding medium on the LSPR

The number, position, shape and intensity of LSPR of metallic nanoparticles can be tuned over wide spectral range by varying the size, shape, dispersion and surrounding medium of the nanoparticles.

Increasing the NP size induces a broadening and red-shift of the LSPR peak. This effect is attributed to a weakening of the restoring force because as the distance between charges on opposite sides of the particle increases, their interaction decreases.

The intensity of the LSPR is reduced by damping interactions induced by scattering mechanisms. Electron oscillations are damped by scattering off the ionic cores and with the NP surface. Whilst scattering with the ionic cores is a constant and independent of NP size, the scattering with the NP surface is highly size dependent.

The geometry of the metallic nanoparticles is also important in shaping the LSPR. The system studied in this thesis take a nanocap shape, having a flat base and rounded hemispherical cap. The asymmetry induces multiple polarisation axes, giving rise to transverse and longitudinal plasmons. As the restoring force is proportional to the charge accumulation at the NP surface, the LSPR of nanocaps is tunable by the aspect ratio (height to diameter) of the nanocaps.

Finally, the dielectric constant of the surrounding medium, ε_{medium}, affects the LSPR. The electric field that is induced in the region of the NP during the SP excitation, also induces a polarization of the surrounding media, that scales with ε_{medium}. This results in charge accumulation at the interface between the metallic NP and the dielectric media. This charge partially screens the charge accumulation due to the movement of conduction electrons in the NP, resulting in a net reduction in charge at the NP surface, and thereby a reduction in the restoring force. Reduced restoring force implies a reduced resonance frequency, therefore leading to a red shift with increasing ε_{medium}. In Chapter 3, this effect is demonstrated for Cu dewetted systems, in which a reduction in charge at the NP surface due to the interaction with the dielectric media (SiO_2) leads to a decreased restoring force and, consequently, a red shift in resonance frequency as ε_{medium} increases.

2.3 Characterisation techniques

The optical, electrical and morphological properties of the ultrathin materials and nanostructured surfaces fabricated in this thesis were evaluated with a number of techniques. In this section, the methods and equipment used are described and divided into four different categories: optical, morphological, wetting and mechanical. The techniques are discussed by chapter.

2.3.1 Optical

When light is incident on a material, the fraction that is transmitted (T), reflected (R), absorbed (A) or scattered (S) depends on the materials' properties (dielectric constant and refractive index) and surface structure. The total contributions of T, R, A and S sum to 1. The optical properties are determined with several techniques explained briefly in the following sections.

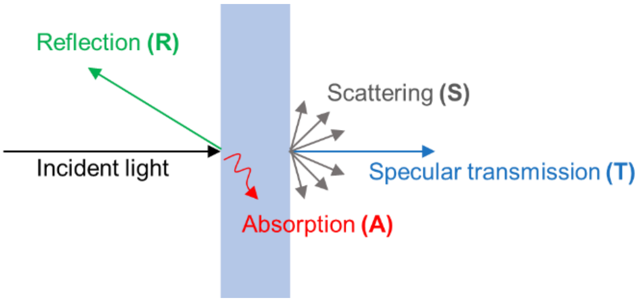

Figure 7 Optical processes occurring when light interacts with a semi-transparent surface

Transmission, reflection and absorption

A PerkinElmer Lambda 950 spectrometer in the UV–Visible region was used to measure the transmission and reflection of samples. The total transmission (%) = $(I/I_o)*100$, in which I is transmitted light intensity at a given wavelength or wavelength range, and I_o is incident light intensity at a given wavelength or wavelength range. In some aspects, the transmission is averaged over the wavelength range of 380-750 nm. The absorption (A) was calculated according to A=100 - T – R (in the case of negligible scattering). Note that the substrate’s contribution is always considered in optical transmittance measurements.

Haze

As used herein, the term “haze” refers to the percentage of transmitted light that is scattered so that its direction deviates more than 2.5 degrees from the direction of the incident beam. The haze should be kept as low as possible for applications requiring high transparency, for example touch display screens such as those proposed in Chapter 5. In this thesis, a Haze-Guard iPro system from BYK instruments was used to measure the haze. The sample is illuminated and all the transmitted light is measured by an integrating sphere. Only light scattered or dispersed at an angle greater than 2.5° is detected, as all forward directed light is excluded by a light trap.

Raman spectroscopy

Raman spectroscopy is a non-destructive optical measurement technique that enables chemical and structural characterisation of a sample. The underlying principle of Raman spectroscopy lies in the coupling of incident photons with the phonon modes of bonds within a material. Incident light can be scattered elastically (Rayleigh scattering) or inelastically (Raman scattering). Elastic scattering implies that the frequency of the emitted photon is the same as the frequency of the incident light. For inelastic scattering, the frequency of the scattered light is larger (anti-Stokes scattering) or smaller (Stokes scattering) than that of the incident light, which is called Raman scattering phenomenon. The majority of phonons within materials experience elastic scattering (around 10^{-3} times the intensity of the incident light) whilst only a fraction undergoes Raman scattering (around 10^{-6} times the intensity of the incident light). Light scattered from the material is passed through a filter which allows only the Raman scattered light to reach the detector. A spectrograph is placed in-between the filter and the detector in order to separate the Raman scattered light by frequency and thus acquire a fingerprint of the vibrational modes within a material.

In this thesis a, Renishaw InVia instrument was used with 532 nm laser. A reduction in the power radiation was selected in order to avoid heat damage on the samples. 50X lenses (with a numerical aperture of 0.75) were used throughout. In addition to single-point spectra, Raman maps of up to 1 μm^2, were also acquired to enable a statistical analysis of larger samples areas. All Raman single-point spectra and maps presented in this thesis were treated by a custom MATLAB® code that combines ten or more spectra obtained from different areas of the sample and fits a single average Lorentzian peak to the relevant peaks, after a linear background subtraction.

Raman spectroscopy of MoS_2

In Chapter 3, Raman spectroscopy measurements are performed to determine the number of layers and quality of as-grown MoS_2, before and after performing the transfer from the growth substrate (NaCl) to the target substrate (PET). MoS_2 has two Raman active phonon modes, depicted in Figure 8. The in-plane vibration (E^1_{2g}) provides information on the in-plane strain, while the out-of-plane mode (A_{1g}) depends on the interaction with its neighbouring material. The frequencies, peak widths and intensities of both Raman modes depend highly on the number of layers of MoS_2 [66]. As the number of layer increases, the E_{2g} vibration observed at ~383 cm^{-1} shows a red-shift (shifts to lower frequency) whereas A_{1g} vibration observed at ~408 cm^{-1} shows a blue-shift (shifts to higher frequencies) [67].

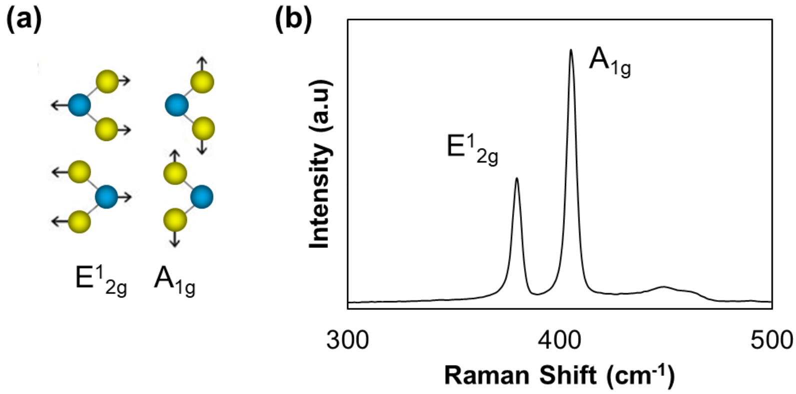

Figure 8 Raman vibrational modes E^1_{2g} and A_{1g} and representative Raman spectra of bulk MoS_2 with E^1_{2g} and A_{1g} peaks at 383 and 408 cm^{-1}. Spectra compares bulk and MoS_2, *(experimentally obtained).

Photoluminescence spectroscopy

Photoluminescence (PL) spectroscopy, similar to Raman spectroscopy, is a contactless fast and non-destructive optical technique to probe the electronic energy structure of materials. When the sample is excited, electron-hole pairs are produced. The electron is excited from the valence band to the conduction band and then relaxes to the band edge before recombining with the hole in a radiative emission process. As photons of particular energy are absorbed by the sample, the energy of the photons emitted can provide evidence of the electronic structure. In the case of MoS_2, where the band structure is layer dependent, PL can be used to determine thickness. Secondly PL spectra can also indicate material quality. If impurities are present in semiconductor materials, the defect energy levels would form near the conduction band or valence band. Depending on the type of impurities introduced, they could act as donor or accepter of electrons in crystals and thus change the energy of the emitted photons.

In Chapter 3, single-point photoluminescence spectroscopy was performed using the Renishaw InVia instrument in order to obtain information regarding the quality of the MoS_2. The photoluminescence spectrum for monolayer MoS_2, (see Figure 9), shows two direct excitonic transitions, the so-called A1 and B1 excitons which appear at 1.85 eV (670 nm) and 1.98 eV (627 nm) and correspond to direct-gap transitions at the K-point of the Brillouin zone between the maxima of split valence bands and the minimum of the conduction band [34]. The ratio of intensities of the peaks is a quality indicator where a low B/A ratio indicates low defect density and high-quality growth and a large B/A ratio signals a high defect density and poor-quality growth [68].

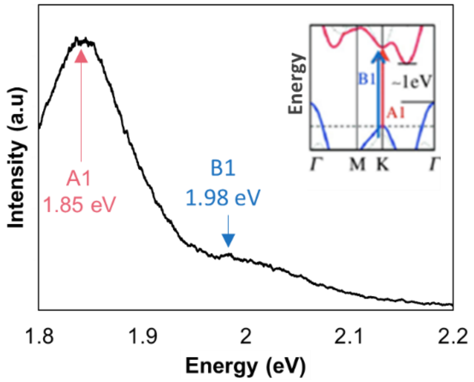

Figure 9 PL spectra of ultrathin MoS_2 (experimental data). The observed absorption peaks at 1.85 eV (670 nm) and 1.98 eV (627 nm) correspond to the A1 and B1 direct excitonic transitions. Inset adapted from reference [34]

2.3.2 Electrical

The following section provides the methodology used for the electrical characterisation of graphene samples and devices fabricated in Chapter 4.

Measurement of sheet resistance

The electrical properties of graphene films are typically described in terms of their sheet resistance, R_s, which for a film with resistivity, ρ, and thickness, t, is defined as,

$$R_s = \frac{\rho}{t} \tag{2.5}$$

As ρ is a measure of the resistance per unit volume of the bulk material, R_S is a scaling independent unit, meaning that it does not depend on the film´s lateral dimensions (only on its thickness), and is typically denoted in units of Ohms per square (Ω/sq.). Rs can be directly measured using a four-point probe set-up. This technique is the most common approach for determining the DC electrical properties of films since it is not affected by parasitic resistances, such as contact resistance, probe resistance or resistances under the probes [69]. There are several configurations in which the measurement can be performed.

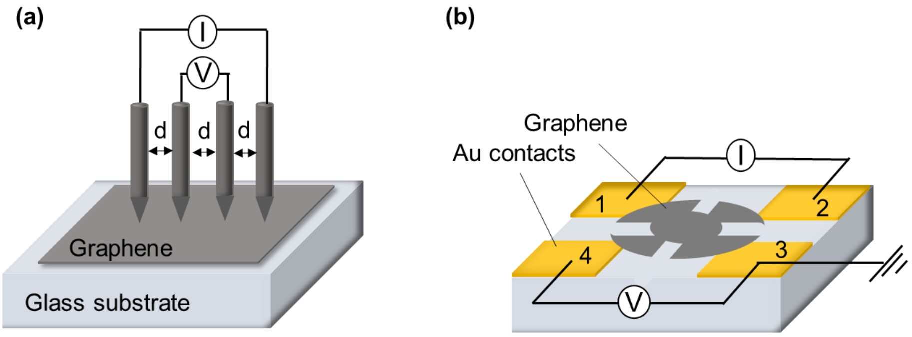

Figure 10 Schematic of the Four Point probe set-up used for the R_S measurement in (a) colinear configuration and (b) Van-der-Pauw configuration with cloverleaf shaped graphene.

For large area graphene samples, in the order of $1 cm^2$, a fixed Cascade Microtech 44/7S 2791 linear four-point probe set-up connected to a Keithley 2001 was used, as shown in Figure 10a. The tips are brought into contact with the graphene surface, a test current (I) is injected through the outer tips while the inner tips measure the voltage drop (V), as shown in Figure 10a. In this case, R_S is calculated as,

$$R_s = C_1 * C_2 * R_m \tag{2.6}$$

where R_m is the measured resistance value, and C_1 and C_2 are corrective coefficients which are related to the ratio between the distance between tips (d) and the graphene thickness (t), and the ratio between 'd' and the sample lateral sizes, respectively (for more details see Ref.[69]). In our case C_1 is approximated to be 1 as the thickness of the graphene is (0.345 nm) is much smaller than the tip separation, d = 1mm, and the area of the graphene (typically $1 cm^2$) is much larger than the tip separation. $C_2 = \pi/\ln(2) = 4.4364$.

For precise measurements of the sheet resistance, a Van der Pauw configuration was used, which allows the electrical conductivity of thin samples with arbitrary shapes to be determined. In this configuration, samples were prepared with 50 nm thick Au rounded contacts 1-4, as shown in Figure 10b. A voltage is applied between two parallel contacts and the current is measured between the remaining two. The area of contact between the metallic pads and the graphene must be infinitesimally small in order to avoid measurement errors [70]. A cloverleaf structure with rounded corners was chosen as it has been shown to be more robust against possible sample defects. In this case, the R_S values are

$$R_S = \frac{\pi}{\ln(2)} * R_m \qquad (2.7)$$

where R_m is the measured resistance value.

Measurement of the carrier density

The quantum Hall effect in graphene allows for a direct measurement of the graphene carrier density, when it is exposed to a perpendicular external magnetic field, B. The underlying principle of the Hall effect arises from the Lorenz force (F_L), which describes the force exerted on a charged particle, such as an electron, when moving through a magnetic field (B).

$$\overrightarrow{F_L} = q_e\left(\vec{E} + \vec{v}x\vec{B}\right) \qquad (2.8)$$

Where q_e is the elementary charge (1.602E^{-19} C), v is the particle velocity and E is the electric field. When B is oriented perpendicular to the direction of the applied electric field, the electron experiences a force that is perpendicular to both the direction of motion and the orientation of the B. The result is that a certain number of charge carriers (n_s) will accumulate at the edge of the device and a transversal Hall voltage (V_H) will appear (Eq. 2.9), where I is the current injected.

In this work R_s, n_s and µ of the Hall bar devices shown in design B of Figure 11 was carried out at 300 K in a Physical Property Measurement System by Quantum Design as follows. A constant DC current of 1 µA was injected into the sample via probes 1-2 whilst probes 3-4 and 3-5 measured the longitudinal (V_{34}) and transverse ($V_{35\ (\mathrm{Hall})}$) voltage, respectively, during a perpendicular magnetic field sweep (−5 T to 5 T) at 300 K. The subscripts indicate the contact pads shown in Figure 11b. From the longitudinal voltage (V_{34}), the sheet resistance (R_s) was determined at zero magnetic field by Ohms law according to Eq. 2.10, where 'W' and 'L' correspond to the width (140 µm) and length (300 µm) of the graphene area, respectively. The n_s was obtained from the slope of the linear fit between the transversal voltage (V_{Hall}), and the magnetic field (B), according to Eq. 2.11 where q_e is the electron charge (1.6×10^{-19} C) and I_{DC} is the constant DC current, (1 µA). If the slope is negative, the graphene is n-type doped (excess of electrons), while if the slope is positive, it is p-type doped (excess of holes). Assuming the Drude model of conductivity [71], the mobility (µ) was calculated by Eq. 2.12. Finally, the Fermi level, E_F, was calculated from the n_s according to Eq. 2.13, where $\hbar$ is reduced Planks constant, v_F is the Fermi velocity, k_F is Fermi wave vector which is equal to $\sqrt{\pi n_s}$ and n_s = number of additional charge carriers.

$$V_H = I \cdot B/q_e \cdot n_s \tag{2.9}$$

$$R_s = V_{3,4}/I_{1,2} \tag{2.10}$$

$$n_s = I_{DC}/q_e \cdot (\Delta V_H/\Delta B) \tag{2.11}$$

$$\mu_H = 1/q_{e\ \cdot n_s \cdot\ R_s} \tag{2.12}$$

$$E_F = \hbar v_F k_F = \hbar v_F \sqrt{\pi n_s} \tag{2.13}$$

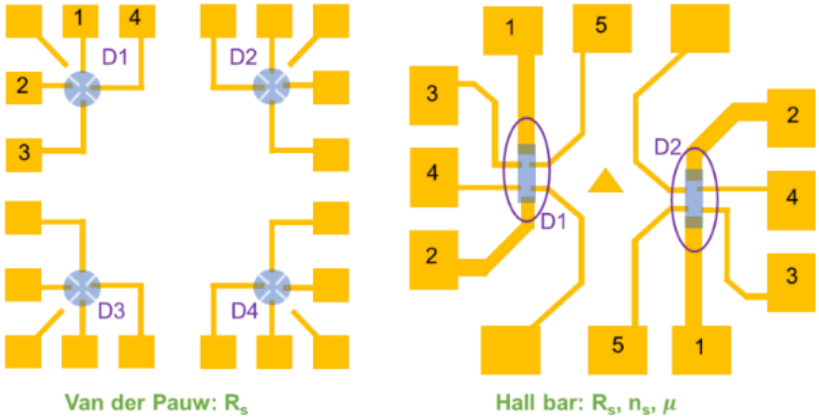

Figure 11 Device designs fabricated in this work. In design A the graphene cloverleaf has a diameter of 300 µm. In design B, the Hall bar has dimensions 140 x 300 µm.

2.3.3 Morphological

SEM

SEM was used in this thesis to investigate properties and structure of materials (MoS_2, dewetted nanoparticles). In this thesis, a SEM (FEI Inspect F) was used for the imaging of CVD grown MoS_2 and dewetted silver nanoparticles in Chapter 3 and for embedded Cu dewetted nanoparticles in Chapter 5.

AFM

Atomic force microscopy (AFM) enables a visualisation of the surface topography at the atomic scale. This technique was used in Chapter 3 to measure the surface roughness of substrates after post-treatment. The principle relies on measuring a mechanical frequency change of an oscillating micron-scale cantilever due to interactions with the surface, such as Van der Waals, capillary or electrostatic forces. In this work an AFM Bruker/Veeco Dimension 3100 was used for topography measurements.

2.4 Transparent optoelectronic and biological applications

The properties of 2D and ultrathin materials, such as large specific surface area, flexibility, electrical conductivity, optical transmittance and reflectance, and tunability together with their unique sensitivity to changes in the environment make them compelling materials for the active components or supporting substrate in applications across a broad range of sectors from electronics, to energy harvesting, storage and conversion, optical displays, biomedicine and health. This thesis is dedicated to the development of low temperature fabrication and processing techniques to obtain 2D materials on substrates of technological interest. Two promising applications are demonstrated: the first is increasing the electrical conductivity of transparent surfaces made of graphene while the second is increasing the antimicrobial functionality of transparent surfaces made of nanostructured copper. The following provides a brief summary of applications of 2D and nanostructured materials that could benefit from the low temperature processing and transfer techniques before reviewing in detail the applications developed in Chapter 4 and Chapter 5.

UTMFs are widely used in transparent optoelectronic applications as transparent conductors (TCs) [48,49] in photovoltaic cells and low emissivity windows [51] as well as plasmonic meta-surfaces [57]. On the other hand, metallic dewetted nanoparticles (DNPs) can be used as a mask to pattern glass surfaces (SiO_2) via reactive ion etching (RIE), allowing the fabrication of large area nanopillars and nanoholes, which have shown unprecedented optical properties such as anti-reflection [72] and increased transparency, as well as self-cleaning properties [73]. Moreover, when large nanopillars are fabricated, surface phonon-polaritons on glass can be excited i.e. increase the optical emissivity in the infrared (IR) optical range, allowing the use of these surfaces for passive radiative cooling [74]. In another example, DNPs can be fabricated with the right dimensions to promote visible light scattering for the fabrication of antiglare surfaces [75]. Finally, antimicrobial metals, for example copper or silver, could be nanostructured on glass substrates for the fabrication of transparent antimicrobial, self-cleaning, anti-viral and antifouling surfaces.

2.4.1 Transparent electrodes

The first application of this thesis is developing highly conductive transparent surfaces that could be used as transparent electrodes. A transparent electrode (TE) is a key component of any optoelectronic or transparent device. With an increasing number of large area applications, there is growing demand to replace the conventional oxide based transparent conducting films with nanomaterials, primarily to reduce the cost. When light photons have to pass through an active material, the electrode(s) hosting the active material must be transparent to light photons. Display screens, for example, use TEs to carry electrical signals while rendering the display visible. Touchscreens, on the other hand, use TEs both to keep the display visible and also to convert touch into electrical signals [76]. Solar cells utilise TEs to collect photons and extract charge carriers generated due to the photovoltaic effect [77]. TEs are also used as transparent heaters in defogging and defrosting applications [78].

In many cases, electrical conductivity and optical transmittance are the most important performance indicators for TCs. Currently, the state of art TEs are large bandgap semiconductors heavily doped with metals, known as transparent conductive oxides (TCOs). TCOs show high transparency in the visible (VIS) range together with excellent electrical properties. Among the TCOs, indium tin oxide (ITO) is the most widely used with a sheet resistance, R_s around 10 Ω/sq. at an optical transmittance, Tr = 85% [79]. However, the use of ITO as a transparent electrode suffers from several drawbacks: 1) it contains Indium, which is a high cost scarce material, 2) it requires complex fabrication and high annealing temperatures to reduce its resistivity making it difficult to integrate at an industrial scale, 3) it is incompatible with certain organic materials (active comments of e.g. solar cells) due to indium and/or oxygen migration from In_2O_3 [80], 4) it is brittle which makes it unsuitable material for flexible applications where bending is desired, and, 5) ITO has a band gap of 3.75 eV (331 nm) which results in absorption of radiation at ultraviolet (UV) wavelengths. In addition, due to plasmon resonances, ITO becomes reflective in near infrared region (NIR) [77]. Thus, the poor, transparency in UV and IR region of the spectrum precludes the use of ITO in certain applications such as (IR) pyroelectric detectors, solar cells for space applications and (UV) photodiodes and LEDs. In this regard, the search for 2D material-based TEs has been developed with primary progress achieved with thin (< 10 nm) metal films [48,81–83], silver nanowire films [84,85], conductive polymers [86–88] carbon nanotube films [89–91] and graphene [92–98].

Pristine graphene has an optical absorption of $\pi\alpha$ = 2.3% per layer. Thus, three layers of pristine graphene could theoretically achieve the industrially competitive standard of 10Ω/sq. at 94% transmittance (equivalent to ITO) [99]. Unfortunately, in practice, the R_s of large area graphene is typically much higher, in the order of ~1-2 kΩ, due to a high scattering rate resulting from wrinkles, defects and domain boundaries. As a result, real graphene films used in devices are not nearly as conductive. The best values reported in the literature are: R_s= 30 Ω/sq. at Tr = 90% for graphene multilayers [100,101], R_s= 125 Ω/sq. at Tr =97.7% [102,103] and 8.8 Ω /sq. at Tr = 84% [104], for chemically doped graphene.

Despite these practical challenges, graphene is still recognised as a promising TE material as it offers superior thermal conductivity and mechanical flexibility enabling more efficient heat dissipation and compatibility with flexible substrates. Furthermore, for some applications such as touchscreens, photodetectors which carry little current, obtaining an ultralow conductivity is less important.

In addition, with recent developments in doping techniques, highly n-doped graphene is promising as low work function electrodes for energy conversion and electron emission applications such as solar cells [105,106] and touchscreens [100]. In Chapter 4, we demonstrate a method of obtaining highly conductive n-doped graphene on glass, while, in Chapter 3 we provide a growth and processing technique for ultrathin materials at low temperatures. This can enable the incorporation of ultrathin materials based TEs on low strain point flexible substrates for a range of emerging flexible optoelectronic and photonic devices in the heath, electronics and energy related industry.

2.4.2 Transparent antimicrobial (AM) surfaces

The second application developed in this thesis are transparent AM surfaces. Transparent touch screen applications is increasingly in demand. Whilst only a decade ago, only smartphones bore touchscreens, nowadays touchscreens can be found in a variety of settings, from train station ticketing machines to self-service kiosks. In parallel, the recent COVID19 pandemic has changed the world attitude towards the hygienic use shared surfaces, which are used by many people in a short space of time and therefore have an increased potential to harbour harmful bacteria. The demand for safer screens has motivated a surge of intense and recent efforts towards imparting antimicrobial functionality into glass, this being the most widely used substrate for touch screens [107].

Whilst historically metals such as copper and silver have been used for their inherent antimicrobial properties [108–111], these metals are not suitable for applications requiring a high level of transparency. In this regard several strategies have been developed with primary progress being achieved by metallic nanoparticle coatings, antimicrobials polymers and photoactivated metal oxide coatings. One market leader in the field is Kastus® Technologies who uses the latter method for AM coatings range. However, due to the high temperature (>600 °C) used for fabrication of the coatings, this option is not suitable for some substrates. Thus, challenges remain in low temperature fabrication for low strain point (glass transition temperature) plastics and thin glass. Chapter 5 provides a full review of the current state-of-the art solutions for transparent AM surfaces and describes the method developed in this thesis to obtain highly durable transparent antimicrobial coating at temperatures <400°C using metal dewetting techniques.

Chapter 3

Low temperature growth and processing techniques for MoS_2 and metal *nanostructures*

The information, text and figures in this chapter have been adapted, under the terms of the Creative Commons Attribution-Non-Commercial license, from the original publications: C. Graham et al. ´´NaCl substrates for high temperature processing and transfer of ultrathin materials´´ Scientific Reports (10)1 7253 (2020) & C. Graham et al. (2023) ´´Durable, transparent and antimicrobial nanostructured surfaces on glass´´ (Under Review).

3.1 Introduction

Ultrathin materials and nano-structures are key elements in developing functional surfaces for, e.g. electronic and optoelectronic devices, display screens, light emitting diodes, smart windows and photovoltaic cells. However, their deposition and processing often necessitate high temperatures, which are not compatible with a direct fabrication onto the target substrate. For example, polymers are widely used as a supporting layer but unfortunately have low strain-point temperatures. In this chapter we develop low temperature growth and processing techniques for ultrathin and nanostructured materials including graphene, MoS_2 and nanostructured metals. In Section 3.2, we overview the fabrication techniques. In Section 3.3 we demonstrate a low temperature fabrication of Copper (Cu) dewetted nanoparticles (DNPs) by a metal dewetting process in order to obtain a coating with a transparency independent of wavelength. The coating is fabricated directly on a low strain point glass substrate that is relevant for use in cover glass for display applications. In Section 3.4 we introduce a novel, simple and fast technique to obtain thin materials and nano-structures requiring high temperature processing onto low strain-point (glass transition temperature) substrates. The innovations presented in this chapter mark progress towards the realisation of functional transparent surfaces on flexible substrates.

3.2 2D materials fabrication techniques

Since the exfoliation of graphene in 2004, and subsequent expansion of the 2D materials family, several techniques have been developed in order to produce high quality 2D materials on a large scale. These techniques are briefly summarized below, focusing mainly on Chemical and Physical Vapor Deposition (CVD and PVD, respectively) processes that also feature in this thesis.

3.2.1 CVD growth

CVD is a chemical process in which the deposition of the target material onto the substrate is controlled by a chemical reaction between powdered and/or gaseous precursors which are heated inside a furnace at high temperatures (>500 °C). Most CVD material growth relies on the pyrolytic decomposition of precursors on the substrate surface after adsorption. The decomposition of the precursor results in the generation of new surface adsorption sites and enables thereby a continuous growth of the desired material. The reaction is performed at temperatures greater than the pyrolytic decomposition threshold of the precursor in order to enable continuous film growth. Figure 12 shows a schematic of the CVD which takes place in the following 3 stages i) adsorption, decomposition, and desorption of precursor molecules on the substrate surface; ii) diffusion and reaction of atoms or molecules from the decomposed precursor on the substrate surface; iii) the nucleation and growth of the 2D material templated by the substrate. The thermodynamics and kinetics of growth, and the resulting material thickness, quality and morphology, is highly dependent on parameters such as precursors used, the carrier gas flow rate, temperature, pressure, and type of substrate.

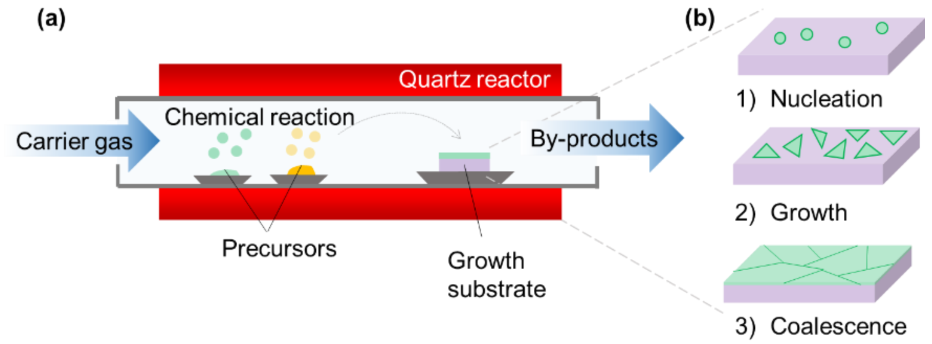

Figure 12 The schematic of a tube CVD system. (b) 2D film growth process: first, the nucleation is formed as the growth centre of grain domains; second, the growth of the 2D grain domains; third, the 2D domains coalesce to form a continuous film

To date, CVD has been employed to grow a range of large-area high quality 2D materials. The most prominent examples include transition metal dichalcogenides, including several to monolayer MoS_2 [112], and graphene [100] where lateral dimensions of up to 6 and 30-inches, have been demonstrated. The development of transfer techniques (detailed in Section 3.4) has enabled the growth materials to be transferred onto a range on functional substrates. Furthermore, with CVD it is possible to directly grow materials on substrates with complex and patterned geometries. Besides the parameters of precursors, temperature and time, CVD techniques have witnessed further advancements with the use of seeding promotors [113], sacrificial layer catalysts [114] and magnets [115] to precisely control the growth and quality of the materials obtained.

3.2.2 PVD techniques: Sputtering & Evaporation

Sputtering is a PVD technique that uses electrical energy to release a material from a source and deposit it onto the substrate. The target material goes from a solid to vapour phase and then back again to a solid phase, as a thin film. The basic operation of sputtering consists of introducing a process gas (Ar in this thesis) into a high vacuum ($\sim 10^{-8}$ Torr) chamber. Then an electric field is applied between the target, which contains the material to be sputtered, and the substrate, as shown in Figure 13a. This electric field ionizes the Ar gas, creating a plasma of Ar^+ ions. These positive charges are accelerated towards the target placed at the bottom of the chamber and collide with the target, detaching particles, which are then deposited on the substrate. The quality of thin films obtained by this method is governed by a number of parameters, including deposition rate, pressure of the process gas, initial vacuum level, and substrate material and temperature, to name a few. In this thesis, we used a computer controlled, automatic RF/DC magnetron sputtering system from AJA International Incorporation.

Thermal and electron beam (e-beam) evaporation are also physical vapour deposition (PVD) techniques. In thermal evaporation, Figure 13b, a solid target is heated to a temperature beyond its melting point, producing the vapor phase of the material, which is then coated onto the substrate in the solid phase. In this thesis, films were thermally evaporated under high vacuum ($\sim 10^{-8}$ Torr) in a system from Kurt J Lesker. In e-beam evaporation, Figure 13c, a high voltage source produces a stream of electrons which bombard and melt the target material producing the vapor phase which is subsequently deposited on the substrate as a solid film. The deposition rate is controlled by the voltage applied to the target material where the voltage is proportional to the thermal energy produced.

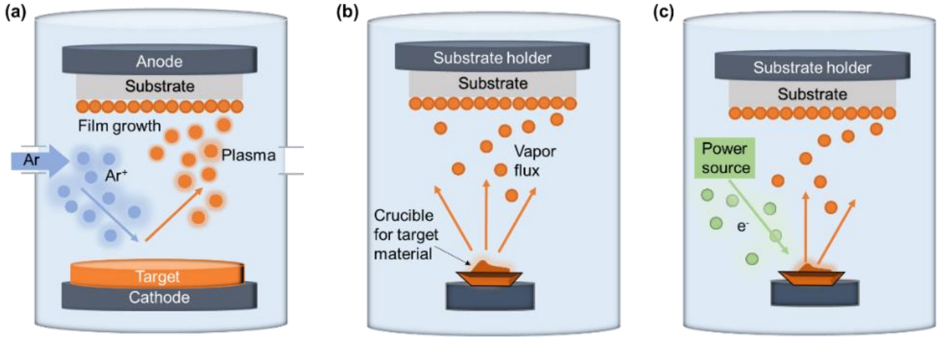

Figure 13 PVD techniques (a) sputtering; (b) thermal evaporation; (c) E-beam evaporation

3.3 A low temperature metal dewetting process to obtain highly transparent DNPs on low strain point glass

Metal dewetting is a low-cost technique to create nanostructured metals on transparent silica surfaces without the need of complicated multistage lithographic techniques [75,116,117]. The dewetted nanoparticles (DNPs) are typically obtained by a rapid thermal annealing process at temperatures in excess of 600°C, as explained in Chapter 2, Section 2.2.2. The resulting DNP array carries a signature extinction (absorbance and reflectance) associated with the plasmonic resonance of the particles. For some applications, it is desirable to reduce the absorption and/or reflection in order to obtain a surface with a high transparency independent of wavelength; i.e. reduce colour. The light absorption, reflection, transmission and colour by the nanoparticles is tunable by the size (diameter) and shape (contact angle) of the DNPs [47]. These parameters can be controlled by the dewetting temperature, the duration of the thermal treatment used to induce dewetting, the initial UTMF thickness and substrate type [118].

In this Section, we utilise a low temperature annealing of Cu UTMFs i.e. sufficiently close to the temperature at above which dewetting of the continuous film is observed and below the glass strain point of the substrate (580°C). By doing so we intentionally introduce a degree of inhomogeneity into the contact angle, size and morphology of the particles obtained such that the plasmonic resonance effect on the colouring of the coating is kept within acceptable values. To provide a comparison and demonstrate the advantage of low temperature dewetting, electromagnetic simulations of the high (750°C) and low (390°C) temperature dewetting cases were performed together with a comparison to the experimental optical spectra. Cu is chosen as the precursor UTMF, but the technique could also be applied to metals such as silver and gold.

3.3.1 Electromagnetic simulation of the individual DNPs

The optical response of individual nanocaps is simulated using the Finite Element Method with commercial COMSOL Multiphysics® software [119]. A 2-D array of nanoparticles was chosen as physical model, considering periodic boundary conditions on the edges of a unit cell. The unit cell is then composed by the substrate, i.e. fused silica, 1-nm thin layer of metallic Ti and a single Cu nanoparticle in air properly shaped. For the nano particles obtained at higher dewetting temperature the period of the system is set to 120 nm. For the lower dewetting temperature case, 230 nm has been used for the periodic condition. The geometric parameters of the unit cell, including particle geometry, particle base diameter and contact angle were considered according to a statistical analysis of the representative sample SEM images Figure 14c, using the Fiji distribution of ImageJ software [120]. The model input parameters are listed in Table 1. The particles were described as spherical nanocaps and assume fixed and average values of the copper-on-silica contact angle and base diameter for high and low temp dewetting cases, respectively. For the high temperature samples, the nanoparticle shape was made to be more rounded and the nanoparticles density lower while the model for the low temperature samples is composed by flattened nanoparticles and higher density. The metal dielectric function for Cu is taken from McPeak et al. [121], the one for Ti from Johnson and Christy [122] while for air we set fixed values of the refractive index (n=1) and extinction coefficient (k=0) and for the substrate n=1.45 and k=0.0001. The mesh chosen is a free-triangular mesh that is finer at the boundaries between different materials with the smallest domain equal to 3nm in the nanoparticle and at the interface between the substrate and air. The wavelength range used for the simulation is 380 – 750 nm with a step of 35 nm. Note that since the theoretical model is based on a simplified 2D array of Cu nanoparticles, it enables a qualitative rather than quantitative comparison to experimental data, whilst still reproducing the experimental trends.

Table 1 Statistical Parameters for two fabricated Samples with UTMF of 3.5 nm Cu annealed at 390 and 750 °C, respectively, as extracted by SEM Image Analysis in ImageJ. Standard deviation follows the '±' symbol.

Annealing temperature (°C)	Average base diameter (nm)	Average particle height (nm)	Average particle contact angle (°)
390	117 ± 38	64 ± 20	35 ± 12
750	62 ± 24	42 ± 21	74 ± 23

3.3.2 Discussion

Experimentally we observed that: (i) low temperature produces flatter particles with a lower contact angle, (ii) particles are much closer together, and in some cases, in contact with each other (Figure 14a), (iii) high temperature annealing produced the typical narrowband resonance centred around 580 nm with pinkish colour while the same process at low temperature produces a broader resonance at longer wavelength with paler bluish colour (Figure 14b). The simulated optical spectra (Figure 14c) are in good agreement to the experimental observations. Without wishing to be bound by theory, it is believed that the broadening and red-shift of the plasmonic resonance in the low temperature annealing case may arise from a combination of two effects: the first may be that low temperature produces flatter particles with a lower contact angle; the second may be that particles are much closer together or in some cases touching (Figure 14a), this being consistent with previous work [47].

The change in particles' structure and associated optical response give the coating a transparency without strong dependence on wavelength. We have also measured low scattering (haze) < 1%. Thus, the colour of the Cu UTMFs as a whole remains visually close to the neutral colour of the substrate against white and coloured text backgrounds and has a transmission between 70-80% that is substantially independent of wavelength in the visible range. The inset of Figure 14b demonstrates that the visual appearance is such that the functionality of transparent devices would be retained.

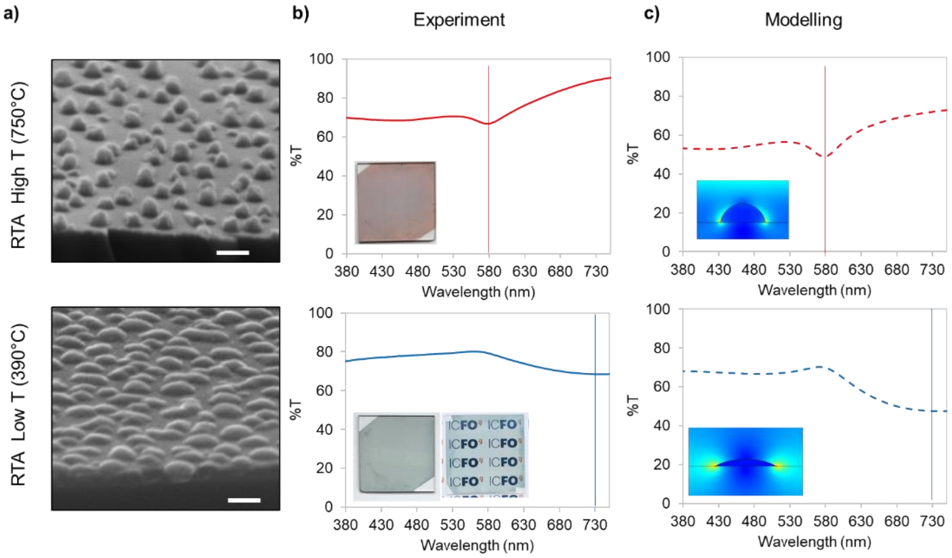

Figure 14 SEM images clearly illustrate the influence of the annealing temperature on the particle shape and size. High temperature produces separate, rounded particles with a contact angle ≈90° whilst low temperature produces, flatter particles, with a contact angle < 90° and that are sometimes in contact. Scale bar = 100 nm. Optical spectra obtained from experiment (b) and modelling (c). Modelling reproduce qualitatively the experiments, in particular the red shift and broadening of the plasmonic resonance due to a reduction of particle's contact angle. Inset of b) shows the colour of the coatings against white background and also against a coloured text background to show transparency and colour neutrality of the dewetted CU UTMFs. The inset of c) shows the particle shape used for the modelling as determined from the SEM images in a.

3.3.3 Applications

The techniques developed in this section would enable the implementation of nanostructured metals onto transparent flexible substrates at low temperatures. Substrates of interest are thin cover glass, typically used for display screens, or plastic substrates for emerging flexible electronics applications. For example, by tuning the metal and additional dielectric thickness and additional function coatings, one can engineer the dimensions of the nanoparticles and the refractive index of the embedding material to create transparent antiglare, antireflection, self-cleaning coatings for display applications on substrates that cannot withstand high temperatures. Other applications can be in transparent sensors and solar cells where, for example, the use of metal nanostructures on the front and rear surfaces or in the bulk of a cell can be used to enhance their light collection efficiency through surface plasmon resonances [123,124]. Finally, an application that is elaborated in Chapter 5, is the use of dewetted Cu UTMFs for transparent antimicrobial coatings for touch-activated displays.

3.4 A transfer procedure for obtaining nanostructured and 2D materials on polymeric substrates

The field of flexible electronics stands to greatly benefit from advances in 2D materials, as the unmatched combination of device physics accessible on flexible polymeric or plastic substrates would enable long sought after large-area high-performance flexible devices. One of the main challenges facing plastic as a next-generation substrate is the substantially reduced processing temperature window. The maximum fabrication temperature is related to the glass transition temperature (strain point) above which plastic deformation takes place and the substrate no longer retains its original dimension. For example, polyethylene naphthalate (PEN) and polyethylene terephthalate (PET) satisfy the requirements for flexible substrates in that they are highly transparent, light, deformable, have low roughness, are inexpensive and highly resistant to chemical/environmental corrosion. However, they can tolerate maximum temperatures of only 160 and 120 °C, respectively. Due to this limitation, high thermal processing materials are typically grown on SiO_2 or sapphire substrates, which can withstand high temperatures, after which they can be transferred onto a flexible substrate.

To this aim, a number of techniques have been developed to delaminate the 2D film from the growth substrate, each with varying degrees of cleanliness, uniformity and transfer related damage. In the following we briefly summarize; (i) etchant based, (ii) dry-transfer, (iii) water-assisted and (iv) salt-assisted techniques, in particular, the processes, advantages, and drawbacks of various transfer methods are discussed. A detailed summary is provided in [125]. Chemical-etchants e.g. hydrofluoric acid (HF), hydrochloric acid (HCl), or nitric acid (HNO_3) or strong bases such as NaOH or KOH, act by etching the substrate from underneath the 2D film, after which it can be transferred to the target substrate. Unfortunately, these etchants are non-environmentally friendly, highly corrosive and often damage or unintentionally dope the transferred film, ultimately leading to reduced device performance [126–130]. Dry-transfer techniques involve the use of adhesive supporting layers e.g. PDMS stamps, metals or other 2D materials to peel-off and separate the 2D material from its growth substrate [131–134]. These techniques unfortunately suffer from lack of control over contamination from the adhesion layer or stress induced film damage upon lift-off or transfer steps. Water-assisted transfer approaches rely on ultrasonication or capillary action to force water into the interface between 2D material and growth substrates [135–137]. This technique is prone to generate cracks and wrinkles in the transferred film [138–140]. Finally, water-soluble sacrificial layers such as NaCl [141–143], PTAS [144], and Na_2S/Na_2SO_4 [145,146] have been reported for the transfer of metals, metal nanostructures, graphene and TMDs. In this technique, the sacrificial material is deposited on the growth substrate prior to the target material. Whilst being etchant- and polymer support-layer-free, the sacrificial layers may not always be suitable for high-quality defect-free growth, potentially causing undesired chemical or catalytic reactions which degrade the material quality. Previously, NaCl has been used as the growth substrate for the semiconducting materials [147], metal oxides [148], magnetic materials [149], metallic films [150,151], nanostructures [152] and graphene [153].

In this work, we develop a novel technique to obtain ultrathin and nano-structured materials requiring high temperature processing onto low strain-point (glass transition temperature) substrates. Our technique utilizes polished NaCl substrates, a well-known material that can stand the high temperatures involved during the growth – up to about 1000 °C - and can provide a fast and clean transfer onto the flexible target substrate due to the easy dissolution of the salt in water. We demonstrate two model systems including thermal dewetting of Au ultrathin metal films and growth of MoS_2 on NaCl at 750 and 650 °C, respectively, and subsequent transfer onto PET film substrates, after which the salt is easily dissolved by water.

3.4.1 Fabrication

NaCl substrates from International Crystal Laboratories with a size of 1 × 1 inches and of 5 mm thickness were used for the Au DNPs, meanwhile for MoS_2, the substrate was diced to 0.5 ×0.5 inches in order to fit the furnace dimension. PET films of 125 µm thickness from Goodfellow Inc. were used as the flexible target substrate. All substrates were sonicated in conventional organic solvents for 10 minutes and dried with a N_2 stream. As it can be observed in the AFM in Figure 15, NaCl substrates were purchased polished, which is translates into a low roughness (RMS (root mean square) = 2.42 nm).

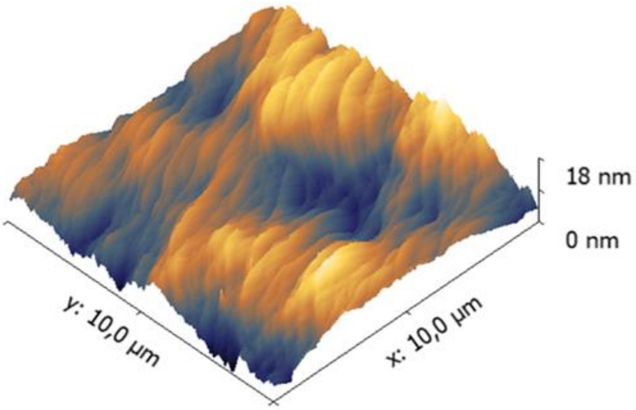

Figure 15 AFM of NaCl substrate after cleaning with organic solvents (acetone and isopropanol).

The substrates were treated in a way that minimises expose to air as much as. If not kept under vacuum, the surface may become rough due to the reaction with humidity. A rougher surface will lead to poorer growth quality. This was avoided by keeping the NaCl in vacuum and properly evacuating the air from the CVD growth chamber.

Ag dewetted nanoparticles (Ag DNPs)

Gold (Au) thin films of 7 nm thickness were deposited onto NaCl substrates using a Lesker thermal evaporator with a deposition rate of 1 Å/s. The continuous films were subsequently dewetted by a rapid thermal annealing (RTP) (TSUNAMI^{TM} RTP-600S) at 750 °C for 90 seconds. The temperature profile and gas flow rate are shown in Figure 16c. A description of the dewetting procedure was explained in Chapter 2 and is elaborated in reference [62].

CVD growth of MoS$_2$

MoS$_2$ was grown as the main product from the reaction between powdered molybdenum trioxide (MoO$_3$) and sulphur (S) precursors by a chemical vapor deposition (CVD) process illustrated in Figure 16b. The NaCl substrate was mounted facing down above a ceramic boat containing 6 milligrams of MoO$_3$ precursor (Sigma-Aldrich, 99.97% purity) and then loaded into the CVD furnace (MTI GSL-1100X-NT-LD). Another boat containing 300 milligrams of sulphur (Sigma Aldrich, 99.98% purity) and a magnet was placed upstream, 18 centimetres from the boat of MoO_3, in order to control the rate of sublimation. Once the substrates and precursors were mounted, a cycle of pumping until 0.1mbar and N_2 flow (10 ml/min) is repeated at least 3 times to remove oxygen from the reactor. The furnace was firstly heated to 300 °C with a rate of 20 °C/min after which the rate was reduced to 10 °C/min to prevent overshooting of the target temperature. Upon reaching a growth temperature of 650 °C, an external magnet was used to push the sulphur containing boat into the reaction zone where the temperature was held at 650 °C for 5 minutes. During the process, nitrogen (99.999% purity) was used as the carrier gas, with a flow rate of 50 ml/min. After 5 minutes, the furnace was left to cool down slowly. Atmospheric pressure was maintained throughout the experiment. The temperature profile and gas flow rate are shown in Figure 16d.

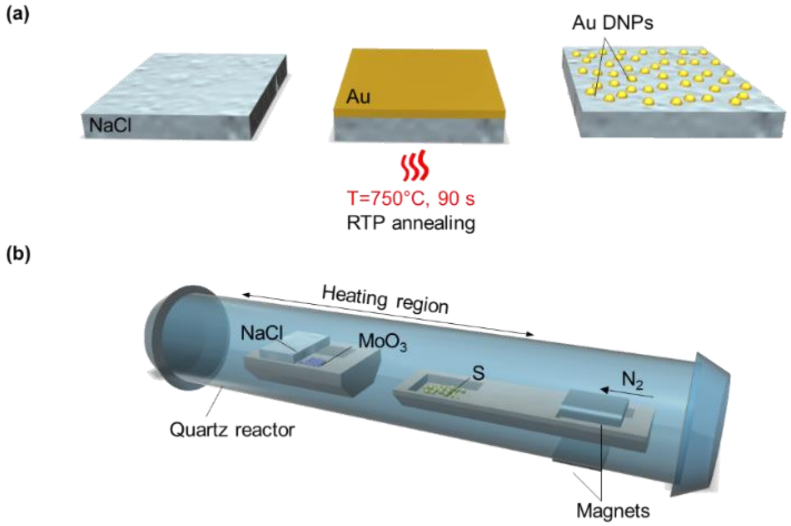

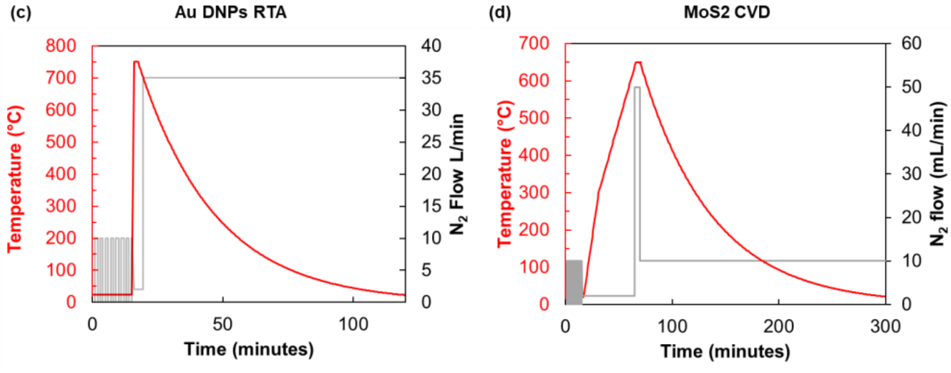

Figure 16 Fabrication of Au dewetted nano-particles (nano-caps) on NaCl by heating a sputtered Au layer of 7 nm thickness at 750 °C for 90 seconds. (b) CVD growth of MoS$_2$ on NaCl substrates due to the reaction of MoO$_3$ with S powder, with the latter being introduced at 650 °C using two magnets. Heating profile and N$_2$ flow rate for (c) Au DNPs and (d) MoS$_2$

3.4.2 Transfer of growth materials

A polymer assisted wet transfer method was used to transfer the MoS$_2$ film and the Au DNPs onto a flexible substrate, PET. Figure 17 illustrates the common transfer process using a PMMA as an intermediate layer. Firstly, a PMMA film was spin-coated at 4000 rpm for one minute onto the sample surface as a support to avoid the disaggregation of both growth materials, MoS$_2$ and Au DNPs respectively, during the transfer. The PMMA layer, with the adhered growth material, is afforded by water intercalation in between the growth material and substrate due to the high solubility of NaCl in water. The substrate is first located on the base of the beaker after which deionised water is slowly added. Once the water level reaches the top surface of the substrate, the release of the growth material occurs gently without inducing cracks or wrinkles. After that, the growth material remains floating on the water surface and it is then located onto the PET substrate. The high surface energy of the free standing MoS$_2$ or Au affords a strong interfacial Van der Waals adhesion between the transferred MoS$_2$ and the PET substrate, preventing the wash out or detachment of the transferred material during the subsequent PMMA removal process. The process was performed at room temperature and was complete within minutes for the samples of 1×1-inch size. After locating the growth material on top of the PET, the PMMA is removed by immersion in acetone and isopropyl alcohol for 10 minutes each. In case of removing PMMA residues, cleaning could be improved by a low power oxygen plasma treatment.

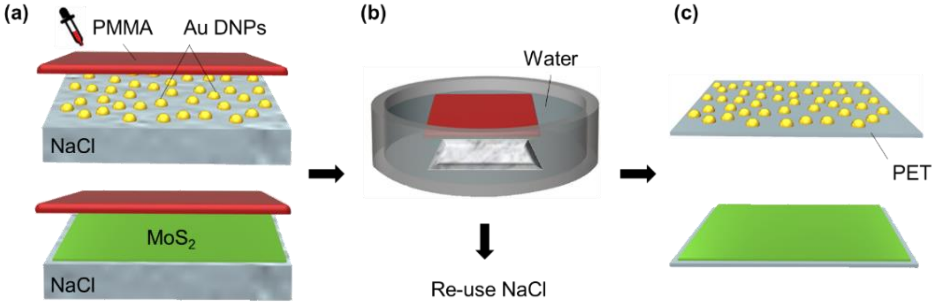

Figure 17 Transfer of Au DNPs and MoS_2 to PET using PMMA as an intermediate layer: (a) Spin-coating of PMMA at 4000 rpm for 1 minute; (b) Partial dissolution of NaCl substrate in water to afford the separation of the growth material covered with PMMA; (c) PMMA with Au DNPs and MoS_2 is located on top of the PET after which the PMMA is removed by immersion in acetone and isopropyl alcohol for 10 minutes each

Thus, our method guarantees easy, fast transfer and, given the 5 mm thickness of the NaCl substrate, there is the potential to re-use the growth substrate by performing a post-transfer surface conditioning procedure.

Figure 18 provides optical images and AFM pictures of the NaCl substrate as received after cleaning, immediately after MoS_2 transfer, and following a rapid thermal annealing surface conditioning treatment at 750 °C for 135 seconds, where it can be observed that the surface roughness is markedly improved to approaching that of the as received substrate.

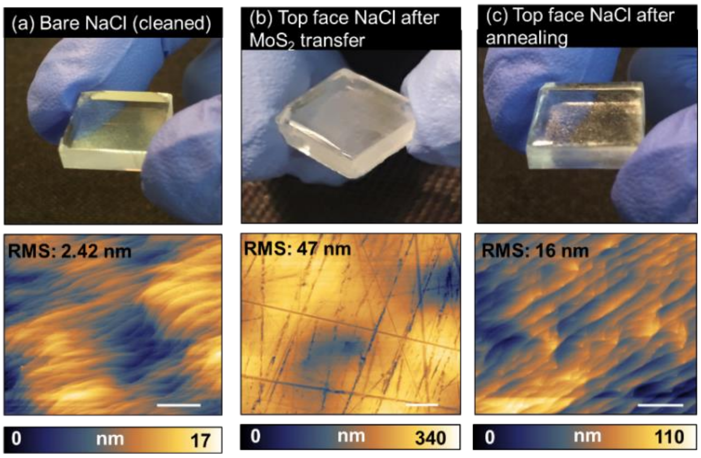

Figure 18 NaCl post-transfer conditioning Photographs (top) and AFM pictures (bottom) of (a) NaCl substrate sonicated in conventional organic solvents for 10 minutes and dried with a N_2 stream, (b) after MoS_2 removal and (c) after post-transfer rapid thermal annealing at 750ºC for 135s. Scale bar: 5 μm.

3.4.3 Quality preservation of transferred nanostructured and 2D materials

For the transfer to be successful, the coverage, morphology, thickness and quality of the material should be well preserved. In this section, we provide the SEM, Raman and transmittance characterisations before and after the transference of Au DNPs and MoS_2 films.

SEM imaging was performed to evaluate the morphology and uniformity of the Au DNPs and MoS_2 films. Figure 19 shows a top view SEM of the Au DNPs and MoS_2 before, Figure 19a&d, and after, Figure 19b&e, the transfer onto PET. In both cases, the structure, coverage and morphology of the materials is preserved. In the case of Au DNPs, Figure 19a&b confirm that the transfer did not significantly affect their size or distribution. Moreover, Figure 19c provides an SEM comparison of Au DNPs on NaCl and fused silica where it is demonstrated that the morphology of the DNPs remains unchanged in each case, differing only in size due to the difference in interfacial energy between the Au and the substrate surfaces, respectively. Regarding MoS_2, the variation in domain size and shape as a function of precursor ratio has been well documented in the literature [154–156] and can vary between hexagonal, triangular flakes and circular truncated and vertical stacks for more supersaturated conditions. In saturated conditions, as in our case where the Mo:S ratio is 1:50, the flakes have coalesced to form larger overlapping regions. This can be seen clearly in Figure 19d&e, which show a continuous film with areas of overlapping domains.

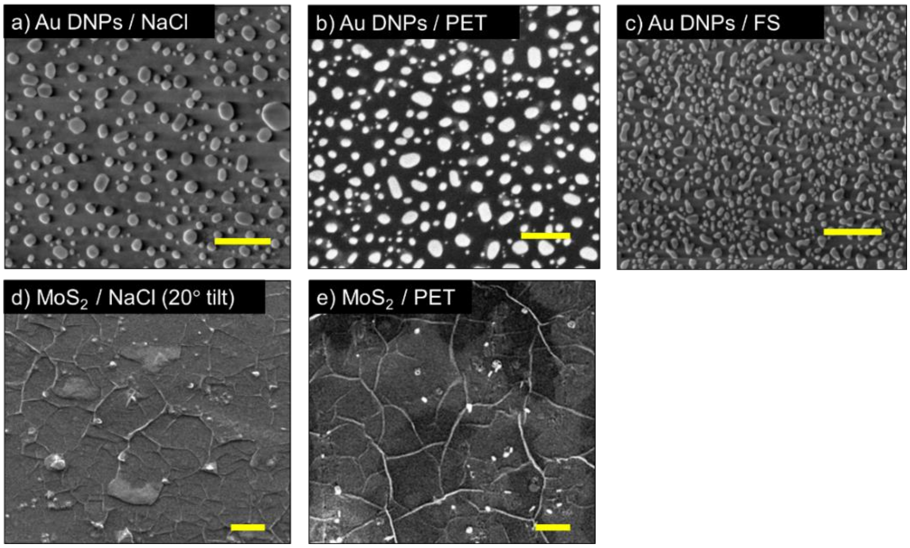

Figure 19 SEM images of (a,d) as-grown and (b,e) transferred Au DNPs and MoS_2 respectively. Scale bar: 2 µm. Note that the different contrast in the top images (a,b) is due to different substrate charging. Figure c provides a comparison to as grown Au-DNPs on a fused silica (fs) substrate.

Raman spectroscopy measurements were performed to identify the quality and layer structure of the as-grown MoS_2, as described in Chapter 2, Section 2.3.1. Single point Raman spectra, Figure 20a, displays the two signature peaks corresponding to the in-plane vibrations of the Mo and S atoms (E^1_{2g}) at ~385 cm^{-1} and the out of plane vibration of the S atoms (A_{1g}) at ~407 cm^{-1} [66]. Raman maps, shown in Figure 20c-d, of 500 µm × 500 µm were obtained. For both the MoS_2/NaCl and MoS_2/PET maps, a relatively uniform distribution and intensity were found with an average $E^1_{2g} - A_{1g}$ peak distance of 22 cm^{-1}, therefore confirming that the MoS_2 film was cleanly transferred with perfect preservation of the coverage, morphology, and thickness. The average peak separation of between 22 and 23 cm^{-1} is indicative of 2–3 layers of MoS_2, in agreement with the SEM micrographs of Figure 19d-e, which indicate several layer-overlapping domains.

Single-point photoluminescence spectra, see Figure 20b, show the characteristic peak of A1 excitonic emission at 1.87 eV for both the pristine and transferred MoS_2 samples, again indicating a damage-free transfer with a good preservation of the sample. Note the absence of the B-exciton peak at 1.98 eV, whose absence has previously been associated with high quality samples [68].

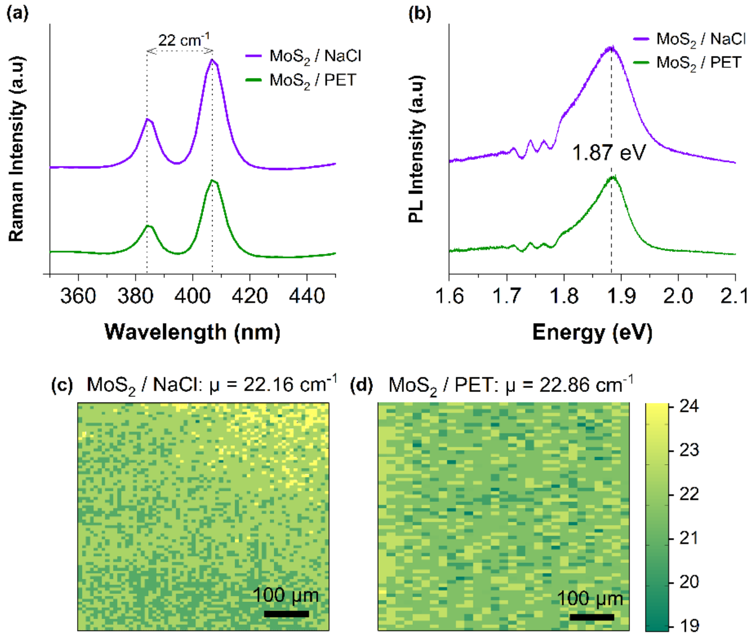

Figure 20 Single point (a) Raman and (b) photoluminescence spectra in the range 1.6 to 2.1 eV before and after transfer. Raman maps for MoS_2 on (c) NaCl and (d) PET. Scale bar: 100 µm.

The transmission of the films was measured in the range 400 – 2200 nm. The results are collected in Figure 21a and Figure 21b for Au DNPs and MoS_2, respectively. All graphs include the transmittance of the bare NaCl (black line) and PET substrate (red line). Transmittance of the samples is preserved in both cases differing slightly due to the transmittance of the respective substrates. In the case of Au DNPs, see Figure 21a, a transmission dip at 600 nm wavelength is present due to surface plasmon resonances [47]. Note that the reduced transmission is compared to Au DNPs on NaCl, which correlates to the reduced transparency of NaCl in the region 500-600 nm. The insets of the Figure 21 show the aspect of Au DNPs and MoS_2, respectively, before and after transfer. The transferred films were completely removed from the growth substrate, leaving no visible PMMA residues and were deposited continuously, as confirmed by Raman mapping.

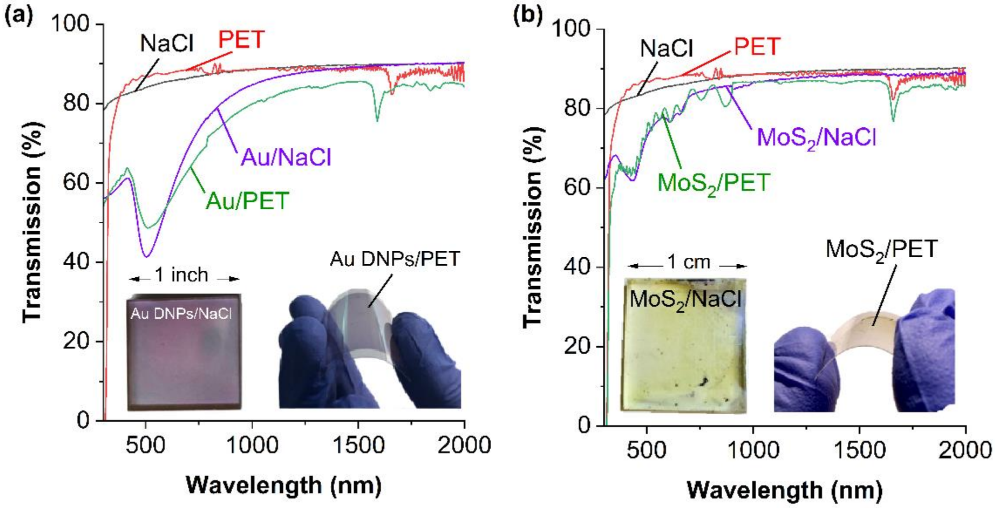

Figure 21 Transmission as a function of wavelength for (a) Au DNPs and (b) MoS_2 on NaCl and PET. Inset shows photographs of Au DNPs and MoS_2 on NaCl and PET substrate.

3.4.4 Applications

The clean transfer of large-area (centimeter scale) CVD-grown MoS_2 and dewetted Au nanoparticles onto arbitrary substrates, including flexible substrates such as PET demonstrates the versatility of the transfer method, allowing for the fabrication of flexible devices. The transfer method will be of interest to the research community working toward the manufacturing of devices based on 2D materials for electronics, optoelectronics and flexible electronics.

3.5 Conclusions and outlook

The techniques presented in this chapter represent important innovations as they can be applied to different material combinations and are not limited by the underlying substrate. In such a way, we open up the possibility to obtain a host of functional, optical and biological surfaces on flexible substrates. Specifically, we demonstrate for the first time the growth of high thermal processing materials, Au DNPs and MoS_2, on NaCl substrates. Additionally, we show a new fast and easy way to transfer the growth materials to low strain point and flexible substrates, such as PET, whilst preserving the film quality. The technique is scalable, easily implemented and etching free. For the case of fabricating metallic nanostructures, increased scalability only requires a larger sacrificial substrate when compared to existing methods such as nano-lithography which is always limited to less than micron size dimensions. Similarly, up-scaling the growth of MoS_2 may be achieved with the use of a larger CVD chamber and consequent optimization of the reactive compounds.

In the future work, this technique could be readily extended to other ultrathin and 2D materials, such as graphene, or for the assembly of vertical hetero-structure systems, thereby offering extended functionality and performance for both fundamental studies and various existing and emerging applications.

The method could also be extended on other growth water-soluble crystalline substrates, such as ZnO. It is well known that, lattice constant matching between the 2D material and the growth substrate is very important for achieving high quality material growth; when the constants differ, strains are introduced into the layer, which leads to defected growth. Due to closer lattice matching of MoS_2 (a=3.212Å) with ZnO (a=3.2495Å) compared with NaCl (a=5.6413Å), ZnO would promote higher quality growth of MoS_2, but since the cost of ZnO substrates is far greater, for this basic study we demonstrated the proof of principle using NaCl.

Chapter 4

Tuning electrical functionality of a transparent surface made of graphene

The information, text and figures in this chapter have been adapted, under the terms of the Creative Commons Attribution-Non-Commercial license, from the original publications: C. Graham et al. (2023) ´´Highly doped graphene on ion-exchanged glass", 2D Mater. ***10*** *035037*

4.1 Introduction

Engineering the doping level in graphene is essential to realizing functional electronic and optoelectronic devices. While achieving strong p-doping is relatively straightforward, electrostatic or chemical approaches to negatively dope graphene have yielded electron densities (n_s) of -9.5×10^{12} cm^{-2} or below. This Chapter presents a method of achieving a very high n_s (-10^{13} to -10^{14} cm^{-2}) in graphene, on an ion-exchanged (IOX) glass substrate, which is widely used in touch screen displays (e.g. smart phones). Moreover, the proposed method, which is easy to implement and scalable, leads to relatively stable graphene doping, with about a 40% increase in sheet resistance over 5 months at ambient conditions. The results presented in this work could enable a route towards a host of previously inaccessible applications of graphene where the reduction of sheet resistance and strong and tunable n-doping is important, such as low work function transparent electrodes for energy conversion and electron emission applications such as OLED, LEDS, solar cells and photonic devices operating in the NIR/VIS wavelength range.

Broadly speaking, graphene doping techniques can be classified in three categories: *i)* substitutional, *ii)* chemical and *iii)* electrostatic. Substitutional doping involves the replacement of one or more carbon atoms with atoms with a different number of valence electrons, e.g boron or nitrogen. It is typically achieved by introducing precursor gases containing boron (HBO_3, H_2B) or nitrogen (NH_3) during the CVD synthesis of graphene [157,158]. Boron has one less valence electron than carbon and p-dopes graphene. Nitrogen, has one more valence electron than carbon, and so is used for n-doping. A drawback of this method is the difficulty in controlling the number of heteroatoms introduced into the graphene lattice, which can compromise the accuracy and repeatability of the doping level achievable by this method [159]. Additionally, the incorporation of heteroatoms can induce lattice strain effects and structural defects, which can eventually compromise the conductivity of graphene thus limiting its use in electronic devices [160]

Chemical doping techniques refer to the adsorption to the graphene surface of strong electron withdrawing or electron donating groups [161]. The technique relies on the charge transfer process taking place at the adsorbate/graphene interface. Some examples of chemical doping are the adsorption of HNO_3 (p-doping) [162], NO_2 (p-doping) [163], H_2O (p-doping) [163], ethanol (n-doping) [161] and NH_3 (n-doping) [164]. One drawback related to this method of doping is that it is difficult to control the surface coverage and reactivity of the chemical species adsorbed onto the graphene (e.g., HNO_3 and $AuCl_3$). This can lead to difficulty in controlling the doping level and instability of the doping over time [165].

Electrostatic doping is a technique in which the graphene doping level is modulated by application of a gate voltage where the polarity and value of the gate voltage determines the type and strength of doping. This technique allows for a degree of reversible and accurate control of the doping. This is typically performed in back or top gated device configurations depending on the nature of the substrate. One drawback is the relatively low reachable n_S - maximum 10^{13} cm^{-2} due to the limited capacitance of the available solid-state thin film or electrolyte capacitors (e.g.300 nm-thick SiO_2 grown on Si). The capacitance can be increased by reducing the thickness of the SiO_2 dielectric[166]. However, SiO_2 is prone to dielectric breakdown at gate voltages required for achieving high doping. In this respect, the use of thinner or higher dielectric constant materials (e.g. MoS_2, h-BN), oxides (e.g. HfO_2, ZrO_2, Al_2O_3), ionic liquids or polymers have been considered for achieving high doping [167–169]. However, there remains challenges to reduce the influence of the target substrate or dielectric on the doping of graphene.

Moreover, while achieving strong p-doping is relatively straightforward, accessing high and stable n-type doping in graphene is challenging on two fronts. The first is that it is difficult to prevent graphene from process related p-doping that can arise from its reaction with chemical resists, metal etchants and polymer residues [170–172]. The second concerns the stability of n-type doping as graphene reacts with moisture and oxygen in the atmosphere causing it to become p-doped. Despite these challenges, significant efforts are being made towards engineering high levels of n-type doping in graphene as it would provide a route towards a host of previously inaccessible applications, including photonic devices operating in the NIR/VIS wavelength range, low work function transparent electrodes for energy conversion and electron emission applications such as Organic Light Emitting Diodes (OLEDs) [173–175], Light Emitting Diodes (LEDs) [97], solar cells [105,106,164] and touchscreens [100].

Electrostatic and chemical doping techniques have so far yielded electron densities (n_s) of -9.5×10^{12} cm^{-2} or below. In light of this limitation, several works have demonstrated graphene doping after its transfer onto appropriately treated substrates. For example, the deposition of ammonia or aluminium on the surface onto SiO_2 substrates led to formation of positive ($NSiO^+$) and negative ($AlSiO^-$) surface charge layers on the substrate which were shown to induce the electrostatic n- and p-doping of graphene, with n_S of $-8.62x10^{12}$ and $2.17x10^{12}$ cm^{-2}, respectively [176].

More recently, n-doping of graphene has been demonstrated on multicomponent glass where the ions are exploited to n-dope graphene to a level sufficient to reverse environmental and process related p-doping [177]. Similarly, sodalime glass (SLG) has been used to obtain highly n-doped graphene, in the order of -1.33×10^{13} cm^{-2}, where it was proposed that the high surface density of Na in SLG dopes the graphene via electron transfer [178].

This Chapter describes, for the first time, a method to obtain highly n-doped graphene with carrier densities (n_s) in the order of -10^{13} to -10^{14} cm^{-2} by transferring graphene (e.g., pristine graphene) onto ion-exchanged (IOX) CORNING® GORILLA®GLASS substrates, widely used in touch screen displays (e.g. smart phones). This glass contains potassium ions (K^+) from an ion exchange process in which some of the sodium ions (Na^+) at the glass surface are replaced by K^+. The depth of the exchange layer (referred herein as 'IOX thickness') can be modified from 5 to 50 µm.

4.2 Fabrication of devices

Two types of devices were fabricated on IOX Corning® Gorilla® glass, fused silica (FS) and Si/SiO_2 substrates for electrical measurements. Van-der-Pauw devices, shown in Figure 22 (left), features four identical devices (D1 - D4) with the typical cloverleaf geometry for performing sheet resistance measurements. Hall bar devices, shown in Figure 22 (right), features two identical devices (D1 and D2) with Hall bar geometry for performing transport measurements. To allow for statistical descriptions, multiple samples of each design were fabricated. Both devices follow the same fabrication procedure outlined in the following, with the addition of Al_2O_3 device encapsulation for the Hall bar structures.

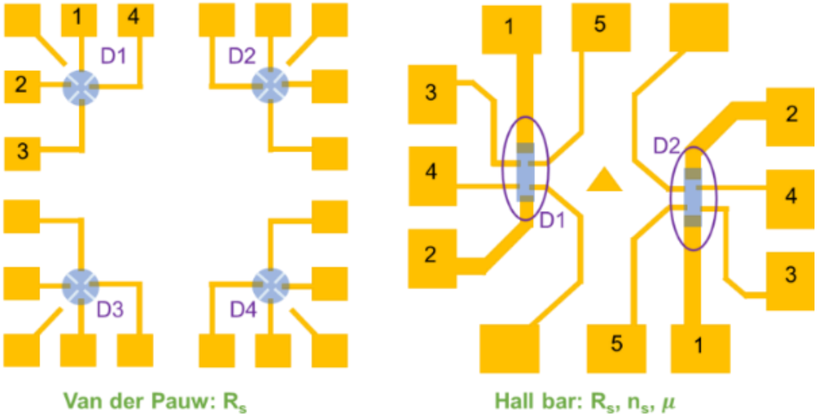

Figure 22 Device designs fabricated in this work. In design A the graphene cloverleaf has a diameter of 300 µm. In design B, the Hall bar has dimensions 140 x 300 µm.

All experiments have been carried out with graphene grown by chemical vapor deposition (CVD) purchased from Graphenea. The graphene sheets were transferred using a wet-transfer technique [179] onto FS, Si/SiO_2 or IOX Corning$^{\circledR}$ Gorilla$^{\circledR}$ glass substrates. Prior to graphene transfer, the substrates were cut to a size of 1 cm^2 and cleaned in an ultrasonic bath using acetone and isopropyl alcohol for 5 minutes in each solvent. Then, Ti/Au (3/50 nm) contacts were fabricated with Van-der-Pauw or Hall bar geometry by photolithography and lift-off processes. CVD graphene was transferred to the metallized substrates which were subsequently dried under atmospheric conditions for 12 h and later immersed in a bath of acetone to remove the PMMA residues. A photolithography process and subsequent Argon/Oxygen etching step was performed to reduce the area of the graphene to a 300 µm diameter cloverleaf in Van-der-Pauw devices and a 140 x 300 µm rectangle in the Hall bar devices, respectively. Remaining photoresist was removed by immersing the samples in acetone for 2 minutes. Finally, the Hall bar devices were encapsulated with 40 nm Al_2O_3 by atomic layer deposition and a final photolithography and subsequent etching process were performed to remove the excess Al_2O_3. The etching was performed by dipping the samples in a buffered HF oxide etchant solution (BOE, HF: NH_4F, 1:7) for 1 minute.

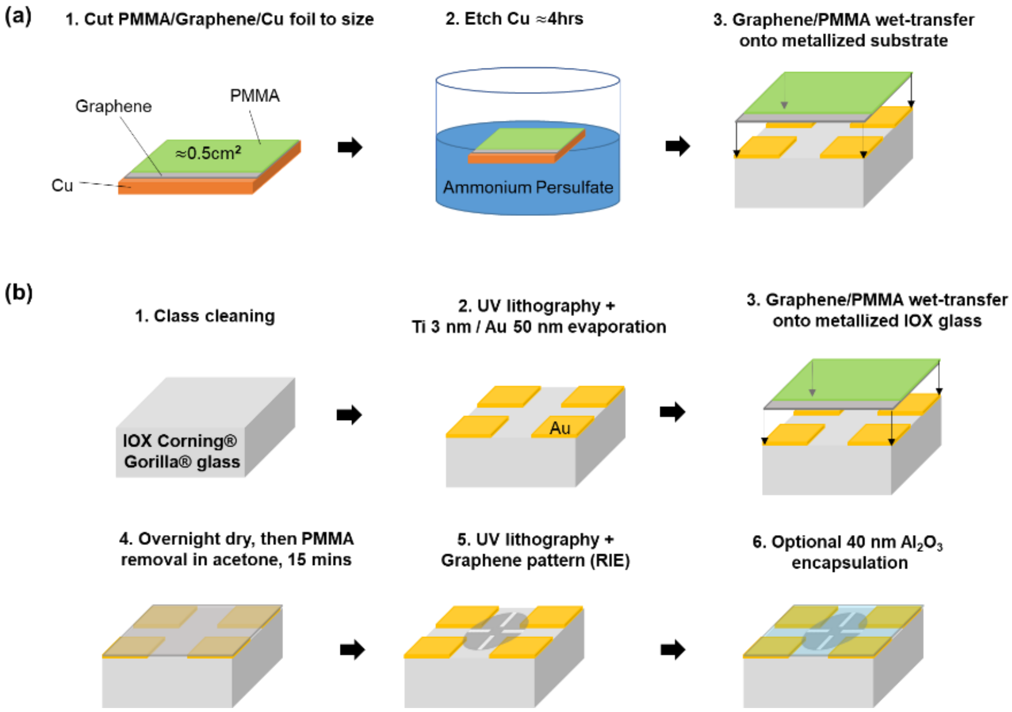

Figure 23 Procedure for the graphene device fabrication: (a) Wet graphene transfer (1) Cut PMMA/Gr/Cu foil to approx. 0.5cm^2 in size. (2) The foil is floated on top of ammonium persulphate for approximately 4 hours to etch the Cu from underneath the graphene. (3) The resulting PMMA/Gr stack is wet transferred onto a metalized substrate; (b) (1) Initial cleaning of substrates is by organic solvents acetone and isopropanol. (2) UV lithography and evaporation of the metal contacts (Ti 3 nm / Au 50 nm) (3) Graphene transfer onto metalized substrates by wet etching process. (4) Samples are left overnight to dry after which PMMA is removed by immersion in acetone for 15 minutes. (5) A second lithography step is performed to reduce the graphene contacts area, removing the excess by reactive ion etching (RIE). (6) Hall bar devices were encapsulated with 40 nm Al_2O_3 by ALD deposition. A final lithography step is performed to remove the Al_2O_3 from the top of the Au contacts by dipping the samples into a BOE solution.

4.3 Characterisation of devices

4.3.1 Electrical characterisation

The electrical measurements have been previously explained in Section 2.3.2. Figure 24 shows a sketch of the graphene transferred onto IOX Corning® Gorilla® glass (a) and fused silica (FS) glass (b) where blue shaded area comprises the silica matrix.

Sheet resistance measurements

The four-point R_s of all Van-der-Pauw devices (comprising 16 on IOX and 16 on FS) was measured. For each device, the I-V curve was measured several times to ensure repeatability, sampling at 1 mV steps, which were subsequently averaged. A linear fit was applied to the I-V curves collected for all devices on each substrate, from which the average R_s was obtained.

Figure 24c compares the I-V characteristics for Van-der-Pauw devices prepared on $IOX_{20\mu m}$ Corning® Gorilla® glass and FS substrates, where the difference in slope confirms the strong influence of the supporting substrate on the sheet resistance of graphene. The corresponding average R_s (obtained from the slope of the linear fit of the I-V curve) of the graphene/FS devices was 1.22 ±0.353 kΩ/sq. which is similar to those values previously reported [180], thus confirming the reliability of our transfer technique and characterization method. On the other hand, the R_s for the graphene/$IOX_{20\mu m}$ devices was consistently 3-5 times lower with an average of 0.245 ±0.069 kΩ/sq. The results were quite repeatable across all devices fabricated by independent runs. The low R_s is in and of itself of great interest, as it supports the use of graphene on IOX substrates as a transparent conductor [181] and other applications requiring low R_s such as low work function electrodes [182].

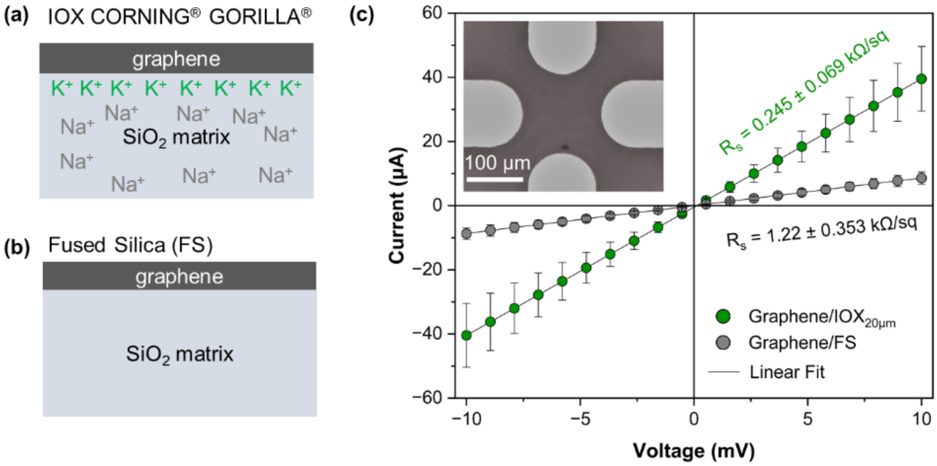

Figure 24 Sketch of graphene transferred onto IOX Corning® Gorilla® glass (a) and fused silica (FS) glass (b) where blue shaded area comprises the silica matrix. The top surface of the IOX Corning® Gorilla® glass contains potassium (K+) from an ion-exchange procedure, where the depth of layer can be modified from 1 to 50 µm; (c) I-V characteristics measured for graphene on IOX20 µm Corning® Gorilla® glass (green circles) and FS (black circles) substrates. For each device, the I-V curve was measured several times to ensure repeatability, sampling at 1 mV steps, which are subsequently averaged. A linear fit was applied to the I-V curves collected for all devices on each substrate (totalling 16 IOX and 16 FS devices), with error bars representing the spread in the data. Note that the error bar for graphene/FS is not visible because of the low standard deviation. The average Rs was obtained from the slope. The inset of the graph shows an optical microscope image of a real sample. Scale bar 100 µm.

R_s measurements were also performed on graphene transferred onto bare (i.e. with no pre-defined Au contacts) substrates. For this experiment, graphene was wet transferred onto bare 1x1cm^2 IOX Corning® Gorilla® Glass or fused silica (FS) substrates as described in the fabrication methods, Section 4.2. The sheet resistance of the graphene (Rs) was measured with a four-probe point probe in colinear configuration, as described in Section 2.3.2. Four samples on IOX Corning® Gorilla® Glass and four samples on FS were prepared. Several measurements were taken per sample to ensure repeatability. The value of R_s reported in Table 2 is the average for all samples of each substrate.

Table 2 Rs of graphene measured by in using the 4-point probe method in co-linear orientation.

	Rs kΩ/sq.	**Standard deviation**
IOX 20 µm	1.32	0.7
FS	1.39	0.4

Interestingly, and in contrast to Au-contacted graphene devices (Figure 24c), no difference in R_s was found, irrespective of the underlying substrate with both IOX and FS systems measuring between 1-2kΩ/sq., Table 2. This result was repeated several times by independent fabrication processes.

Hall measurements

Eight samples on $IOX_{1\text{-}43\mu m}$ were fabricated with a Hall bar design, Figure 11b, where each sample contains two identical devices (D1 and D2) for gathering statistics. The Hall measurement was previously explained in Section 2.3.2 Figure 25a-b show the measurement scheme and the evolution of Hall voltage (V_{Hall}) as a function of perpendicular magnetic field sweep (B) between -5 and 5 Tesla at 300 K.

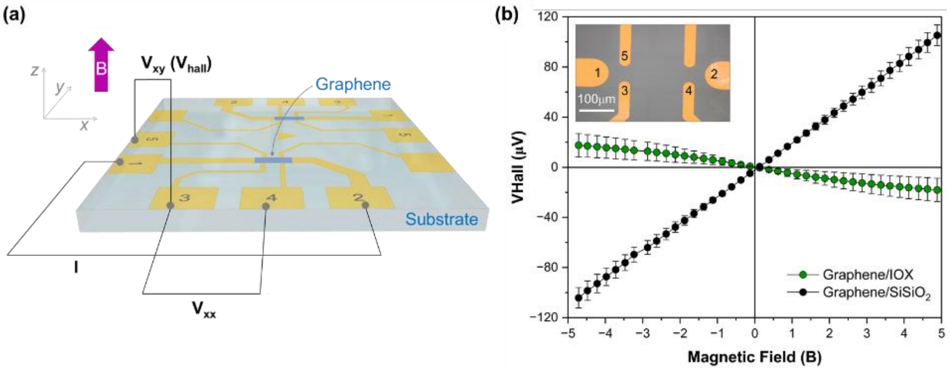

Figure 25 Simplified three-dimensional views of the Hall bar structures, along with circuits for the Hall effect measurement. The heavy purple arrow indicates the direction of the magnetic field corresponding to the circuit diagrams shown. A constant DC current of 1µA was injected through the sample via probes “1-2” whilst probes “3-4” or “3-5” were used to measure the R_S or V_{Hall}, respectively during a perpendicular magnetic field sweep (−5 T to 5

T) at 300 K. (b) V_{Hall} vs. magnetic field (B) data obtained from 16 graphene/$IOX_{1\text{-}43\mu m}$ devices (green circles) and 2 graphene/Si/SiO_2 devices (black circles) where the dotted line represents a linear fitting of all devices. *Note that the IOX data does not distinguish IOX layer thickness because the n_s was not influenced by the depth of exchange and, by deduction, the V_{Hall} was found to be independent of the IOX thickness. The inset of the graph shows an optical microscope image of a real sample. Scale bar 100 μm.

A negative slope indicates n-type doping (excess of electrons), while a positive slope indicates p-type doping (excess of holes) where the magnitude of the gradient correlates to the strength of the doping. Comparing the slope of the devices fabricated on $IOX_{1\text{-}43\mu m}$ to that of the Si/SiO_2 reference, it is found that V_{Hall} induced by the charge carriers in the graphene on IOX substrates is lower in amplitude and of opposite sign, for a fixed current and magnetic field.

Figure 26a-c shows the evolution of R_s, μ_H and n_s respectively, for the eight graphene/IOX samples, comprising of IOX thicknesses: 1x1μm, 1x5 μm, 2x10 μm, 2x20 μm and 2x43 μm. Each marker and corresponding error bar represent the average and standard deviation of D1 and D2. Identical measurements on the Si/SiO_2 reference sample are indicated with blue markers. Note that the low R_s (and high n_s) is reproduced with a comparable magnitude irrespective of the IOX thickness.

The sheet resistance measurements shown in Figure 26a show an average R_s value of 0.318 ± 0.078 kΩ/sq. for the graphene/$IOX_{1\text{-}43\mu m}$ devices. This is in close agreement with the R_s statistics obtained with the Van-der-Pauw structures (0.245 ± 0.069 kΩ/sq.) and confirms that the effect of the underlying substrate is significant and independent of the slight processing differences between the two designs e.g. encapsulation with Al_2O_3. Furthermore, the R_s for the Si/SiO_2 reference, 2.32 ± 0.690 kΩ/sq., is of the same order of that for graphene/FS devices fabricated with Van-der-Pauw geometry (1.22 ± 0.353 kΩ/sq.).

The room temperature (RT) carrier mobility (μ) measurements, in Figure 26b, show a mobility between 80 – 800 and 150-160 $cm^2/V\cdot S$ for graphene on IOX and Si/SiO_2 substrates, respectively. Graphene wet-transferred onto Si/SiO_2 substrates typically produces mobility values in the range of 10^2-10^3 $cm^2/V\cdot s$ at 300 K for a carrier concentration, n_s $\sim 10^{12}$ cm^{-2}

[180,183,184]. In the future, we will perform studies and evaluate previous techniques to reduce the spread of the mobility we have observed toward the highest values observed in the literature for glass [185–187].

The carrier density measurements (n_s) shown in Figure 26c show a moderate p-doping (average n_s $+3.9\times10^{13}$ cm^{-2} ± $1.3x10^{13}$ cm^{-2}) for the graphene/Si/SiO_2 devices (blue marker). The doping may depend on processing conditions and is consistent with data previously reported in graphene−silica systems [171,188–193]. In contrast, the graphene/$IOX_{1-43\mu m}$ devices, indicated with red markers, show a strong n-doping within range -1.7×10^{14} to -4.5×10^{14} cm^{-2}, with an average of $-1.9x10^{14}$ ± $-9.8x10^{13}$ cm^{-2} which validates the effect of the IOX layer on the graphene doping. From the average n_s value, the Fermi level (E_F) was calculated to be -1.61 ± 0.4 eV for the graphene/$IOX_{1-43\mu m}$ devices.

The observed high n_s might be related to a local surface density of positive charge present in the IOX glass layer in which the graphene is in direct contact. A positive surface charge might originate from the excess of K^+ after the ion-exchange process [194,195]. When the graphene is contacted, electrons are drawn into graphene to neutralize the excess surface charge due to IOX process. Similar examples have been reported in literature where it is demonstrated that a charged substrate surface induces the doping of graphene [176,196]. Although it is clear that the IOX glass is a key element to achieve doping, additional experiments are needed to confirm the doping mechanism and the interplay between the processing steps to make the devices and the substrate composition [170–172,197].

To evaluate the stability of the doping, the R_s of several IOX and Si/SiO_2 devices was measured again after being kept for five months in a dry box. The IOX devices (purple markers in Figure 26a) reveal an increase between 0.100 to 0.160 kΩ/sq. corresponding to a 42 % average increase as compared to the initial R_s. The Si/SiO_2 devices reveal a similar increase of ~0.100 ±0.8 kΩ/sq, corresponding to a 5% average increase compared to the initial R_s. Given that the increase in R_s after 5 months is of a similar magnitude for both IOX and Si/SiO_2 devices, we understand that the 42% increase for the IOX is only large in the context that the initial starting R_s was low. We believe that the increase in R_s after 5 months is probably not due to the IOX substrate, but more likely related with a combination of atmospheric exposure, which is known to degrade the graphene, and degradation induced by the Al_2O_3 encapsulation layer. In this regard, future work should consider alternative encapsulation techniques that maintain an effective moisture barrier and therefore the initial quality of the transferred graphene over time.

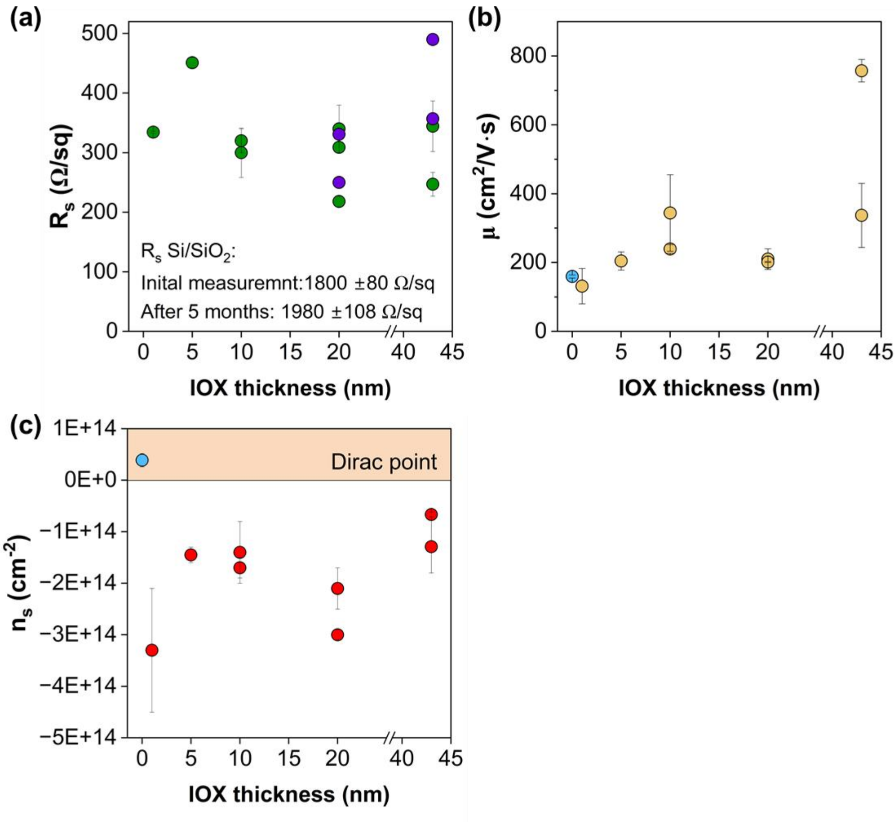

Figure 26 The evolution of (a) Rs (b) μ_H and (c) n_s with IOX layer thickness. Each marker and error bars represent the average and standard deviation of D1 and D2. Samples included in the statistics are 1x1 µm, 1x5 µm 2x10 µm, 2x20 µm and 2x43 µm. In graph (a) purple markers represent the Rs for the IOX devices remeasured after 5 months. The corresponding values for the Si/SiO_2 reference sample is provided in the inset of graph a. The values of μ_H and n_s for the Si/SiO_2 reference samples are indicated with blue markers in graphs b and c. In some cases, the error bars were smaller than the markers and are not visible.

4.4 Applications and future work

The results presented in this Chapter could enable a route towards a host of previously inaccessible applications of graphene where the combination of low sheet resistance, strong n-doping and high E_F, obtained on a transparent glass substrate, are important. For example, one application could be low work function transparent electrodes for energy conversion and electron emission applications such as OLED, LEDS, and solar cells. Secondly, the demonstrated high n_s, corresponding to E_F of -1.61 eV, could be interesting for plasmonic applications, which for graphene devices has so far been limited to mid-infrared and longer wavelengths [198–201]. As frequency of plasmonic excitation scales according to $\sqrt{E_F}$, the graphene/IOX system could be subsequently nanostructured into, for example, nanodisk or nanoribbon geometries, for making plasmonic devices operating in the near-infrared region.

4.5 Conclusions and outlook

As described herein, IOX Corning® Gorilla® glass was found to naturally modify graphene doping without the need of additional post-treatment (e.g. thermal poling under applied potential). Sheet resistance and Hall measurements performed at room temperature demonstrate high and reproducible doping levels of graphene placed in direct contact with IOX glass leading to graphene with an unexpectedly high n_S (-10^{13} cm^{-2} or higher). The negative values obtained with IOX glass were found to be 1-2 orders of magnitude larger than the positive values on undoped silica glass substrate.

Chapter 5

Highly transparent, antimicrobial and durable copper nano-structured surfaces on glass

The information, text and figures in this chapter have been adapted, under the terms of the Creative Commons Attribution-Non-Commercial license, from the original publications: C. Graham et al. (2023) ´´Durable, transparent and antimicrobial nanostructured surfaces on glass´´ Under Review.

This chapter presents an application of the low temperature metal dewetting process introduced in Chapter 3. The work described in this chapter and partly in Chapter 3 was performed with other members of the Optoelectronics group, in particular Alessia Mezzadrelli, and also in collaboration with Corning Incorporated. I fabricated the majority of the samples and I contributed to the design, optical measurements, data analysis and paper writing.

Shared touchscreen environments are becoming ever prevalent in our advancing society, facilitating the way we buy tickets, order food, and provide feedback to name a few examples. However, their frequent use by hundreds of people in a short space of time, provides the perfect environment for harbouring harmful germs and bacteria. Moreover, in these applications, where repeated spray-based sanitisation methods are impractical, the need for transparent surfaces to inherently be antimicrobial has become important. This chapter implements the low temperature fabrication of metallic nanostructures described in Chapter 3 to obtain transparent coatings with antimicrobial (AM) functionality that are also durable and long lasting. The coatings are easy to clean, maintain their AM functionality, optical and wetting properties over a long period of time, whilst also being fabricated in a way that is industrially scalable. We anticipate this innovative method of imparting AM function into transparent surfaces will be useful in many applications of technological interest such as touch-enabled public displays. This work has resulted in the filing of a Patent application in 2023 entitled *"Antimicrobial surface with high transparency and durability using discontinuous metal islands"*.

5.1 Introduction

The COVID19 pandemic highlighted the potential of surfaces to harbour harmful microorganisms by contamination with infectious droplets from sneezing, coughing, speaking and breathing. Now more than ever, the importance of effective disinfection practices for surfaces with constant and repeated use has become a priority. In the first instance, surface contamination is combatted by spraying the surface with an alcohol-based disinfectant, soap or antimicrobial wipes. While effective in the short-term, these procedures are impractical for multi-user surfaces and require continuous re-application to clear any microbes present on the surface. Furthermore, the chemicals in sanitisers are damaging to water streams, detrimental to indoor air quality and are often packaged in non-recyclable bottles that end up in landfills. Accordingly, a need exists for functional surfaces that are persistently antimicrobial, resistant to general use wear-and-tear and sufficiently transparent to retain their functionality. Transparency typically includes high light transmission combined with low scattering (haze). In the following we provide a brief overview regarding the current status of transparent AM surfaces with particular attention to technologies developed for touch screen application.

5.2 State of the art AM Solutions for display and touchscreen applications

The strategies that have been developed to impart AM functionality into transparent surfaces can be broadly divided into 4 categories, outlined in Figure 27, where green text indicates most popular commercially available products. The following provides a brief overview of each method. Table 3 presents a non-exhaustive list of commercial AM screen protection technologies for mobile devices, laptops, tablets and kiosks.

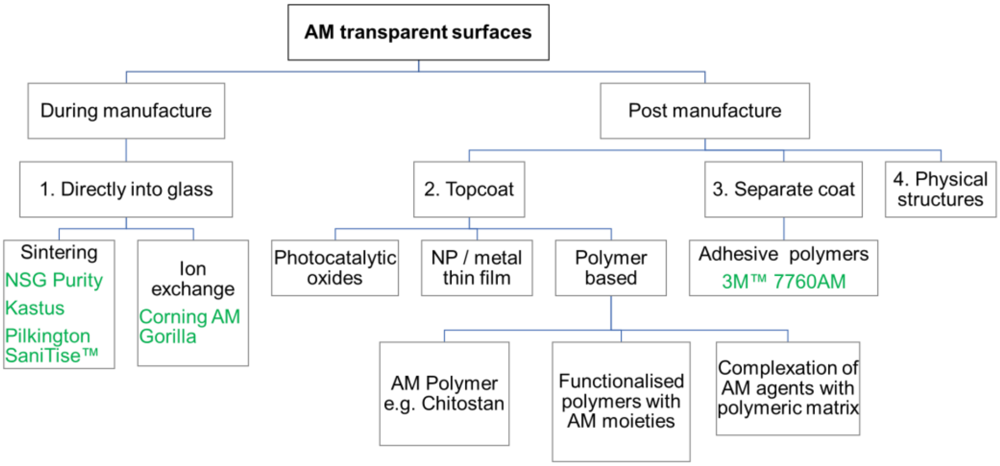

Figure 27 Strategies to impart AM function into transparent surfaces. Green text indicated commercial products referenced in Table 3.

5.2.1 Sintering and Ion-exchange processes

These methods require infusing various AM agents, typically silver (Ag) or copper (Cu) in the form of nanoparticles (NPs) or photocatalytic metal oxides films, e.g. titanium dioxide (TiO_2) or zinc oxide (ZnO), directly into the glass surface during manufacture. This can be achieved by either sintering or ion-exchange processes. The process of sintering involves the application of the AM agent onto the glass surface through either spray or dip coating. The coating is then annealed to temperatures in excess of 600

°C. The high temperature facilitates the creation of a durable, permanent hard coat in the top layer of the glass [202,203]. Conversely in ion-exchange processes, the AM agent integration is achieved through a chemical infusion process. The glass is heated inside a bath containing Ag/Cu salts. Diffusion gradients drive the exchange of Cu^{2+}/Ag^{+} ions into the glass surface with the simultaneous out-diffusion of Na^{+} ions. Thus, an AM layer comprising a few microns deep is formed in the surface of the glass [204,205].

Both sintering and ion exchange produce highly durable coatings, which may be over-coated with functional layers for example, anti-fingerprint (AF) coatings. Sintered coatings have witnessed huge success in the market place with current world leader Kastus, employing this method for its AM display glass [206]. Pilkington and NSG have also developed silver ion-containing sintered AM coatings. Meanwhile Ion-exchange is the technology behind world leading 'Antimicrobial Corning® Gorilla® Glass', that is widely used as a cover glass for display applications.

Despite their success and easy implementation with existing glass manufacturing infrastructure, both strategies come with several limitations. Firstly, the use of silver as a raw material introduces significant cost considerations. Secondly, the high processing temperatures required for fabrication, precludes the use of these techniques for emerging flexible display modules. In this regard, alternative strategies (2-4 in Figure 27) have been developed for post-glass manufacture.

5.2.2 Coating methods

In a second approach the AM agent may be contained within a coating that is fabricated on top of the glass substrate. The use of polymers has received great interest as they are a low-cost option, that can be easily prepared and functionalized, by solution processes without the need of high temperature or vacuum deposition methods [207]. Polymer-based coatings can be further subdivided into; *(a)* application of polymers that have an intrinsic AM function e.g. Chitosan *(b)* incorporation/complexation of the charged AM agent (metallic ions, metals, metal oxides, nanoparticles) into the polymer matrix [208–210], or in a nanocomposite with SiO_2 [211–215] and *(c)* functionalization of the polymer with AM agents e.g. quaternary ammonium compounds (QACs) [216].

By loading or embedding AM agents into supporting polymers, the release of Cu ions can be controlled. The intentional prolongation of ion release confers sustained AM functionality, maintaining the coatings efficacy over an extended period. However, despite their popularity and recent success in the marketplace [217,218], polymer coatings are often not practical under conditions where chemical durability is desired. Moreover, the inherent durability of the polymer is less than that of the underlying glass, potentially limiting the overall product´s lifespan.

5.2.3 Separate coating

In this method a plastic/glass protective cover containing an AM agent is separately fabricated and then adhered to the display glass module. This method is particularly popular for disposable coatings for example mobile or tablet protector films.

5.2.4 Physical structures

Physical structures are fabricated in top coat or directly into the glass. In contrast to approaches 1-3 which release active AM agents, this approach relies on surface nanostructures that are biocidal by combination of mechanisms including anti-adhesion properties that prevent bacterial attachment and nanometre sized structures that are capable of perforating bacterial cell membranes [219,220].

Table 3 Commercially available transparent AM coatings indicating fabrication method, coating properties.

Company Coating name	Coating AM agent	Fabrication	Properties	Comments	Ref.
NBD technologies InvisiPrint® MBED	Silane based thin film coating	Spray/dip/wipe	Oleophilic Hydrophobic ETC 93% transparent	ISO 22196 results Not EPA registered.	[221]
Kastus (Irish) Antimicrobial film	Cu / Ti based coating nanoparticle	Sintering T>600°C	>95% transparent	Market leader in screen protectors	[206]

NSG Purity	Photo-catalytically activated TiO_2	Sputtering T>600°C			
Corning (US) Antimicrobial Corning® Gorilla® glass	Ag ions ion infused into glass surface	Ion-exchange T>600°C	EPA registered	EPA registered	[222]
Pilkington (UK) SaniTise™	Pilkington SaniTise™ TiO_2 thin film	Pyrolytic hard coat T>600°C	90.5% transparent	Photocatalytic effect UV activated	[223]
3M™ Durable Protective Film 7760AM	Aftermarket PET adhesive film with an Ag ion containing hard-coat layer	Low T	Transparent	12-month shelf life due to humidity sensitivity EPA registered	[218]

Table 4 A comparison of the present study with previous works directed towards creating transparent Antimicrobial (AM) or antiviral (AV) coatings

Coating	Agent	Fabrication method	AM efficacy	AV efficacy	%T	Ref.
This work; SiO2 embedded Cu DNPs coatings on glass	Cu ions	Sputtering and dewetting	Up to 99.99%	Not reported	70-85	
PVA/ZnO PVA/Ag PVA/ZnO & Ag Disposable protective coatings	Ag/Zn ion	Spin coating a mixture PVA/$AgNO_3$ PVA/zinc acetate 80 °C		Not reported	75	[224]
PVF/AQCS/SiO_2 NP/Cu ions PVF/AQCS/SiO_2 NP/AQCS/Cu ions	ACQS / Cu ion supported on SiO2 NP	layer-by-layer (LbL)assembly of bactericidal polymers	99-100%			[213]
PDA/Cu PDA/Cu2O NP on glass	Cu ion/ Cu NP Supported on EDTA	Solution processes AQCS & EDTA covalently grafted to PVD for complexation with Cu ions	96% S. aureus 99.8% P. Aeruginosa		73-75	[208]
PDA/Cu2O	Cu ion	Spray coated (electroplateless deposition) <100°C	99.99% P. Aeruginosa	99.98 SARS-CoV-2	40-80	[209]
SiO_2 / Cu SiO_2 / Ag On borosilicate	Ag/Cu ion	<100°C	>99.99% P. Aeruginosa 99.18% S. aureus	99.98% SARS-CoV-2	71-75	[225]

Polymeric salts PSS-Bz-Ag and PSS-Bz bound to PSS		FA-CVD 150 °C	99.8% S. aureus		88-91	[211] [226]
Cu_2O-Zeolite/Polyurethane film	Cu ions	Polymeric salts 50 °C	SARS-CoV-2			[210]
(PVA)-based Cu NP–graphene coating	Cu NP/Cu ion	Flow coating on PET and PVC	99.99% E. coli 99.99% S. aureus	99.94% for SARS-CoV-2		[227]
Cu NP/ Ag NP on nanostructured PET/PE films	QAC	Dip coating on tempered glass	Not reported	Influenza A/H1N1/ WSN/1933 virus	>85	[228]
Conical nanopillars with Ag / Cu NPs	Ag / Cu NP/ions	Atomisation spray, thermal nanoimprint	Not reported	99.99% for SARS-CoV-2		[229]
Tetraethoxysilane (TEOS) and Q_4N^+-Si(OEt)$_3$	QAC	Sol-gel on glass	99.99% E. coli 99.99% S. aureus	Not reported	>85	[216]
Tertiary amine 2-(dimethylamino)ethyl methacrylate on glass	QAC	Atom transfer radical polymerization	99.99% E. coli 99.99% S. aureus	Not reported		[230]

5.2.1 Review of the antimicrobial properties of Copper and copper-based materials

Within the family of AM materials, Cu is registered as a self-sanitizer by the U.S. Environmental Protection Agency (EPA). Furthermore, in 2021 its' antiviral (AV) properties were also recognized after it was proven to inactivate 99.9% of SARS-CoV-2 virus particles within two hours [231]. As such, Cu-based materials have gained popularity in place of Ag-based and polymeric solutions owing to the comparably lower raw material cost and the wide spectrum of AM and AV activity against different species of microbes [108,111,208,212,232–234].

The AM activity of pure Cu/Cu-oxide surfaces is attributed to their ability to release free Cu ions (i.e. Cu^+ and Cu^{2+}) by aqueous corrosion processes [235,236]. The dominant process(es) taking place are determined by the prevailing environmental (e.g. relative humidity, temperature) and chemical conditions (e.g. air constituents, sweat contaminants). Once released, the Cu^+/Cu^{2+} species exert cytotoxic effects by participating in cyclic redox reactions at the cell surface [237]. For example, charged ions accumulate on the negatively charged domains of the bacterial membrane, altering its permeability and causing leakage of intracellular components [238]. In addition, ion channels within the membrane also permit the transport of ions into bacterial cells where they continue to release ions, which subsequently generate intracellular ROS including hydrogen peroxide (H_2O_2), superoxide ($O_2^{\bullet-}$), hydroxyl radical ($^{\bullet}OH$), and singlet oxygen [239]. These species induce oxidative stresses to intracellular components, denature proteins, alter the structure of DNA and de-regulate cellular metabolism [240–243]. A full review of the AM mechanisms of copper-containing surfaces can be found in references [212,244].

This Chapter describes a method of creating transparent AM nanostructured copper coatings (TANCs) on glass substrates. Nine criteria were set out; (1) the coated glass surface must have an AM function that is >99.9% effective against bacteria using the EPA dry test requirement, as described in Section 5.3.1. (2) the coating should be passive, i.e. not requiring additional activation from external sources (e.g. UV light); (3) the Cu release rate should be controlled such that the coating is permanently AM and yet still transparent; (4) the coating should impart the desired AM function without altering the original performance of the substrate; (5) the metallic colour of the Cu film or nanoparticles when deposited on the substrate should not impact the transparency of the original substrate, in particular, the nanostructures should be fabricated in such a way to minimise wavelength dependent light absorption and scattering; (6) The nanostructures must be durable and retain their AM property, after repeated and extended use. Generally, surfaces having nanostructures often lack durability due to the removal of the nanostructures by repeated use (e.g., friction), such as by wiping with a cleaning cloth, frequent contact with a pants pocket or purse during removal and insertion, touching with a human finger, and/or chemical interaction with the environment or cleaning solutions; (7) the coatings should be resistant to oxidation since the oxidation of Cu into CuO_x leads to a lessening of the AM effect; (8) electrically insulating function of touch-activated devices must be maintained; and (9) cover glass for displays is typically thin (<0.5mm in thickness). Herein, 0.3 mm thick ion-exchanged glass was used. This glass is typically used for touchscreen products. The processing temperature must be <400°C, as to avoid affecting the depth of layer or compressive stress characteristics of the glass or ion-exchanged glass.

The copper is obtained on the glass surface in the form of dewetted nanoparticles (DNPs) by an RTA process, described in Chapter 3, Section 3.3. The RTA of the Cu films is performed at low temperature (390°C), i.e. sufficiently close to the critical temperature at above which dewetting of the continuous film is observed and below the glass softening temperature (strain point) of the substrate, to intentionally introduce a degree of inhomogeneity into the contact angle, size and morphology of the particles obtained such that the plasmonic resonance effect on the colouring of the coating is kept within acceptable values. Additional dielectric layers of an inorganic oxide, for example SiO_2, are deposited on top to encapsulate the dewetted particles onto the surface and enhance their durability against the environment, external chemical agents and mechanical forces.

Based on the copper stability, and on the binding interactions between copper and the material of the dielectric layer, the copper release rate can be tuned. The durable transparent antimicrobial nanostructured coating, abbreviated to 'TANC' herein, is presented schematically in Figure 28. It comprises: a transparent substrate (1) upon which an optional titanium adhesion layer is first deposited, a second layer comprising of copper dewetted nanoparticles (Cu DNPs) (2) obtained through metal dewetting and with an average particle size and distribution to obtain high optical transmission, limited haze and colour, a third SiO_2 layer (3) to embed and encapsulate the Cu DNPs to the surface as well as protect the Cu from oxidation. This layer is within approximately 90% of the average particle height of the Cu DNPs. Finally, an anti-fingerprint (AF) Easy-to-Clean (ETC) coating is deposited on top of the embedded Cu DNPs, layer (4).

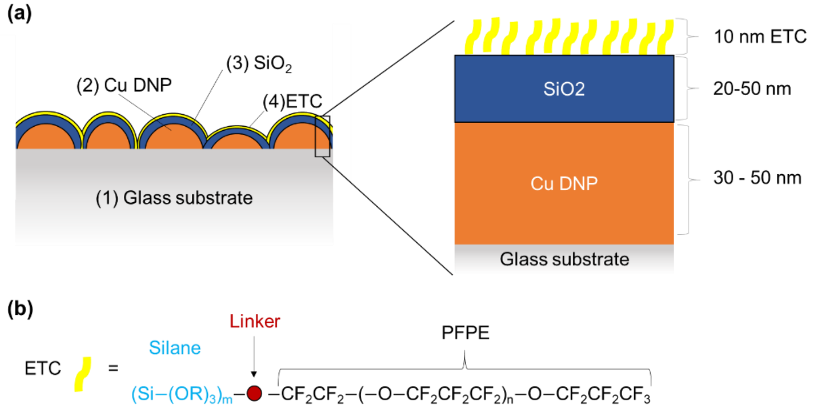

Figure 28 (a) Schematic illustration of the cross section of the TANC comprising 1 the glass substrate with optional adhesion layer, 2 copper or Cu_2O dewetted nanoparticles, 3 inorganic oxide embedding layer and 4 an easy to clean fluorosilane. The variation in contact angle the particle makes with the substrate is shown in the figure together with the related effects on thickness of covering layer. Dimensions are representative but not to scale. Zoomed area shows the cross section of the coating with representative dimensions. (b) General chemical formula of ETC Optool UD509, PFPE–silane monomer, which can have variable number of silane groups, m, and variable length of PFPE chain, n.

The ETC coatings have been adopted by the touch screen and display industries due to their oleophobic, hydrophobic, and excellent wear resistance properties. In this thesis, we selected an ETC from Daikin Chemicals (Optool UD509) due to its high contact angle with water (116°) and low coefficient of friction (COF) (~0.03) [245]. Optool UD509 belongs to the group of high molecular weight alkoxysilane functionalized perfluoropolyether (PFPE) compounds. The general structure, presented in Figure 28b, consists of three parts: i) the silane functional group, ii) the linker 'L' and iii) the PFPE chain. The silane group forms a strong covalent bond with the pre-deposited SiO_2 to create a uniform monolayer of thickness around 10 nm. Meanwhile the PFPE group gives the coating a low surface energy with hydrophobic self-cleaning properties. This property causes the oils and dirt from fingerprints to "bead up," making it "easy to clean" upon wiping with a dry cloth. The linker has length between 2 - 20nm, to ensure that there is a sufficient distance between the Si atom and the terminal fluorocarbon group, such that water/moisture from the ambient environment can contact the coating and transport Cu ions from the coating to the microbes at the surface.

Being hydrophobic the ETC may also act as a secondary barrier (or blocking layer), slowing the release of copper (since access of water with coating may be reduced) and further improving the durability to prolong the overall longevity of the surface of the AM coating.

5.3 Fabrication of TANCs

The deposition techniques used herein were previously described in Section 3.2.2. Ion-exchanged glass substrates from Corning Incorporated (glass code 2320) with a size of 2x2 inch and 0.3 mm thickness were sonicated in conventional organic solvents for 10 minutes and dried with an N_2 stream. A magnetron sputtering system (ATC Orion 8, AJA International, Inc.) was used for the metal depositions. A pre-deposition cleaning of the substrates was performed by exposing the substrates to an Ar plasma (bias power 40 W, pressure 8 mT, Ar flow 20 ssc/min) for 5 min. An ultrathin titanium (Ti) adhesion layer with a thickness of 2 nm onto the flat glass substrates was deposited from a target of 99.7% purity with a DC power of 100 W and a working pressure of 2 mTorr in an argon atmosphere (20 ssc/min). This was followed by an ultrathin Cu film with a thickness of 3.5 nm as shown in Figure 29a. The Cu film thickness was controlled by the sputtering time. The depositions were performed at a base pressure between about 10^{-7} and 10^{-8} Torr, room temperature, 100 W of Direct Current (DC) power, and 20 standard cubic centimetres per minute (scc/min) of pure argon (Ar). The working pressure was 1.5×10^{-3} Torr, the extrapolated deposition rate was 0.0454 nm/s for Ti and 0.142 nm/s for Cu, and the target−substrate distance was 35 cm with a rotation speed of 60 rpm. To obtain nanoparticles, the samples were subjected to a rapid thermal annealing (RTA) process as shown in Figure 29b. The RTA was carried out in the Tsunami TM RTP-600S system at the temperature of 390 °C, below the glass transition temperature of the substrate, for 600 s. High-purity N_2 gas (1 atm pressure) was used to prevent oxidation of the metal film. After RTA, 10-25 nm of SiO_2 was deposited conformally onto the Cu nanoparticles by using E-beam evaporation system (Lesker LAB 18 Thin Film Deposition System), as shown in Figure 29c. The deposition was performed at a base pressure of about 10^{-7} and 10^{-8} Torr, room temperature. The SiO_2 E-beam evaporation rate was set to 1 A/s as measured by a quartz microbalance. Thickness ranged from 0 - 50 nm to provide partial coverage of the nanoparticles whilst allowing optimisation of the durability and AM property of the coating. As a final step, the nanostructured surface was coated with a low surface energy coating, also known as an easy to clean (ETC) coating. Both continuous and patterned ETC coating methods were tested to obtain the best coating performance. Prior to the ETC application, the coated substrates were cleaned with an oxygen plasma of strength between 50-300 W for a time of 2 - 5 minutes. The ETC used was a fluorinated silane (Optool UD509) obtained from Daikin Chemicals. Optool UD509 was diluted to 0.005-0.024 % by weight in a fluorinated solvent (Novec HFE7200, 3M Company) to facilitate application to the surface while also helping to control density, thickness, and morphology of the coating. The ETC was deposited onto the substrate by spray-coating using an airbrush. The airbrush was held 2 inches away from the AM coating and sprayed for 20 seconds to give even coverage. The pressure of the airbrush was varied between 6 to 35 psi. Finally, the ETC was cured at 150°C, <10 min or in a desiccator at room temperature (RT) for 2 days. The curing step is required to adhere the silanes to the coating. The coating was then rinsed or sonicated in fluorinated solvent (NovecTM HFE7200 from 3M Company) for a time of 3-5 minutes to remove any un-reacted but physically adsorbed ETC. In this work, AM efficacy against *S. Aureus* was performed on two sets of TANCs (Set A and Set B), with varying SiO_2 thickness, fluorosilane concentration and oxidation conditions, according to Table 5.

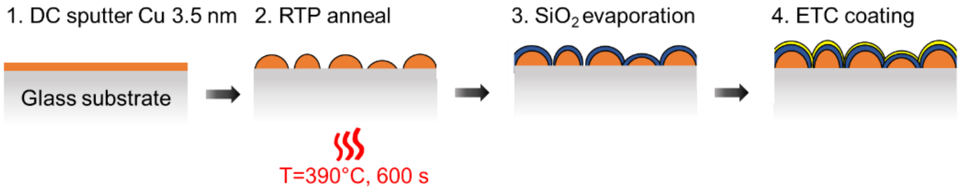

Figure 29) Fabrication of transparent and AM nanostructured Cu surface (TANCS) by (1) DC sputtering of 3.5 nm Cu onto a glass substrate, (2) Low temperature annealing of Cu to form dewetted nanoparticles, (3) Evaporation of an inorganic oxide, e.g. SiO_2, embedding layer and (4) spray coating of a polymer coating, e.g. fluorosilane based easy to clean (ETC). Note that the contact angle the particle makes with the substrate is not representative and varies between 60 -100° typically for low temperature de-wetting processes.

Table 5 TANCS coatings (A and B type) together with control (ctrl) samples.

Set	**Plasma (Duration / Time)**	**SiO_2 (nm)**	**Fluorosilane concentration %**
Ctrl: Uncoated glass	-	-	-
Ctrl: Stainless steel	-	-	-
Ctrl: Cu pure	-	-	-
A	50 W 2min	20 – 25 -30- 35 - 50	0
		20 – 25 -30- 35 - 50	0.012
		35 – 50	0.024
B	300 W 5 min	0 – 10 - 15	0
		15 – 25	0.005
		0 – 10 -15 - 25	0.012
		10 -15	0.024

5.3.1 Antimicrobial (AM) efficacy testing

Bactericidal efficacy testing on the TANCS coatings and stainless steel (SS), uncoated glass and Cu control samples was performed as described in the EPA test for efficacy of Cu alloy surfaces as a sanitizer [246]. Each coupon was tested in duplicate. Prior to AM testing all coupons were cleaned by immersion in a 75% ethanol solution followed by rinsing with deionized (DI) water. The coupons were then sterilized by exposure to UV light at 254 nm, for a duration of 15 minutes. For the preparation of the inoculum, a 20 µL aliquot of thawed bacterial Staphylococcus aureus AT 6538 (*S.Aureus*) culture was added to 10 mL Tryptic Soy Broth. The bacterial suspension was incubated at 36 °C for 48 h. The culture was subsequently centrifuged and allowed to settle. The supernatant was removed and pellet was resuspended in 6mL of phosphate buffer saline (PBS). The upper two thirds of the suspension were aspirated and the optical density at 600 nm (OD600) was measured to obtain the bacterial density estimation. The cell culture was diluted with PBS to achieve a bacterial inoculum concentration near the target value 1.0×10^6 colony-forming units (CFU) mL^{-1}. Organic soil load containing 250 µL fetal bovine serum (FBS) and 50 µL TritonX was added to 4700 µL of the inoculum to aid in spreading. Each coupon was inoculated with 20 µL of inoculum (Figure 30a). The inoculum volume was spread evenly over a central 1x1 inch test area of the coupon using bent sterile pipette tips. The 20 µL on the coupon typically dried within 5-15 min in ambient conditions. Once dry, the coupons were incubated in a controlled environment set at 42 % relative humidity (RH) and 23 °C for a period of 2 hours. Following the 2-hour exposure period, the coupons were neutralized in Letheen broth (GenLab). Ten-fold serial dilutions of the neutralized solutions were plated using standard spread plate technique on Tryptic Soy Agar plates and incubated for 48 h at 36 °C to yield countable numbers of survivors (approximately 20–200 colonies per plate). This range was selected because below 20 CFUs gives poor counting statistics and above 200 CFUs the bacteria grow too close together.

5.3.2 Calculations of log and percentage of reductions.

The calculation of the value of the AM activity is based on the $\log_{10}$ difference between the mean number of bacteria surviving on the TANCS and the mean number of bacteria surviving on the glass cover slip control samples [246]. Example calculations and all of the raw data are provided in Appendix A.

The experiments were performed in duplicate. First the geometric mean (GeoMean) of the number of organisms surviving on two control surfaces and two TANC surfaces was determined by Eq. 5.3.1:

$$\text{Geo Mean (CFU/mL)} = \left(\frac{\text{Sample1} + \text{Sample2}}{2}\right) \qquad (5.3.1)$$

where 'Sample X' represents the number of CFU/carrier on the TANC or control sample.

The log reduction (LR) was calculated by Eq. 5.3.2:

$$\text{LR} = -\ \text{Log}\left(\frac{\text{Geo Mean of TANC survivors}}{\text{Geo Mean of control survivors}}\right) \qquad (5.3.2)$$

The percentage (%) reduction of organisms surviving on the TANC surfaces over organisms surviving on parallel control surfaces was determined by Eq. 5.3.3:

$$\% \text{ reduction} = \left(\frac{\text{Geo mean of control survivors - Geo mean of TANC survivors}}{\text{Geo mean of control survivors}}\right) \cdot 100 \quad (5.3.3)$$

For the coatings to be approved as a ‘self-sanitising’, the AM test must demonstrate at least a 3-LR within the specified contact time. This corresponds to a 99.9% reduction in CFUs.

5.3.3 Stipulated wear testing

TANCS were subjected to a cleaning regimen suitable for electronic glass display covers based on EPA test method for the efficacy of copper surfaces as a sanitizer [246]. The cleaning regimen was designed to test the durability of the TANCS against abrasion from wiping with a cleaning cloth, frequent contact with a pants pocket or purse during removal and insertion, touching with a human finger, and/or chemical interaction with the environment or cleaning solutions. The abrasion procedures simulate regular touch and a worst-case scenario of 2× cleaning every day for up to 2 years. Simulated wear was performed using an Elcometer 5750 Taber® Linear Abrader, schematically shown in Figure 30b. For wet abrasion, the cleaning solution was prepared with isopropanol (IPA) and deionized (DI) water (70:30). A cloth was saturated with the cleaning solution and attached to the abrader head using double-sided adhesive tape. No additional accessory weights were added to the spline-shaft of the linear abrader (base load of 350 g) in order to keep the pressure similar to that applied by repeated touch or cloth wipes. This process was repeated for a certain number of cycles, such as 700 - 1200 cycles (1400-2400 passes of the wet or dry cloth), to simulate wear and cleaning for up to 2 years.

After completion of the wear cycles, the ‘worn’ surfaces were tested for bacterial efficacy against *S.Aureus* using the EPA testing procedure detailed in Section 5.3.1, as well as other optical and water contact angle properties. The “cloth” used in the durability tests is made of a standard material that is typically marketed and sold for use with electronic device touch screens (e.g., BIOPURETM 70% IPA wipes, or “Just Add Water” personal electronics cloths available from E-CLOTHTM), and thus does not readily impart scratches or damage to such a touchscreen surface. The “cloths” can also be the typical disinfecting wipes sold by LYSOL™ and CLOROX™, which are not typically marketed for touchscreen devices but can be used on them without readily imparting scratches or damage. Further information on typical setup conditions for the durability test are as follows: sample size 50 x 50 mm; weight 680 g; stroke length 18 mm; collet 1-inch diameter; speed 40 CPM. In a wet test, four wipes were stacked so as to maintained moisture due to capillary action; however, if wetness dissipated throughout a long (1200 cycle) test, then the used wipes were replaced with new wipes. If desired, for a single durability test that spans several days, the old wipes can be replaced with new wipes every day. It is not believed that the results are affected by using old or new wipes, provided that the moisture condition is maintained (e.g., dry conditions in a dry test and liquid conditions in a liquid test).

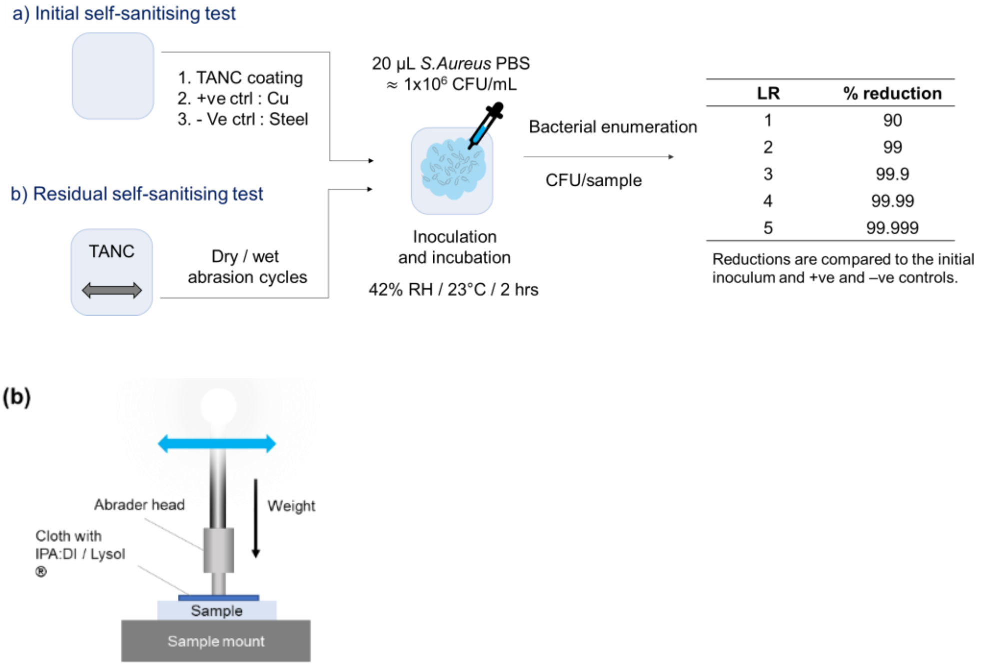

Figure 30 (a) Initial and residual self-sanitising test protocols defined by the EPA for the quantification of the AM efficacy of Cu-containing surfaces. (b) Stipulated wear testing setup for the residual self-sanitising test as described in 5.3.3.

5.3.4 ICP-MS mock testing to determine % of leached copper from TANCS

The number of Cu ions from the coating that equilibrate with those in the liquid inoculum in the AM test was estimated using a mock test that mimics the AM test – the mock test keeps all conditions the same as the AM test (Figure 30a) except the mock test has no bacterium in the inoculum. The control and test coupons are treated with the same cleaning and sterilization process as for the EPA AM test (Section 5.3.1). 20 µL aliquot of inoculum (without bacteria) was added to the central 1 cm^2 area of the TANCS. The leaching was performed in a controlled environment set at 42 % RH and 23 °C for a period of 2 hours. The leachate was collected from the coating by using 2x150µL of PBS in the exposed 1 inch^2 region, rinsing and removing the rinse solution into a tube. The amount of Cu in the leached solution was determined using ICP/MS detection. Positive and negative controls were run with pure Cu and stainless-steel coupons, respectively. The optical response of the coating after mock testing in the region 350-750 nm was also obtained.

5.3.5 Morphological, Optical, Mechanical and Antimicrobial Characterizations of the coatings.

The optical transmission spectra of the coatings in the wavelength range 380-750 nm were acquired using a spectrometer (Perkin Elmer LAMBDA 950). All of the reported transmission spectra represent the substrate and coating i.e., bare (uncoated) glass + Ti adhesion layer + dewetted Cu + SiO_2 + fluorosilane. Haze measurements were obtained using a BYK Haze-Guard iPro system. The wetting characteristic of the coated and uncoated substrates was determined by measuring the water contact angle (WCA) using a drop shape analysis system (DSA-100, Krüss GmbH). Five measurements at different points of each sample were taken, and the average and standard deviation reported. Scanning Electron Microscopy (SEM) images were obtained using a FEI-SEM, FEI Inspect F).

5.4 Results and discussion

5.4.1 Morphological, optical and electrical properties

As depicted schematically in Figure 31, the size and morphology of the Cu DNPs can be quite varied, due to the low temperature conditions of the dewetting process and thin precursor copper film. In Chapter 3, Section 3.3, a theoretical modelling of the low temperature dewetting together with a comparison of the simulated and experimental optical spectra provided insight into the advantage of low temperature dewetting for obtaining highly transmissive Cu DNP surfaces.

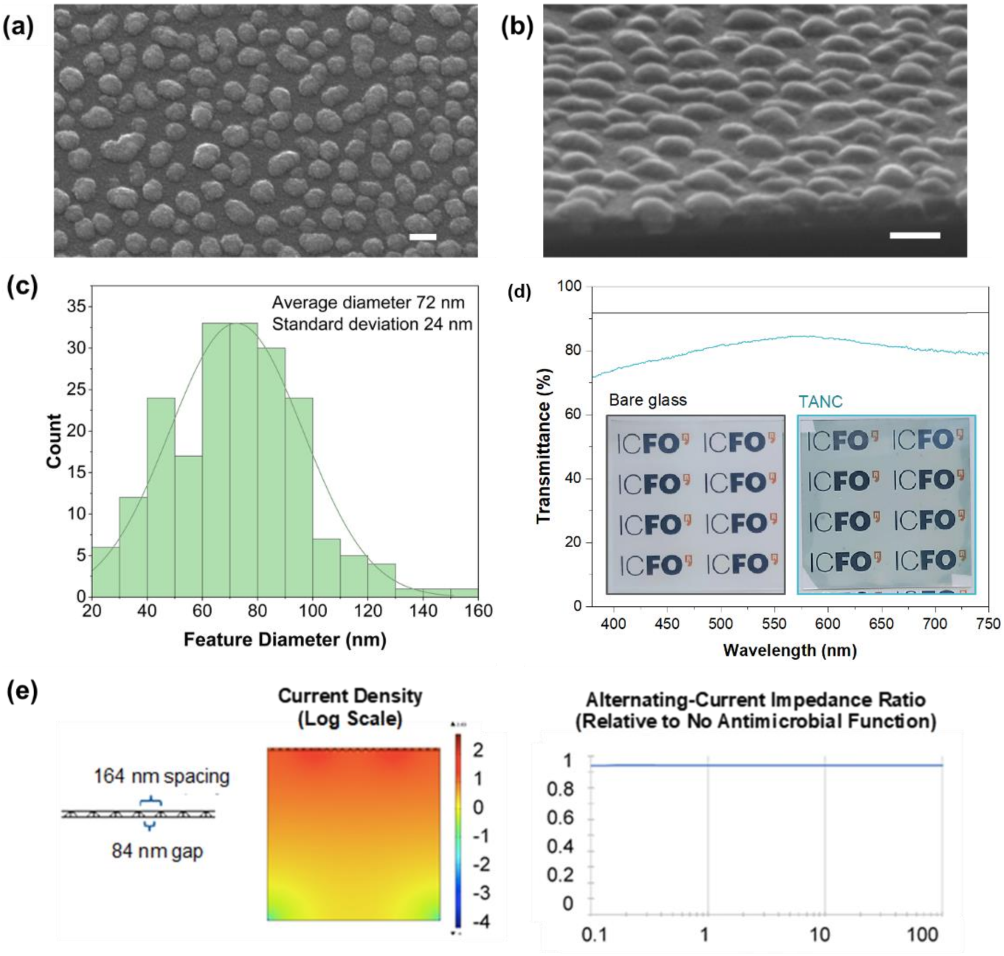

Figure 31 Top down (a) and side on (b) SEM micrographs of TANCS coatings. The parameters of the SEM scan are as follows. HV 15.00 kV; det ETD; magnification 160,000x; WD 9.9 mm; spot 3.0; tilt 0° (a). tilt -15°(b). The scale bar is 500 nm; (c) Particle size distribution analysis using ImageJ); (d) Transmission spectra of representative TANC (blue line) as compared to the uncoated bare glass substrate (black line). Inset shows photographs of bare glass (left) and TANCs (right); (e) Finite Element Model Prediction for TANCS obtained from 3.5 nm Cu UTMF. The graph shows the alternating-current impedance ratio of an TANC in accordance with one aspect relative to an otherwise identical bare glass substrate. The lateral-surface impedance predictions demonstrate that capacitive touch performance can coexist with this dewetting antimicrobial process.

The shape of the Cu DNPs (a and b) varies from flat hill to spherical-like. In some instances, particles are interconnected while others are separated up to around 60 nm. The average diameter and standard deviation is 72 nm ± 24. Likewise, the average particle height was 64 ± 20nm and average contact angle was 35° ± 12°. Note that in the case where the particle is non-spherical the diameter refers to the longest lateral edge to edge distance of the feature. The average of the longest lateral dimension is calculated using ImageJ [120] by measuring a representative number of Cu DNPs and averaging the result on a numbers basis. "Average height" was also calculated by measuring a representative number of Cu DNPs and averaging the result on a numbers basis.

The large dispersion of particle size and shape and interparticle distance induces a broadening and softening of the plasmonic resonance. The broadening of the resonance gives the coating a transparency without strong dependence on wavelength and the also leads to low scattering (haze) > 1%. Thus, the TANCS remain visually close to the neutral colour of the substrate and have a transmission between 70-80% that is almost independent of wavelength in the visible range. The inset photograph in Figure 31d demonstrates the visual appearance is such that the functionality of touchscreen devices would be retained

Furthermore, product modelling for capacitive touch devices was performed for the Cu DNPs using the Finite Element Model, Figure 31e. The results are for Finite Element Model Predictions for the dewetting case that result in Cu DNPs with a 164 nm spacing and 84 nm gap, based on the SEM analysis. The graph shows the alternating-current impedance ratio of a TANC in accordance with one aspect relative to an otherwise identical bare glass substrate. The predictions show that TANCs do not impact the frequency dependence of the surface-lateral electrical impedance in the 1MHz to 100MHz frequency range required by touch-enabled devices, indicating that the TANCs surfaces would retain touch screen functionality.

5.4.2 AM activity of TANCS

Mock and AM testing was performed on TANCs, whose conditions are presented in Table 5. Note that the mock tests are performed without bacteria for the reason that it is difficult to run safe measurements with microorganisms. Though we cannot conclude whether the presence of the microorganism would alter the rate of Cu dissolution, we assume that the main driver is the PBS solution and that any additional effect that the microorganism may have would not be significant by comparison. In other words, the rate of Cu dissolution due to the PBS >>> rate of consumption of Cu due to the presence of microorganisms. It is also important to acknowledge that the results presented herein should be interpreted with consideration of their processing conditions. Standardized test conditions were provided by the EPA, which is used by the majority of manufacturers for determining the antimicrobial activity of Cu-containing surfaces. The conditions of the test are very much more invasive with respect to the real-world environment, utilising a wet inoculum and elevated temperature and humidity, and as such, it does not guarantee efficacy *in situ* where conditions may differ. In fact, it is generally accepted that AM surfaces under wet conditions perform better due to accelerated rate of Cu dissolution [247–249]. It may also be that the salts contained within the buffer may complex with the 'free' Cu ions and reduce their bioavailability to the bacteria thereby suppressing the toxic effects of metal excess [250]. Future work should also consider 'dry testing´ approaches to better emulate the real working conditions [251].

A practical requirement for touchscreen application is the ability to continually release Cu in optimal concentrations over a long period of time without compromising the overall transparency, durability, and functionality of the coating. Figure 32 plots the data of LR from AM test against the data of Cu leaching from the mock test. The LR correlates positively with the amount of Cu leached into the solution up to ~4 mg/L after which increased Cu dissolution does not significantly increase the LR. By this, the minimum inhibitory concentration of Cu (MIC-Cu) needed in solution to reach the EPA requirement of 3-LR, equivalent to 99.9% kill, was determined to be ∼2 mg/L. The bacterial killing mechanism could be explained by diffusion of mobile Cu ions through the SiO_2 and fluorosilane capping layers to the coating's surface where they interact with and kill the suspended/floating microbes. The diffusion of Cu ions is mediated by a liquid vehicle - e.g. cleaning solvents, surface moisture or the PBS solution hosting the bacteria. Based on a MIC-Cu of ∼2mg/L and, assuming a uniform distribution of microorganisms in the fluid, the number of ions, *n*, available to each microorganism is estimated to be on the order of 10^{11}. This is orders of magnitude over the natural intracellular concentration of Cu atoms/ions in *S. Aureus*, which is reported to be in the region of 10^4 to10^5 [252]. Therefore, it is reasonable to assume that TANCS impose their AM activity by releasing Cu in sufficient concentrations for these specific bacteria.

For assessment of the optical properties, the transmission of the coatings in the visible region was measured before and after mock testing. Figure 32b shows the optical spectra and photographs corresponding to TANCS leaching <2 mg/L Cu (squares) and >4 mg/L Cu (circles). Both cases show an increase in transmission after mock testing in the region of the plasmonic resonance associated with the Cu DNPs. This can be explained by reduced plasmonic coupling, as Cu dissolves into solution, the DNPs decrease in dimensions, reducing the interactions that give rise to plasmonic coupling.

The distinction between Set A and B lies in the strength and duration of oxygen plasma cleaning treatment prior to the fluorosilane application. Set A TANCs were treated with 50W for 2 minutes whilst Set B were treated with 300 W for 5 minutes (Table 5). The inset photographs in (b) show prototypical examples of TANCS from both sets after mock testing where the marked central region denotes the mock testing area. A distinction in the color of the central region after mock testing is observed where Set B maintains a color close to the original coating whilst Set A has a more evident color loss. The release of Cu species into the PBS droplet, is influenced by the Cu solubility within the coating. It is likely that the different oxygen plasma treatment supports the difference in the leaching data between Set A and B TANCs.

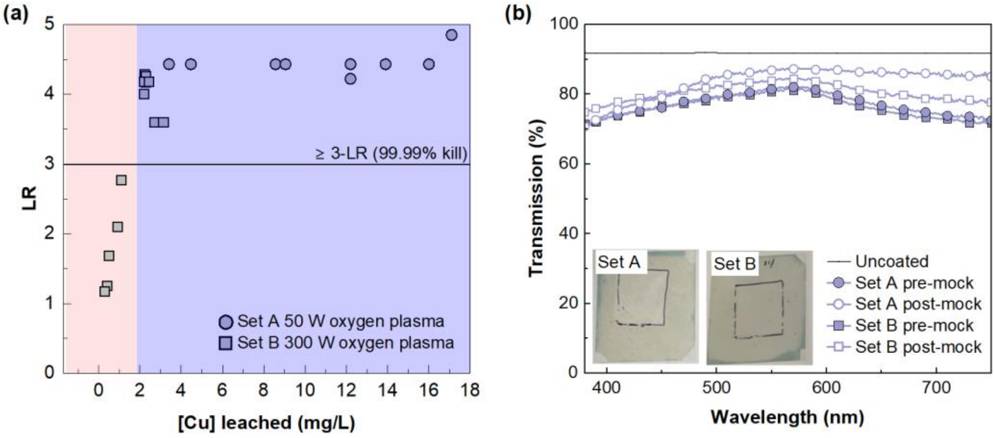

Figure 32 (a) LR vs [Cu] leached. The EPA-prescribed 3-LR, corresponding to >99.99% reduction in bacterial colony counts, is marked with a black line. The blue and pink shaded regions correspond to the [Cu] concentration range above and below which a 3-LR was observed, respectively. *The comparison between LR and [Cu] leached assumes that the majority of the ions are held in the liquid phase and not consumed by the microorganisms i.e. rate of Cu dissolution due to the PBS >>> rate of consumption of Cu due to the presence of microorganisms. (b) Transmission spectra of representative TANCS. For both graphs, the circle and square markers represent TANCS from sets A and B, respectively. Inset of (b) shows photographs of Set A and Set B after mock testing where the marked central region shows the testing area.

It is evident from the plot in Figure 32a that some of the TANCS in Table 5 leach Cu excessively above the MIC-Cu determined to be ~2mg/L. From a coating longevity point of view, excessive Cu leaching is undesirable. In cases where [Cu] leached >> MIC-Cu, we propose that the Cu is being released in a burst like manner. The migration of chloride ions into the TANC facilitates the fast generation of Cu ions such that the effect of the SiO_2 thickness is masked. To combat this and increase the longevity of the TANCs, we increased both the fluorosilane concentration and the SiO_2 thickness in order to control the rate of Cu dissolution.

The results are presented in Figure 33 which plots the LR from the AM test and [Cu] leached during the mock test *vs.* SiO_2 thickness and fluorosilane concentration for TANCS treated with (a) 50 W and (b) 300 W oxygen plasma. First, we observe that Set A TANCS leached up to 4 times more Cu than Set B for the same SiO_2 thickness and flurosilane concentration. The lower Cu dissolution rate in Set B is likely due to a higher (300 W) oxygen plasma treatment that may have partially oxidized the underlying Cu, thereby reducing its solubility. Second, we note that all TANCS from Set A demonstrated a >4-LR in the AM test irrespective of SiO_2 thickness, except with the 0.024 % fluorosilane coated TANCS, where the LR and [Cu] leached scaled with SiO_2 thickness concentration. The same trend was observed in Set B TANCS, though, the effect of SiO_2 thickness was also observed for the lower (0.012%) fluorosilane concentration. It is likely that for TANCS with high concentration fluorosilane high oxygen plasma treatment (Set B), the migration of chloride into the TANCS is reduced and the burst release mechanism is suppressed. In such a way, a method of controlling the Cu dissolution to within the optimal range above MIC-Cu is demonstrated. Overall, a combination of SiO_2 thickness, fluorosilane concentration and oxidation of the underlying Cu is required to achieve the optimal Cu release and LR.

(a) Set A: 50 W O_2 plasma

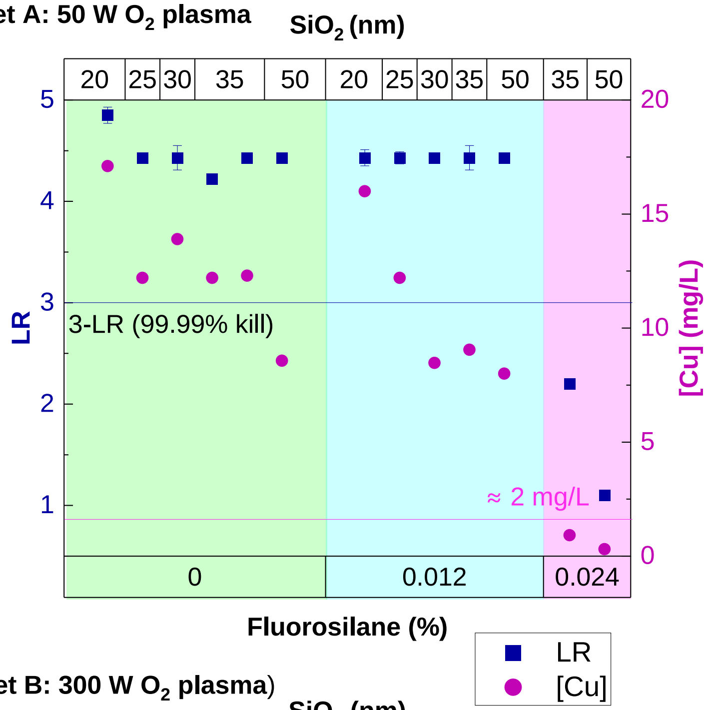

(b) Set B: 300 W O_2 plasma)

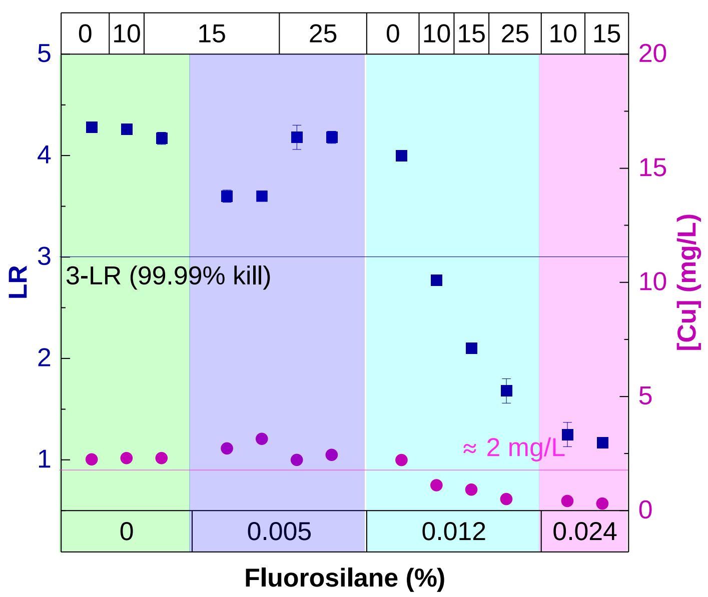

Figure 33 Plots of LR and [Cu] leached as a function of SiO_2 thickness and fluorosilane concentration for (a) 50 W and (b) 300 W oxygen plasma treated TANCS. Error bars represent the standard deviation of two samples. Note that in some cases, the error bar is smaller than the marker and not visible

Finally, WCA of the coatings before and after AM testing. The ETC coating imparts a contact angle >90° and changes by less than 5% after the AM test. Table 6 shows that for the selected embodiments of Set A, after AM testing, the change in water contact angle of the antimicrobial article surface varies by less than 5% from the initial contact angle value of the coating measured before testing. For other samples, the variation is as low as 3% or less than 1%. The results of the AM testing illustrate good performance of the AM surface in terms of retaining a high-water contact angle.

Table 6 Water contact angle (WCA) of Set A TANCS before and after AM testing.

Sample ID	**SiO_2 (nm)**	**Conditions**	**Mean WCA before EPA test (°)**	**SDev. (°)**	**Mean WCA after EPA test (°)**	**SDev. (°)**
Ctrl Glass coverslip	-	-				
Ctrl Steel	-	-				
Cu metal	-	-				
1-A	20	As rcd	59	3.2	56	7.4
2-A	25	As rcd	61	1.3	58	1.6
3-A	30	As rcd	49	4.8	51	3.2
4-A	35	As rcd	37	3.6	30	6.5
5-A	50	As rcd	42	2.1	40	2.4
6-A	20	0.012 % ETC	110	1.9	98	2.9
7-A	25	0.012 % ETC	107	4.3	97	1.5
8-A	30	0.012 % ETC	101	5.7	95	1.9
9-A	35	0.012 % ETC	107	4.3	102	1.6
10-A	50	0.012 % ETC	108	2.7	99	1.8
11-A	35	0.024 % ETC	118	0.4	119	0.1
12-A	50	0.024 % ETC	120	0.8	116	1.0

"WCA" is contact angle; "SDev." is standard deviation. The contact angle was measured at five locations and averaged.

5.5 AM durability

Touchscreens are continuously exposed to various types of contact and wear. Therefore, durability and resistance to general wear and tear is an important reliability feature for AM coatings. Durability against wiping and cleaning as prescribed by European Centre for Disease Prevention and Control (ECDC) guidelines for infection control, was tested by subjecting the TANCS to the equivalent of up to 2 years of wear (see methods Section 5.3.3) and then testing their AM, optical and wetting properties. Identical TANCs (each with 25 nm SiO_2 and 0.012% fluorosilane) were fabricated. The first sample was immediately AM tested, and the second sample was AM tested after 730 or 1200 abrasion cycles with a Lysol® or IPA impregnated scouring pad on the coating surface, respectively. The results are presented in Figure 34. All TANCs demonstrated a > 3-LR against *S. Aureus* even after abrasion testing. The TANCs also maintained their wetting and optical characteristics post-abrasion, revealing a less than 5% average gain in transmission and between 10-15% reduction in contact angle with respect to the initial value. The maintenance of the high WCA, demonstrates that the fluorosilane is a robust topcoat that does not degrade with repeated wiping. Overall, the results of the abrasion testing suggest that the embedded Cu DNPs are reasonably durable in terms of retaining AM activity, optical properties and high-WCA (>90).

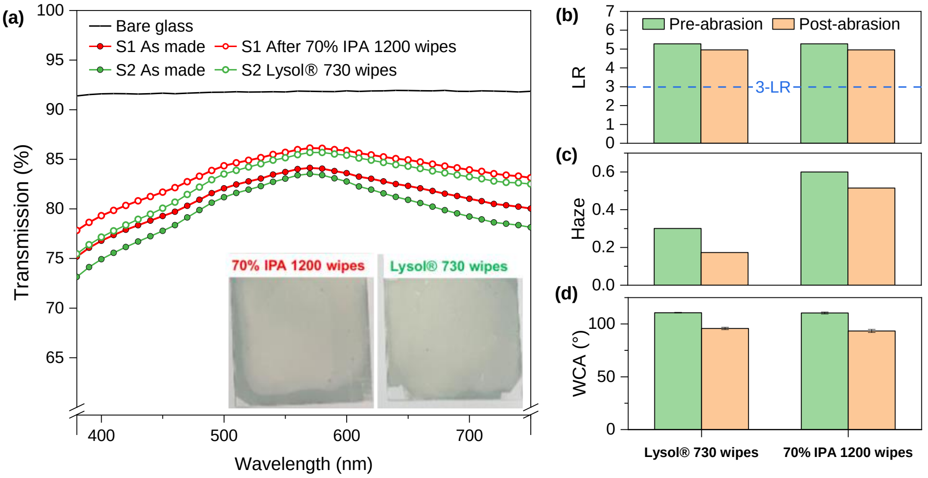

Figure 34 (a) Transmission, (b) LR, (c) Haze and (d) WCA of TANCS before and after wet abrasion testing with IPA (1200 wipes) and Lysol® (730 wipes). The inset of (a) shows the TANCS after wet abrasion testing on the central region. The visual appearance of the central wiping region remains close in color to the outer region, indicting a good durability of the coating to repeated wipes with cleaning sanitizers.

5.6 Conclusion

This work incorporates Cu DNPs into a transparent and AM nanostructured Cu surface (TANCS) for glass substrates. The TANCS demonstrated a > 99.9% effectiveness against *S. Aureus,* and have a colour-neutral optical transparency between 70-80% in the region 380-750 nm. Moreover, the TANCs are easy to clean and retain their AM efficacy, optical and wetting properties even after durability testing. In addition, they are fabricated in a way that is industrially scalable. The proposed AM TANCS may be useful in applications of technological interest such as multi-user transparent touch activated surfaces.

Chapter 6

Conclusions & Outlook

6.1 Conclusions

Ultrathin materials and nano-structures are key elements in developing multifunctional transparent surfaces. Combining optically transparent substrates with ultrathin materials with advanced functionalities, such as antimicrobial or electrically conducting could have a significant impact in multiple applications, including display screens, transparent solar cells and transparent antimicrobial coatings. This thesis has been focused on the development of low temperature growth and processing of ultrathin and nanostructured materials to create transparent multifunctional surfaces for optoelectronic and biological applications through easy to implement, scalable methods. The main achievements of this thesis are summarised by its objectives:

Objective 1: Develop scalable techniques to transfer 2D materials, such as graphene, MoS_2 and nanostructured metals onto transparent flexible substrates at low temperatures

- Chapter 3 demonstrated a simple and fast technique to obtain high thermal processing materials and nano-structures on low strain-point flexible substrates. The method utilises water-soluble polished salt substrates, a well-known material that can stand the high temperatures involved during the growth, and can provide a fast and clean transfer onto the flexible target substrate due to the easy dissolution of the salt in water. Moreover, employing salt as a sacrificial substrate avoids the detrimental effects of harsh-etchant based transfer processes.

- The use of NaCl salt substrates for the material growth and transfer was verified, for the first time, with two prototypical materials, dewetted gold nano-particles and MoS_2. The method demonstrated preservation of coverage and structural quality of both materials after transfer to PET substrates. The proposed method offers universal applicability for various 2D materials and nanostructures, supporting polymers, and final substrates, thus facilitating the easy fabrication of flexible 2D material-based electronics and optoelectronics.

Objective 2: *Find the optimum substrate-graphene combination for increasing doping and the electrical conductivity of transparent surfaces.*

- The development of a method of obtaining a highly transparent conductive surface of graphene on an ion-exchanged glass was demonstrated in Chapter 4. Specifically, an n-doping in the order of -10^{13} to -10^{14} cm^{-2} was obtained. Such high n-doping levels in graphene originating from the interaction with the substrate underneath have never been observed before.

Objective 3: Use ultrathin metals and subsequent nanostructuring for increasing the antimicrobial activity of transparent surfaces

- The development and optimisation of novel, Cu-nanoparticle-based antimicrobial coatings on glass that are transparent, durable and retain their antimicrobial efficacy, optical, electrical, and wetting properties after regular and repeated use over a long period of time, whilst also being fabricated in a way that is industrially scalable, was demonstrated in Chapter 5. Furthermore, unlike traditional high temperature sintering and ion-exchange techniques, the AM coatings presented in this thesis are fabricated using low temperature techniques compatible with a wider range of technologically relevant substrates, for example, cover glass for display modules. Thus, the approach demonstrates the potential to address one of the largest sources of fomite-driven nosocomial infections, namely displays and other surfaces requiring transparency and electrical/ capacitance activity.

6.2 Outlook

The methods developed in this thesis represent a significant stepping stone towards the implementation of nanostructured and ultrathin materials on low thermal budget transparent substrates for applications such as transparent conductors and antimicrobial coatings for glass. Nevertheless, further developments will be necessary to achieve practical implementation.

The demonstrated proof-of-concept growth and transfer technique using NaCl (Chapter 3) could easily be extended to other 2D materials, heterostructures and nanostructures, as well as alternative water-soluble crystalline growth substrates, such as ZnO for a wide range of applications, including advanced electronic and optoelectronic devices.

As for the graphene/IOX systems, whilst a substantial increase in the graphene surface potential (-1.61 eV) and about a factor of 10 decrease in sheet resistance was demonstrated (Chapter 4), the sheet resistance gradually increased by about 40% after exposure to ambient conditions. This doping instability is considered as one of the biggest challenges to realizing the practical applications of transparent graphene electrodes. With this in mind, it would be promising to pursue methods of improving the doping stability over time, with, for example, the use of alternative encapsulation techniques. Secondly, whilst it is clear that the IOX glass is a key element to achieve doping, additional experiments with other modified glasses would be needed to confirm the doping mechanism and the interplay between the processing steps to make the devices.

With these developments, the graphene/IOX system demonstrates potential to realize a host of previously inaccessible applications including low cost, compact photonic devices operating in the NIR/VIS wavelength range and low work function transparent electrodes for energy conversion and electron emission applications such as OLED, LEDS, solar cell, and touchscreen applications. One area to explore could be subsequent nanostructuring into, for example, nanodisk or nanoribbon geometries, for making plasmonic sensing devices operating in the near-infrared region.

Finally, this thesis demonstrated a novel method to achieve durable transparent antimicrobial surfaces. One challenge when using Cu-based nanostructures as high-touch surfaces is the oxidation, corrosion and aging of the surface. Since the oxidation of copper(0) or copper(I) oxide into copper(II) oxide has a lessening effect on the antimicrobial action of a surface, strategies that minimise the oxidation of Cu should be explored. One line of investigation, for example, could involve dewetting UTMFs of a Cu-Zn alloy. Another inquiry, aimed at facilitating practical applications, could be a systematic exploration of the antimicrobial functionality of TANCs during indoor atmospheric exposure conditions, including factors such as deposited sweat and cyclic wet/dry air conditions.

Broader questions remain over the antimicrobial mechanism(s) of metallic species, especially for such instances as those in Chapter 5, where the mechanism likely involves a complex interplay between the surface feature shape, size and geometry as well the inherent antimicrobial nature of both Cu and Cu oxides. In this regard, studies further examining the survival of bacteria as a function of measured surface oxidation and wettability would prove vital in understanding the role of the bacteria/surface interaction.

BIBLIOGRAPHY

[1] Novoselov K S, Geim A K, Morozov S v, Jiang D, Zhang Y, Dubonos S v, Grigorieva I v and Firsov A A 2004 Electric Field Effect in Atomically Thin Carbon Films *Science (1979)* **306** 666–9

[2] Novoselov K S, Geim A K, Morozov S v., Jiang D, Katsnelson M I, Grigorieva I v., Dubonos S v. and Firsov A A 2005 Two-dimensional gas of massless Dirac fermions in graphene *Nature* **438** 197–200

[3] Zhang Y, Tan Y W, Stormer H L and Kim P 2005 Experimental observation of the quantum Hall effect and Berry's phase in graphene *Nature* **438** 201–4

[4] Du X, Skachko I, Duerr F, Luican A and Andrei E Y 2009 Fractional quantum Hall effect and insulating phase of Dirac electrons in graphene *Nature* **462** 192–5

[5] Novoselov K, Jiang Z, Zhang Y, Morozov S, Stormer H, Zeitler U, Maan J, Boebinger G, Kim P and Geim A 2007 Room-Temperature Quantum Hall Effect in Graphene *Rep. Prog. Phys* **64** 201

[6] Geim A K and Novoselov K S 2007 The rise of graphene *Nat Mater* **6** 183–91

[7] Novoselov K S Graphene: Materials in the flatland. Nobel Lecture (2010)

[8] Geim A K Random walk to graphene. Nobel Lecture (2010).

[9] Castro Neto A H, Guinea F, Peres N M R, Novoselov K S and Geim A K 2009 The electronic properties of graphene *Rev Mod Phys* **81** 109–62

[10] das Sarma S, Adam S, Hwang E H and Rossi E 2011 Electronic transport in two-dimensional graphene *Rev Mod Phys* **83** 407–70

[11] Lee S K, Kim B J, Jang H, Yoon S C, Lee C, Hong B H, Rogers J A, Cho J H and Ahn J H 2011 Stretchable graphene transistors with printed dielectrics and gate electrodes *Nano Lett* **11** 4642–6

[12] Lemme M, Member S, Echtermeyer T, Baus M, Kurz H, Lemme M C, Echtermeyer T J, Baus M and Kurz H 2007 *A Graphene Field Effect Device* vol 28

[13] Banszerus L, Schmitz M, Engels S, Dauber J, Oellers M, Haupt F, Watanabe K, Taniguchi T, Beschoten B and Stampfer C 2015 Ultrahigh-mobility graphene devices from chemical vapor deposition on reusable copper *Sci Adv* **1** 1–7

[14] Blake P, Hill E W, Castro Neto A H, Novoselov K S, Jiang D, Yang R, Booth T J and Geim A K 2007 Making graphene visible *Appl Phys Lett* **91**

[15] Nair R R, Blake P, Grigorenko A N, Novoselov K S, Booth T J, Stauber T, Peres N M R and Geim A K 2008 Fine structure constant defines visual transparency of graphene *Science (1979)* **320** 1308–9

[16] Low T and Avouris P 2014 Graphene plasmonics for terahertz to mid-infrared applications *ACS Nano* **8** 1086–101

[17] Mak K F, Sfeir M Y, Wu Y, Lui C H, Misewich J A and Heinz T F 2008 Measurement of the opptical conductivity of graphene *Phys Rev Lett* **101**

[18] Li Z Q, Henriksen E A, Jiang Z, Hao Z, Martin M C, Kim P, Stormer H L and Basov D N 2008 Dirac charge dynamics in graphene by infrared spectroscopy *Nat Phys* **4** 532–5

[19] Kuzmenko A B, van Heumen E, Carbone F and van der Marel D 2008 Universal optical conductance of graphite *Phys Rev Lett* **100**

[20] Mak K F, Lee C, Hone J, Shan J and Heinz T F 2010 Atomically Thin MoS 2 : A New Direct-Gap Semiconductor *Phys Rev Lett* **105** 136805

[21] Wang Q H, Kalantar-Zadeh K, Kis A, Coleman J N and Strano M S 2012 Electronics and optoelectronics of two-dimensional transition metal dichalcogenides *Nat Nanotechnol* **7** 699–712

[22] Bertolazzi S, Brivio J and Kis A 2011 Stretching and Breaking of Ultrathin MoS $_2$ *ACS Nano* **5** 9703–9

[23] Salvatore G A, Münzenrieder N, Barraud C, Petti L, Zysset C, Büthe L, Ensslin K and Tröster G 2013 Fabrication and Transfer of Flexible Few-Layers MoS $_2$ Thin Film Transistors to Any Arbitrary Substrate *ACS Nano* **7** 8809–15

[24] Li X and Zhu H 2015 Two-dimensional MoS2: Properties, preparation, and applications *Journal of Materiomics* **1** 33–44

[25] Radisavljevic B, Radenovic A, Brivio J, Giacometti V and Kis A 2011 Single-layer MoS2 transistors *Nat Nanotechnol* **6** 147–50

[26] Pu J, Yomogida Y, Liu K-K, Li L-J, Iwasa Y and Takenobu T 2012 Highly Flexible MoS $_2$ Thin-Film Transistors with Ion Gel Dielectrics *Nano Lett* **12** 4013–7

[27] Borah C K, Tyagi P K and Kumar S 2020 The prospective application of a graphene/MoS2heterostructure in Si-HIT solar cells for higher efficiency *Nanoscale Adv* **2** 3231–43

[28] Wu S, Zeng Z, He Q, Wang Z, Wang S J, Du Y, Yin Z, Sun X, Chen W and Zhang H 2012 Electrochemically Reduced Single-Layer MoS2 Nanosheets: Characterization, Properties, and Sensing Applications *Small* **8** 2264–70

[29] Kang Z, Ma Y, Tan X, Zhu M, Zheng Z, Liu N, Li L, Zou Z, Jiang X, Zhai T and Gao Y 2017 MXene–Silicon Van Der Waals Heterostructures for High-Speed Self-Driven Photodetectors *Adv Electron Mater* **3**

[30] Chen Y, Wang Y, Wang Z, Gu Y, Ye Y, Chai X, Ye J, Chen Y, Xie R, Zhou Y, Hu Z, Li Q, Zhang L, Wang F, Wang P, Miao J, Wang J, Chen X, Lu W, Zhou P and Hu W 2021 Unipolar barrier photodetectors based on van der Waals heterostructures *Nat Electron* **4** 357–63

[31] Yu F, Hu M, Kang F and Lv R 2018 Flexible photodetector based on large-area few-layer MoS2 *Progress in Natural Science: Materials International* **28** 563–8

[32] Chang H-Y, Yang S, Lee J, Tao L, Hwang W-S, Jena D, Lu N and Akinwande D 2013 High-Performance, Highly Bendable MoS $_2$ Transistors with High-K Dielectrics for Flexible Low-Power Systems *ACS Nano* **7** 5446–52

[33] Bernardi M, Palummo M and Grossman J C 2013 Extraordinary sunlight absorption and one nanometer thick photovoltaics using two-dimensional monolayer materials *Nano Lett* **13** 3664–70

[34] Splendiani A, Sun L, Zhang Y, Li T, Kim J, Chim C Y, Galli G and Wang F 2010 Emerging photoluminescence in monolayer MoS2 *Nano Lett* **10** 1271–5

[35] Watanabe K, Taniguchi T and Kanda H 2004 Direct-bandgap properties and evidence for ultraviolet lasing of hexagonal boron nitride single crystal *Nat Mater* **3** 404–9

[36] Dean C R, Young A F, Meric I, Lee C, Wang L, Sorgenfrei S, Watanabe K, Taniguchi T, Kim P, Shepard K L and Hone J 2010 Boron nitride substrates for high-quality graphene electronics *Nat Nanotechnol* **5** 722–6

[37] Jang A R, Hong S, Hyun C, Yoon S I, Kim G, Jeong H Y, Shin T J, Park S O, Wong K, Kwak S K, Park N, Yu K, Choi E, Mishchenko A, Withers F, Novoselov K S, Lim H and Shin H S 2016 Wafer-Scale and Wrinkle-Free Epitaxial Growth of Single-Orientated Multilayer Hexagonal Boron Nitride on Sapphire *Nano Lett* **16** 3360–6

[38] Golberg D, Bando Y, Huang Y, Terao T, Mitome M, Tang C and Zhi C 2010 Boron nitride nanotubes and nanosheets *ACS Nano* **4** 2979–93

[39] Lee C, Li Q, Kalb W, Liu X-Z, Berger H, Carpick R W and Hone J *Frictional Characteristics of Atomically Thin Sheets*

[40] Li L H, Cervenka J, Watanabe K, Taniguchi T and Chen Y 2014 Strong oxidation resistance of atomically thin boron nitride nanosheets *ACS Nano* **8** 1457–62

[41] Ahn S, Kim G, Nayak P K, Yoon S I, Lim H, Shin H J and Shin H S 2016 Prevention of Transition Metal Dichalcogenide Photodegradation by Encapsulation with h-BN Layers *ACS Nano* **10** 8973–9

[42] Liu Z, Gong Y, Zhou W, Ma L, Yu J, Idrobo J C, Jung J, Macdonald A H, Vajtai R, Lou J and Ajayan P M 2013 Ultrathin higherature oxidation-resistant coatings of hexagonal boron nitride *Nat Commun* **4**

[43] Geim A K and Grigorieva I v 2013 Van der Waals heterostructures *Nature* **499**

[44] Novoselov K S, Mishchenko A, Carvalho A and Castro Neto A H 2016 2D materials and van der Waals heterostructures *Science (1979)* **353**

[45] Maniyara R A, Rodrigo D, Yu R, Canet-Ferrer J, Ghosh D S, Yongsunthon R, Baker D E, Rezikyan A, García de Abajo F J and Pruneri V 2019 Tunable plasmons in ultrathin metal films *Nat Photonics*

[46] Kang H, Jung S, Jeong S, Kim G and Lee K 2015 ARTICLE Polymer-metal hybrid transparent electrodes for flexible electronics *Nat Commun* **6**

[47] Yu R, Mazumder P, Borrelli N F, Carrilero A, Ghosh D S, Maniyara R A, Baker D, García De Abajo F J and Pruneri V 2016 Structural Coloring of Glass Using Dewetted Nanoparticles and Ultrathin Films of Metals *ACS Photonics* **3**

[48] Ji C, Liu D, Zhang C and Jay Guo L 2020 Ultrathin-metal-film-based transparent electrodes with relative transmittance surpassing 100% *Nat Commun* **11**

[49] Maniyara R A, Mkhitaryan V K, Chen T L, Ghosh D S and Pruneri V 2016 An antireflection transparent conductor with ultralow optical loss (<2 %) and electrical resistance (<6Ωsq-1) *Nat Commun* **7**

[50] Zhao G, Shen W, Jeong E, Lee S G, Yu S M, Bae T S, Lee G H, Han S Z, Tang J, Choi E A and Yun J 2018 Ultrathin Silver Film Electrodes with Ultralow Optical and Electrical Losses for Flexible Organic Photovoltaics *ACS Appl Mater Interfaces* **10** 27510–20

[51] Akin Sonmez N, Donmez M, Comert B and Ozcelik S 2018 Ag/M-seed/AZO/glass structures for low-E glass: Effects of metal seeds *Int J Appl Glass Sci* **9** 383–91

[52] Luhmann N, Høj D, Piller M, Kähler H, Chien M H, West R G, Andersen U L and Schmid S 2020 Ultrathin 2 nm gold as impedance-matched absorber for infrared light *Nat Commun* **11**

[53] Shah D, Kudyshev Z A, Saha S, Shalaev V M and Boltasseva A 2020 Transdimensional material platforms for tunable metasurface design *MRS Bull* **45** 188–95

[54] Mejía-Salazar J R and Oliveira O N 2018 Plasmonic Biosensing *Chem Rev* **118** 10617–25

[55] Bauer E 1958 Phenomenological theory of crystal deposition on surfaces *Zeitschrift fur Kristallographie, Materials* **110** 372–94

[56] Schubert S, Meiss J, Müller-Meskamp L and Leo K 2013 Improvement of transparent metal top electrodes for organic solar cells by introducing a high surface energy seed layer *Adv Energy Mater* **3** 438–43

[57] Martínez-Cercós D, Paulillo B, Maniyara R A, Rezikyan A, Bhattacharyya I, Mazumder P and Pruneri V 2021 Ultrathin Metals on a Transparent Seed and Application to Infrared Reflectors *ACS Appl Mater Interfaces* **13** 46990–7

[58] Kamiko M, Kim S M, Jeong Y S, Ha J H, Koo S M and Ha J G 2018 Influences of ultra-thin Ti seed layers on the dewetting

phenomenon of Au films deposited on Si oxide substrates *Physica E Low Dimens Syst Nanostruct* **99** 320–9

[59] Kamiko M, Suenaga R, Koo J W, Nose K, Kyuno K and Ha J G 2013 Epitaxial growth of fcc-Ag(0 0 1) nanodots on MgO(0 0 1) substrates via Ti seed layer-assisted agglomeration *J Phys D Appl Phys* **46**

[60] Todeschini M, Bastos Da Silva Fanta A, Jensen F, Wagner J B and Han A 2017 Influence of Ti and Cr Adhesion Layers on Ultrathin Au Films *ACS Appl Mater Interfaces* **9** 37374–85

[61] Leroy F, Borowik, Cheynis F, Almadori Y, Curiotto S, Trautmann M, Barbé J C and Müller P 2016 How to control solid state dewetting: A short review *Surf Sci Rep* **71** 391–409

[62] Thompson C v 2012 Solid-State Dewetting of Thin Films *Annu Rev Mater Res* **42** 399–434

[63] Kittel C 2005 *Introduction to Solid State Physics Charles* (Wiley: Hoboken,NJ, 2005.)

[64] Ashcroft N W and Mermin N D 1978 *Solid State Physics* vol 9 (Holt,Rinehart & Winston: New York, 1976)

[65] Wang H, Tam F, Grady N K and Halas N J 2005 Cu nanoshells: Effects of interband transitions on the nanoparticle plasmon resonance *Journal of Physical Chemistry B* **109** 18218–22

[66] Li H, Zhang Q, Yap C C R, Tay B K, Edwin T H T, Olivier A and Baillargeat D 2012 From bulk to monolayer MoS2: Evolution of Raman scattering *Adv Funct Mater* **22** 1385–90

[67] Molina-Sánchez A, Hummer K and Wirtz L 2015 Vibrational and optical properties of MoS2: From monolayer to bulk *Surf Sci Rep* **70** 554–86

[68] McCreary K M, Hanbicki A T, Sivaram S v. and Jonker B T 2018 A- and B-exciton photoluminescence intensity ratio as a measure of sample quality for transition metal dichalcogenide monolayers *APL Mater* **6**

[69] Schroder D K 2015 *Semiconductor Material and Device Characterization, 3rd Edition*

[70] Bahk J-H, Favaloro T and Shakouri A 2013 *Thin Film Thermoelectric Characterization* vol 16 (Begell House)

[71] Sze S M and Ng K K 2006 *Physics of Semiconductor Devices. 3rd Edition, John Wiley and Sons, Hoboken.*

[72] Rombaut J, Maniyara R A, Bellman R A, Acquard D F, Baca A S, Osmond J, Senaratne W, Quesada M A, Baker D, Mazumder P and Pruneri V 2018 Antireflective Transparent Oleophobic Surfaces by Noninteracting Cavities *ACS Appl Mater Interfaces* **10** 43230–5

[73] Rombaut J, Martínez S, Matera U M, Mazumder P and Pruneri V 2021 Antireflective Multilayer Surface with Self-Cleaning Subwavelength Structures *ACS Photonics* **8** 894–900

[74] Arrés Chillón J, Paulillo B, Mazumder P and Pruneri V 2022 Transparent Glass Surfaces with Silica Nanopillars for Radiative Cooling *ACS Appl Nano Mater* **5** 17606–12

[75] Tulli D, Hart S D, Mazumder P, Carrilero A, Tian L, Koch K W, Yongsunthon R, Piech G A and Pruneri V 2014 Monolithically Integrated Micro- and Nanostructured Glass Surface with Antiglare, Antireflection, and Superhydrophobic Properties *ACS Appl Mater Interfaces* **6** 11198–203

[76] Hong C-H, Shin J-H, Ju B-K, Kim K-H, Park N-M, Kim B-S and Cheong W-S 2013 Index-Matched Indium Tin Oxide Electrodes for Capacitive Touch Screen Panel Applications *J Nanosci Nanotechnol* **13** 7756–9

[77] Granqvist C G 2007 Transparent conductors as solar energy materials: A panoramic review *Solar Energy Materials and Solar Cells* **91** 1529–98

[78] Kang J, Kim H, Kim K S, Lee S K, Bae S, Ahn J H, Kim Y J, Choi J B and Hong B H 2011 High-performance graphene-based transparent flexible heaters *Nano Lett* **11** 5154–8

[79] Granqvist C G and Hultaker˚ A H 2002 *Transparent and conducting ITO films: new developments and applications* vol 411

[80] Scott J C, Kaufman J H, Brock P J, DiPietro R, Salem J and Goitia J A 1996 Degradation and failure of MEH-PPV light-emitting diodes *J Appl Phys* **79** 2745–51

[81] Ghosh D S, Martinez L, Giurgola S, Vergani P and Pruneri V 2009 Widely transparent electrodes based on ultrathin metals *Opt Lett* **34** 325

[82] Wang C K, Chang S J, Su Y K, Chang C S, Chiou Y Z, Kuo C H, Lin T K, Ko T K and Tang J J 2004 GaN MSM photodetectors with TiW transparent electrodes *Mater Sci Eng B Solid State Mater Adv Technol* **112** 25–9

[83] Ghosh D S, Chen T L and Pruneri V 2010 High figure-of-merit ultrathin metal transparent electrodes incorporating a conductive grid *Appl Phys Lett* **96** 041109

[84] De S, Higgins T M, Lyons P E, Doherty E M, Nirmalraj P N, Blau W J, Boland J J and Coleman J N 2009 Silver nanowire networks as flexible, transparent, conducting films: Extremely high DC to optical conductivity ratios *ACS Nano* **3** 1767–74

[85] Lee J Y, Connor S T, Cui Y and Peumans P 2008 Solution-processed metal nanowire mesh transparent electrodes *Nano Lett* **8** 689–92

[86] Na S I, Kim S S, Jo J and Kim D Y 2008 Efficient and flexible ITO-free organic solar cells using highly conductive polymer anodes *Advanced Materials* **20** 4061–7

[87] Chang Y M, Wang L and Su W F 2008 Polymer solar cells with poly(3,4-ethylenedioxythiophene) as transparent anode *Org Electron* **9** 968–73

[88] Ouyang J, Xu Q, Chu C W, Yang Y, Li G and Shinar J 2004 On the mechanism of conductivity enhancement in poly(3,4-ethylenedioxythiophene):poly(styrene sulfonate) film through solvent treatment *Polymer (Guildf)* **45** 8443–50

[89] Barnes T M, Bergeson J D, Tenent R C, Larsen B A, Teeter G, Jones K M, Blackburn J L and van de Lagemaat J 2010 Carbon nanotube network electrodes enabling efficient organic solar cells without a hole transport layer *Appl Phys Lett* **96**

[90] Rowell M W, Topinka M A, McGehee M D, Prall H J, Dennler G, Sariciftci N S, Hu L and Gruner G 2006 Organic solar cells with carbon nanotube network electrodes *Appl Phys Lett* **88**

[91] Wu Z, Chen Z, Du X, Logan J M, Sippel J, Nikolou M, Kamaras K, Reynolds J R, Tanner D B, Hebard A F and Rinzler A G 2000 *Transparent, Conductive Carbon Nanotube Films* vol 289 (Academic Press)

[92] Bae S H, Lee Y, Sharma B K, Lee H J, Kim J H and Ahn J H 2013 Graphene-based transparent strain sensor *Carbon N Y* **51** 236–42

[93] Di C A, Wei D, Yu G, Liu Y, Guo Y and Zhu D 2008 Patterned graphene as source/drain electrodes for bottom-contact organic field-effect transistors *Advanced Materials* **20** 3289–93

[94] Liu W, Jackson B L, Zhu J, Miao C-Q, Chung C-H, Park Y-J, Sun K, Woo J and Xie Y-H 2010 Large scale pattern graphene electrode for high performance in transparent organic single crystal field-effect transistors *ACS Nano* **4** 3927—3932

[95] Choe M, Lee B H, Jo G, Park J, Park W, Lee S, Hong W K, Seong M J, Kahng Y H, Lee K and Lee T 2010 Efficient bulk-heterojunction photovoltaic cells with transparent multi-layer graphene electrodes *Org Electron* **11** 1864–9

[96] Jo G, Choe M, Cho C Y, Kim J H, Park W, Lee S, Hong W K, Kim T W, Park S J, Hong B H, Kahng Y H and Lee T 2010 Large-scale patterned multi-layer graphene films as transparent conducting electrodes for GaN light-emitting diodes *Nanotechnology* **21**

[97] Blake P, Brimicombe P D, Nair R R, Booth T J, Jiang D, Schedin F, Ponomarenko L A, Morozov S v, Gleeson H F, Hill E W, Geim A K and Novoselov K S *Graphene-Based Liquid Crystal Device*

[98] Choi H J, Jung S M, Seo J M, Chang D W, Dai L and Baek J B 2012 Graphene for energy conversion and storage in fuel cells and supercapacitors *Nano Energy* **1** 534–51

[99] Rowell M W and McGehee M D 2011 Transparent electrode requirements for thin film solar cell modules *Energy Environ Sci* **4** 131–4

[100] Bae S, Kim H, Lee Y, Xu X, Park J S, Zheng Y, Balakrishnan J, Lei T, Ri Kim H, Song Y il, Kim Y J, Kim K S, Özyilmaz B, Ahn J H, Hong B H and Iijima S 2010 Roll-to-roll production of 30-inch graphene films for transparent electrodes *Nat Nanotechnol* **5** 574–8

[101] Wang Y, Tong S W, Xu X F, Özyilmaz B and Loh K P 2011 Interface engineering of layer-by-layer stacked graphene anodes for high-performance organic solar cells *Advanced Materials* **23** 1514–8

[102] Kasry A, Kuroda M A, Martyna G J, Tulevski G S and Bol A A 2010 Chemical doping of large-area stacked graphene films for use as transparent, conducting electrodes *ACS Nano* **4** 3839–44

[103] Kim K K, Reina A, Shi Y, Park H, Li L J, Lee Y H and Kong J 2010 Enhancing the conductivity of transparent graphene films via doping *Nanotechnology* **21**

[104] Khrapach I, Withers F, Bointon T H, Polyushkin D K, Barnes W L, Russo S and Craciun M F 2012 Novel highly conductive and transparent graphene-based conductors *Advanced Materials* **24** 2844–9

[105] Wang X, Zhi L and Müllen K 2008 Transparent, conductive graphene electrodes for dye-sensitized solar cells *Nano Lett* **8** 323–7

[106] Shim J P, Choe M, Jeon S R, Seo D, Lee T and Lee D S 2011 InGaN-based p-i-n solar cells with graphene electrodes *Applied Physics Express* **4**

[107] Imani S M, Ladouceur L, Marshall T, Maclachlan R, Soleymani L and Didar T F 2020 Antimicrobial nanomaterials and coatings: Current

mechanisms and future perspectives to control the spread of viruses including SARS-CoV-2 *ACS Nano* **14** 12341–69

[108] Vincent M, Hartemann P and Engels-Deutsch M 2016 Antimicrobial applications of copper *Int J Hyg Environ Health* **219** 585–91

[109] Grass G, Rensing C and Solioz M 2011 Metallic copper as an antimicrobial surface *Appl Environ Microbiol* **77** 1541–7

[110] Salah I, Parkin I P and Allan E 2021 Copper as an antimicrobial agent: Recent advances *RSC Adv* **11** 18179–86

[111] Vincent M, Duval R E, Hartemann P and Engels-Deutsch M 2018 Contact killing and antimicrobial properties of copper *J Appl Microbiol* **124** 1032–46

[112] Yang P, Zou X, Zhang Z, Hong M, Shi J, Chen S, Shu J, Zhao L, Jiang S, Zhou X, Huan Y, Xie C, Gao P, Chen Q, Zhang Q, Liu Z and Zhang Y 2018 Batch production of 6-inch uniform monolayer molybdenum disulfide catalyzed by sodium in glass *Nat Commun* **9**

[113] Ling X, Lee Y H, Lin Y, Fang W, Yu L, Dresselhaus M S and Kong J 2014 Role of the seeding promoter in MoS2 growth by chemical vapor deposition *Nano Lett* **14** 464–72

[114] Suleman M, Lee S, Kim M, Nguyen V H, Riaz M, Nasir N, Kumar S, Park H M, Jung J and Seo Y 2022 NaCl-Assisted Temperature-Dependent Controllable Growth of Large-Area MoS2Crystals Using Confined-Space CVD *ACS Omega* **7** 30074–86

[115] Graham C, Frances M M M, Maniyara R A, Wen Y, Mazumder P and Pruneri V 2020 NaCl substrates for high temperature processing and transfer of ultrathin materials *Sci Rep* **10**, 7253

[116] Yan M, Dai J and Qiu M 2014 Lithography-free broadband visible light absorber based on a mono-layer of gold nanoparticles *Journal of Optics (United Kingdom)* **16**

[117] Mazumder P, Jiang Y, Baker D, Carrilero A, Tulli D, Infante D, Hunt A T and Pruneri V 2014 Superomniphobic, Transparent, and

Antireflection Surfaces Based on Hierarchical Nanostructures *Nano Lett* **14** 4681

[118] Tesler A B, Maoz B M, Feldman Y, Vaskevich A and Rubinstein I 2013 Solid-state thermal dewetting of just-percolated gold films evaporated on glass: Development of the morphology and optical properties *Journal of Physical Chemistry C* **117** 11337–46

[119] v. 6.1. www.comsol.com. COMSOL AB S S COMSOL Multiphysics® software

[120] Schindelin J, Arganda-Carreras I, Frise E, Kaynig V, Longair M, Pietzsch T, Preibisch S, Rueden C, Saalfeld S, Schmid B, Tinevez J-Y, White D J, Hartenstein V, Eliceiri K, Tomancak P and Cardona A 2012 Fiji: an open-source platform for biological-image analysis *Nat Methods* **9** 676–82

[121] McPeak K M, Jayanti S v., Kress S J P, Meyer S, Iotti S, Rossinelli A and Norris D J 2015 Plasmonic films can easily be better: Rules and recipes *ACS Photonics* **2** 326–33

[122] B Johnson P P and Christy R W 1974 Optical constants of transition metals *Phys. Rev. B* **9** 5056–70

[123] Paris A, Vaccari A, Lesina A C, Serra E and Calliari L 2012 Plasmonic Scattering by Metal Nanoparticles for Solar Cells *Plasmonics* **7** 525–34

[124] Günendi M C, Tanyeli İ, Akgüç G B, Bek A, Turan R and Gülseren O 2013 Understanding the plasmonic properties of dewetting formed Ag nanoparticles for large area solar cell applications *Opt Express* **21** 18344

[125] Schranghamer T F, Sharma M, Singh R and Das S 2021 Review and comparison of layer transfer methods for two-dimensional materials for emerging applications *Chem Soc Rev* **50** 11032–54

[126] Lin Z, Zhao Y, Zhou C, Zhong R, Wang X, Tsang Y H and Chai Y 2016 Controllable Growth of Large–Size Crystalline MoS2 and Resist-Free Transfer Assisted with a Cu Thin Film *Sci Rep* **5** 18596

[127] Wang X, Feng H, Wu Y and Jiao L 2013 Controlled synthesis of highly crystalline MoS2 flakes by chemical vapor deposition *J Am Chem Soc* **135** 5304–7

[128] Lee Y-H, Zhang X-Q, Zhang W, Chang M-T, Lin C-T, Chang K-D, Yu Y-C, Wang J T-W, Chang C-S, Li L-J and Lin T-W 2012 Synthesis of Large-Area MoS $_2$ Atomic Layers with Chemical Vapor Deposition *Advanced Materials* **24** 2320–5

[129] van der Zande A M, Huang P Y, Chenet D A, Berkelbach T C, You Y, Lee G H, Heinz T F, Reichman D R, Muller D A and Hone J C 2013 Grains and grain boundaries in highly crystalline monolayer molybdenum disulphide *Nat Mater* **12** 554–61

[130] Najmaei S, Liu Z, Zhou W, Zou X, Shi G, Lei S, Yakobson B I, Idrobo J-C, Ajayan P M and Lou J *Vapor Phase Growth and Grain Boundary Structure of Molybdenum Disulfide Atomic Layers*

[131] Castellanos-Gomez A, Buscema M, Molenaar R, Singh V, Janssen L, van der Zant H S J and Steele G A *Deterministic transfer of two-dimensional materials by all-dry viscoelastic stamping*

[132] Liu Y, Huang Y and Duan X 2019 Van der Waals integration before and beyond two-dimensional materials *Nature* **567** 323–33

[133] Wang M, Li H, Ko T J, Shawkat M S, Okogbue E, Yoo C, Han S S, Islam M A, Oh K H and Jung Y 2020 Manufacturing strategies for wafer-scale two-dimensional transition metal dichalcogenide heterolayers *J Mater Res* **35** 1350–68

[134] Lin Z, Zhao Y, Zhou C, Zhong R, Wang X, Tsang Y H and Chai Y 2015 Controllable Growth of Large-Size Crystalline MoS2 and Resist-Free Transfer Assisted with a Cu Thin Film *Sci Rep* **5**

[135] Xu Z Q, Zhang Y, Lin S, Zheng C, Zhong Y L, Xia X, Li Z, Sophia P J, Fuhrer M S, Cheng Y B and Bao Q 2015 Synthesis and Transfer of Large-Area Monolayer WS2 Crystals: Moving Toward the Recyclable Use of Sapphire Substrates *ACS Nano* **9** 6178–87

[136] Zhang F, Erb C, Runkle L, Zhang X and Alem N 2017 Etchant-free transfer of 2D nanostructures *Nanotechnology* **29** 25602

[137] Gurarslan A, Yu Y, Su L, Yu Y, Suarez F, Yao S, Zhu Y, Ozturk M, Zhang Y and Cao L 2014 Surface-energy-assisted perfect transfer of centimeter-scale monolayer and few-layer MoS2 films onto arbitrary substrates *ACS Nano* **8** 11522–8

[138] Lee C H, McCulloch W, Lee E W, Ma L, Krishnamoorthy S, Hwang J, Wu Y and Rajan S 2015 Transferred large area single crystal MoS2 field effect transistors *Appl Phys Lett* **107**

[139] Lee Y H, Yu L, Wang H, Fang W, Ling X, Shi Y, Lin C te, Huang J K, Chang M T, Chang C S, Dresselhaus M, Palacios T, Li L J and Kong J 2013 Synthesis and transfer of single-layer transition metal disulfides on diverse surfaces *Nano Lett* **13** 1852–7

[140] Lai S, Jeon J, Song Y J and Lee S 2016 Water-penetration-assisted mechanical transfer of large-scale molybdenum disulfide onto arbitrary substrates *RSC Adv* **6** 57497–501

[141] Dong W J, Kim S, Park J Y, Yu H K and Lee J L 2019 Ultrafast and Chemically Stable Transfer of Au Nanomembrane Using a Water-Soluble NaCl Sacrificial Layer for Flexible Solar Cells *ACS Appl Mater Interfaces* **11** 30477–83

[142] Ram S K, Desta D, Rizzoli R, Bellettato M, Lyckegaard F, Jensen P B, Jeppesen B R, Chevallier J, Summonte C, Larsen A N and Balling P 2017 Combining light-harvesting with detachability in high-efficiency thin-film silicon solar cells *Nanoscale* **9** 7169–78

[143] Lee D K, Kim T S, Choi J Y and Yu H K 2018 Recrystallized NaCl from Thin Film to Nano-/Microsized Sacrificial Crystal for Metal Nanostructures *Cryst Growth Des* **18** 5295–300

[144] Cho H Y, Nguyen T K, Ullah F, Yun J W, Nguyen C K and Kim Y S 2018 Salt-assisted clean transfer of continuous monolayer MoS2 film for hydrogen evolution reaction *Physica B Condens Matter* **532** 84–9

[145] Sharma M, Singh A, Aggarwal P and Singh R 2022 Large-Area Transfer of 2D TMDCs Assisted by a Water-Soluble Layer for Potential Device Applications *ACS Omega* **7** 11731–41

[146] Singh A, Moun M, Sharma M, Barman A, Kapoor A K and Singh R *NaCl-Assisted Substrate Dependent 2D Planar Nucleated Growth of MoS2*

[147] Bunton G v. and Day S C M 1972 Epitaxial thin films of ZnS and GaAs prepared by R.F. sputtering on NaCl substrates *Thin Solid Films*

[148] Henley S J, Ashfold M N R and Cherns D 2002 The oriented growth of ZnO films on NaCl substrates by pulsed laser ablation *Thin Solid Films* **422** 69–72

[149] Wang L L, Wang X, Zheng W T, Ma N, Guan Q F, Zhao J, Chen Y and Feng S H 2006 Synthesis of single nanocrystal phase γ′-Fe4N on NaCl substrate by DC magnetron sputtering *Mater Chem Phys* **100** 304–7

[150] Matthews J W 1966 Growth of Face-Centered-Cubic Metals on Sodium Chloride Substrates *Journal of Vacuum Science and Technology* **3** 133–45

[151] Yamada Y, Kasukabe Y and Yoshida K 1990 Cubic crystals in Ti Films evaporated on NaCl substrates *Jpn J Appl Phys* **29** 706–9

[152] Linder V, Gates B D, Ryan D, Parviz B A and Whitesides G M 2005 Water-soluble sacrificial layers for surface micromachining *Small* **1** 730–6

[153] Shi L, Chen K, Du R, Bachmatiuk A, Rümmeli M H, Priydarshi M K, Zhang Y, Manivannan A and Liu Z 2015 Direct Synthesis of Few-Layer Graphene on NaCl Crystals *Small* **11** 6302–8

[154] Wang S, Rong Y, Fan Y, Pacios M, Bhaskaran H, He K and Warner J H 2014 Shape Evolution of Monolayer MoS 2 Crystals Grown by Chemical Vapor Deposition *Chemistry of Materials* **26** 6371–9

[155] Govind Rajan A, Warner J H, Blankschtein D and Strano M S 2016 Generalized Mechanistic Model for the Chemical Vapor Deposition of 2D Transition Metal Dichalcogenide Monolayers *ACS Nano* **10** 4330–44

[156] Wu S, Zeng X, Wang W, Zeng Y, Hu Y, Yin S, Lu J and Zhou G 2018 The morphological control of MoS2 films using a simple model under chemical vapor deposition *Thin Solid Films* **666** 150–5

[157] Wang X, Sun G, Routh P, Kim D H, Huang W and Chen P 2014 Heteroatom-doped graphene materials: Syntheses, properties and applications *Chem Soc Rev* **43** 7067–98

[158] Panchakarla L S, Subrahmanyam K S, Saha S K, Govindaraj A, Krishnamurthy H R, Waghmare U v. and Rao C N R 2009 Synthesis, structure, and properties of boron- and nitrogen-doped graphene *Advanced Materials* **21** 4726–30

[159] Lee H, Paeng K and Kim I S 2018 A review of doping modulation in graphene *Synth Met* **244** 36–47

[160] Banhart F, Kotakoski J and Krasheninnikov A v. 2011 Structural defects in graphene *ACS Nano* **5** 26–41

[161] Liu H, Liu Y and Zhu D 2011 Chemical doping of graphene *J Mater Chem* **21** 3335–45

[162] D'Arsié L, Esconjauregui S, Weatherup R S, Wu X, Arter W E, Sugime H, Cepek C and Robertson J 2016 Stable, efficient p-type doping of graphene by nitric acid *RSC Adv* **6** 113185–92

[163] Wehling T O, Novoselov K S, Morozov S v., Vdovin E E, Katsnelson M I, Geim A K and Lichtenstein A I 2008 Molecular doping of graphene *Nano Lett* **8** 173–7

[164] Park H, Rowehl J A, Kim K K, Bulovic V and Kong J 2010 Doped graphene electrodes for organic solar cells *Nanotechnology* **21**

[165] Guo B, Fang L, Zhang B and Gong J R 2011 Graphene Doping: A Review *Insciences Journal* 80–9

[166] Sonde S, Giannazzo F, Raineri V and Rimini E 2009 Dielectric thickness dependence of capacitive behavior in graphene deposited on silicon dioxide *Journal of Vacuum Science & Technology B: Microelectronics and Nanometer Structures Processing, Measurement, and Phenomena* **27** 868–73

[167] Schwierz F 2010 Graphene transistors *Nat Nanotechnol* **5** 487–96

[168] Meric I, Dean C, Young A, Hone J, Kim P and Shepard K L 2010 Graphene field-effect transistors based on boron nitride gate dielectrics *Technical Digest - International Electron Devices Meeting, IEDM*

[169] Kim B J, Jang H, Lee S K, Hong B H, Ahn J H and Cho J H 2010 High-performance flexible graphene field effect transistors with ion gel gate dielectrics *Nano Lett* **10** 3464–6

[170] Pirkle A, Chan J, Venugopal A, Hinojos D, Magnuson C W, McDonnell S, Colombo L, Vogel E M, Ruoff R S and Wallace R M 2011 The effect of chemical residues on the physical and electrical properties of chemical vapor deposited graphene transferred to SiO2 *Appl Phys Lett* **99**

[171] Ryu S, Liu L, Berciaud S, Yu Y J, Liu H, Kim P, Flynn G W and Brus L E 2010 Atmospheric oxygen binding and hole doping in deformed graphene on a SiO2 substrate *Nano Lett* **10** 4944–51

[172] Cheng Z, Zhou Q, Wang C, Li Q, Wang C and Fang Y 2011 Toward intrinsic graphene surfaces: A systematic study on thermal annealing and wet-chemical treatment of SiO2-supported graphene devices *Nano Lett* **11** 767–71

[173] Hwang J O, Park J S, Choi D S, Kim J Y, Lee S H, Lee K E, Kim Y H, Song M H, Yoo S and Kim S O 2012 Workfunction-tunable, N-doped reduced graphene transparent electrodes for high-performance polymer light-emitting diodes *ACS Nano* **6** 159–67

[174] Matyba P, Yamaguchi H, Eda G, Chhowalla M, Edman L and Robinson N D 2010 Graphene and mobile ions: The key to all-plastic,

solution-processed light-emitting devices *ACS Nano* vol 4 pp 637–42

[175] Chang J H, Lin W H, Wang P C, Taur J I, Ku T A, Chen W T, Yan S J and Wu C I 2015 Solution-processed transparent blue organic light-emitting diodes with graphene as the top cathode *Sci Rep* **5**

[176] Wittmann S, Aumer F, Wittmann D, Pindl S, Wagner S, Gahoi A, Reato E, Belete M, Kataria S and Lemme M C 2020 Dielectric Surface Charge Engineering for Electrostatic Doping of Graphene *ACS Appl Electron Mater* **2** 1235–42

[177] Park H Y, Yoon J S, Jeon J, Kim J, Jo S H, Yu H Y, Lee S and Park J H 2015 Controllable and air-stable graphene n-type doping on phosphosilicate glass for intrinsic graphene *Org Electron* **22** 117–21

[178] Dissanayake D M N M, Ashraf A, Dwyer D, Kisslinger K, Zhang L, Pang Y, Efstathiadis H and Eisaman M D 2016 Spontaneous and strong multi-layer graphene n-doping on soda-lime glass and its application in graphene-semiconductor junctions *Sci Rep* **6**

[179] Suk J W, Kitt A, Magnuson C W, Hao Y, Ahmed S, An J, Swan A K, Goldberg B B and Ruoff R S 2011 Transfer of CVD-Grown Monolayer Graphene onto Arbitrary Substrates *ACS Nano* **5** 6916–24

[180] Li X, Cai W, An J, Kim S, Nah J, Dongxing Y, Richard Piner, Velamankanni A, Jung I, Tutuc E, Banerjee Sanjay K, Columbo L and Ruoff R S 2009 Large-Area Synthesis of High-Quality and Uniform Graphene Films on Copper Foils *Science (1979)* **324** 1312–4

[181] Novoselov K S, Fal'Ko V I, Colombo L, Gellert P R, Schwab M G and Kim K 2012 A roadmap for graphene *Nature* **490** 192–200

[182] Yuan H, Chang S, Bargatin I, Wang N C, Riley D C, Wang H, Schwede J W, Provine J, Pop E, Shen Z X, Pianetta P A, Melosh N A and Howe R T 2015 Engineering Ultra-Low Work Function of Graphene *Nano Lett* **15** 6475–80

[183] Dorgan V E, Bae M H and Pop E 2010 Mobility and saturation velocity in graphene on SiO2 *Appl Phys Lett* **97**

[184] Chen J H, Jang C, Xiao S, Ishigami M and Fuhrer M S 2008 Intrinsic and extrinsic performance limits of graphene devices on SiO 2 *Nat Nanotechnol* **3** 206–9

[185] Wang L, Meric I, Huang P Y, Gao Q, Gao Y, Tran H, Taniguchi T, Watanabe K, Campos L M, Muller D A, Guo.J, Kim P, Hone.J, Shepard K L and Dean C R 2013 One-Dimensional Electrical Contact toa Two-Dimensional Material *Science (1979)* **342** 614–7

[186] Purdie D G, Pugno N M, Taniguchi T, Watanabe K, Ferrari A C and Lombardo A 2018 Cleaning interfaces in layered materials heterostructures *Nat Commun* **9**

[187] Mayorov A S, Gorbachev R v., Morozov S v., Britnell L, Jalil R, Ponomarenko L A, Blake P, Novoselov K S, Watanabe K, Taniguchi T and Geim A K 2011 Micrometer-scale ballistic transport in encapsulated graphene at room temperature *Nano Lett* **11** 2396–9

[188] Joshi P, Romero H E, Neal A T, Toutam V K and Tadigadapa S A 2010 Intrinsic doping and gate hysteresis in graphene field effect devices fabricated on SiO2 substrates *Journal of Physics Condensed Matter* **22**

[189] Fan X F, Zheng W T, Shen Z X and Kuo J-L *Interaction between graphene and SiO 2 surface*

[190] Nistor R A, Kuroda M A, Maarouf A A and Martyna G J 2012 Doping of adsorbed graphene from defects and impurities in SiO 2 substrates *Phys Rev B Condens Matter Mater Phys* **86**

[191] Goniszewski S, Adabi M, Shaforost O, Hanham S M, Hao L and Klein N 2016 Correlation of p-doping in CVD Graphene with Substrate Surface Charges *Sci Rep* **6**

[192] Costa S D, Weis J E, Frank O, Fridrichová M and Kalbac M 2016 Monitoring the doping of graphene on SiO2/Si substrates during the thermal annealing process *RSC Adv* **6** 72859–64

[193] Lee D, Ahn G and Ryu S 2014 Two-dimensional water diffusion at a graphene-silica interface *J Am Chem Soc* **136** 6634–42

[194] Mcgrail B P, Engelhard M H, Icenhower J P, Steele J L, Darab J G, Rodriguez E A, Shuh D K, Liu P, Baer D R, Ivanov K E, Shutthanandan V, Booth C H, Thevuthasan S and Nachimuthu P 2001 *Ion-Exchange Processes and Mechanisms in Glasses*

[195] Patschger M and Rüssel C 2015 Sodium/potassium ion exchange of a soda–lime–silica float glass: mechanical strength, hardness, stress profile and thickness of the ion exchanged layer *Glass Technology - European Journal of Glass Science and Technology Part A* **56** 163–70

[196] Paradisi A, Biscaras J and Shukla A 2015 Space charge induced electrostatic doping of two-dimensional materials: Graphene as a case study *Appl Phys Lett* **107**

[197] Brenner K and Murali R 2010 Single step, complementary doping of graphene *Appl Phys Lett* **96**

[198] Fang Z, Thongrattanasiri S, Schlather A, Liu Z, Ma L, Wang Y, Ajayan P M, Nordlander P, Halas N J and García De Abajo F J 2013 Gated tunability and hybridization of localized plasmons in nanostructured graphene *ACS Nano* **7** 2388–95

[199] Jablan M, Buljan H and Soljačić M 2009 Plasmonics in graphene at infrared frequencies *Phys Rev B Condens Matter Mater Phys* **80**

[200] Fang Z, Wang Y, Schlather A E, Liu Z, Ajayan P M, García De Abajo F J, Nordlander P, Zhu X and Halas N J 2014 Active tunable absorption enhancement with graphene nanodisk arrays *Nano Lett* **14** 299–304

[201] Thongrattanasiri S, Koppens F H L and García De Abajo F J 2012 Complete optical absorption in periodically patterned graphene *Phys Rev Lett* **108**

[202] Leyland N S, Podporska-Carroll J, Browne J, Hinder S J, Quilty B and Pillai S C 2016 Highly Efficient F, Cu doped TiO2 anti-bacterial visible light active photocatalytic coatings to combat hospital-acquired infections *Sci Rep* **6**

[203] Valenzuela L, Iglesias A, Faraldos M, Bahamonde A and Rosal R 2019 Antimicrobial surfaces with self-cleaning properties functionalized by photocatalytic ZnO electrosprayed coatings *J Hazard Mater* **369** 665–73

[204] Anon Antimicrobial Corning® Gorilla® Glass

[205] Borrelli N F, Senaratne W, Wei Y and Petzold O 2015 Physics and chemistry of antimicrobial behavior of ion-exchanged silver in glass *ACS Appl Mater Interfaces* **7** 2195–201

[206] Available from: http://www.kastus.com/. 2021 Kastus. Visible light-activated light material. Kastus.

[207] Siedenbiedel F and Tiller J C 2012 Antimicrobial polymers in solution and on surfaces: Overview and functional principles *Polymers (Basel)* **4** 46–71

[208] Mitra D, Li M, Kang E T and Neoh K G 2019 Transparent Copper-Based Antibacterial Coatings with Enhanced Efficacy against Pseudomonas aeruginosa *ACS Appl Mater Interfaces* **11** 73–83

[209] Behzadinasab S, Williams M D, Hosseini M, Poon L L M, Chin A W H, Falkinham J O and Ducker W A 2021 Transparent and Sprayable Surface Coatings that Kill Drug-Resistant Bacteria Within Minutes and Inactivate SARS-CoV-2 Virus *ACS Appl Mater Interfaces* acsami.1c15505

[210] Gentili V, Pazzi D, Rizzo S, Schiuma G, Marchini E, Papadia S, Sartorel A, di Luca D, Caccuri F, Bignozzi C A and Rizzo R 2021 Transparent Polymeric Formulations Effective against SARS-CoV-2 Infection *ACS Appl Mater Interfaces* **13** 54648–55

[211] Varghese S, ElFakhri S O, Sheel D W, Sheel P, Bolton F J E and Foster H A 2013 Antimicrobial activity of novel nanostructured Cu-SiO2 coatings prepared by chemical vapour deposition against hospital related pathogens *AMB Express* **3**

[212] Mitra D, Kang E T and Neoh K G 2020 Antimicrobial Copper-Based Materials and Coatings: Potential Multifaceted Biomedical Applications *ACS Appl Mater Interfaces* **12** 21159–82

[213] Mitra D, Li M, Kang E T and Neoh K G 2017 Transparent Copper-Loaded Chitosan/Silica Antibacterial Coatings with Long-Term Efficacy *ACS Appl Mater Interfaces* **9** 29515–25

[214] Raghunath A and Perumal E 2017 Metal oxide nanoparticles as antimicrobial agents: a promise for the future *Int J Antimicrob Agents* **49** 137–52

[215] Kim Y H, Lee D K, Cha H G, Kim C W, Kang Y C and Kang Y S 2006 Preparation and characterization of the antibacterial Cu nanoparticle formed on the surface of SiO2 nanoparticles *Journal of Physical Chemistry B* **110** 24923–8

[216] Saif M J, Anwar J and Munawar M A 2009 A novel application of quaternary ammonium compounds as antibacterial hybrid coating on glass surfaces *Langmuir* **25** 377–9

[217] Ylitalo Caroline M, Mahfuza Ali B, Walker Christopher B, Jr Gerald R, Hofmann A, Scholtz Matthew T, Pocius Alphonsis V and Olson Linda K M 2006 Antimicrobial adhesive films (Patent)

[218] 3M 3M United States. 3M^{TM} durable protective film 7750AM.

[219] Cao Y, Su B, Chinnaraj S, Jana S, Bowen L, Charlton S, Duan P, Jakubovics N S and Chen J 2018 Nanostructured titanium surfaces exhibit recalcitrance towards Staphylococcus epidermidis biofilm formation *Sci Rep* **8**

[220] Sibilo R, Mannelli I, Reigada R, Manzo C, Noyan M A, Mazumder P and Pruneri V 2020 Direct and Fast Assessment of Antimicrobial Surface Activity Using Molecular Dynamics Simulation and Time-Lapse Imaging *Anal Chem* **92** 6795–800

[221] NBD Technologies InvisiPrint® MBED

[222] Corning Incorportated ANTIMICROBIAL CORNING® GORILLA® GLASS

[223] Pilkington Pilkington SaniTise™

[224] Chan C M N, Cheng H S, Djurišić A B, Ng A M C, Leung F C C and Chan W K 2011 Multicomponent antimicrobial transparent polymer coatings *J Appl Polym Sci* **122** 1572–8

[225] Hosseini M, Chin A W H, Williams M D, Behzadinasab S, Falkinham J O, Poon L L M and Ducker W A 2022 Transparent Anti-SARS-CoV-2 and Antibacterial Silver Oxide Coatings *ACS Appl Mater Interfaces* **14** 8718–27

[226] Varghese S, Elfakhri S, Sheel D W, Sheel P, Bolton F J and Foster H A 2013 Novel antibacterial silver-silica surface coatings prepared by chemical vapour deposition for infection control *J Appl Microbiol* **115** 1107–16

[227] Jampa S, Ratanatawanate C, Pimtong W, Aueviriyavit S, Chantho V, Sillapaprayoon S, Kunyanee C, Warin C, Gamonchuang J and Kumnorkaew P 2022 Transparent Anti-SARS COV-2 Film from Copper(I) Oxide Incorporated in Zeolite Nanoparticles *ACS Appl Mater Interfaces*

[228] das Jana I, Kumbhakar P, Banerjee S, Gowda C C, Kedia N, Kuila S K, Banerjee S, Das N C, Das A K, Manna I, Tiwary C S and Mondal A 2021 Copper Nanoparticle-Graphene Composite-Based Transparent Surface Coating with Antiviral Activity against Influenza Virus *ACS Appl Nano Mater* **4** 352–62

[229] Zhou Y, Fletcher N F, Zhang N, Hassan J and Gilchrist M D 2021 Enhancement of Antiviral Effect of Plastic Film against SARS-CoV-2: Combining Nanomaterials and Nanopatterns with Scalability for Mass Manufacturing *Nano Lett* **21** 10149–56

[230] Lee S B, Koepsel R R, Morley S W, Matyjaszewski K, Sun Y and Russell A J 2004 Permanent, nonleaching antibacterial surfaces, 1.

Synthesis by atom transfer radical polymerization *Biomacromolecules* **5** 877–82

[231] Anon E. P. A. Press Office

[232] Mahmoodi S, Elmi A and Hallaj Nezhadi S 2018 Copper Nanoparticles as Antibacterial Agents *J Mol Pharm Org Process Res* **06**

[233] Wang S, Zhu W, Yu P, Wang X, He T, Tan G and Ning C 2015 Antibacterial nanostructured copper coatings deposited on tantalum by magnetron sputtering *Materials Technology* **30** B120–5

[234] Bharadishettar N, Bhat K U and Panemangalore D B 2021 Coating technologies for copper based antimicrobial active surfaces: A perspective review *Metals (Basel)* **11**

[235] Scully. R J 2020 The COVID-19 Pandemic, Part 1:Can antimicrobial copper-based alloys help suppress infectious transmission of viruses originating from human Contact with high-touch surfaces? *Corrosion* **76** 524–7

[236] Nakhaie D, Williams T C, Velapatino B, Bryce E A, Charles M K, Asselin E and Clifford A M 2022 An Engineered Nanocomposite Copper Coating with Enhanced Antibacterial Efficacy *Adv Mater Interfaces* 2201009

[237] Bogdanović U, Vodnik V, Mitrić M, Dimitrijević S, Škapin S D, Žunič V, Budimir M and Stoiljković M 2015 Nanomaterial with high antimicrobial efficacycopper/polyaniline nanocomposite *ACS Appl Mater Interfaces* **7** 1955–66

[238] Lex J R, Koucheki R, Stavropoulos N A, Michele J di, Toor J S, Tsoi K, Ferguson P C, Turcotte R E and Papagelopoulos P J 2022 Megaprosthesis anti-bacterial coatings: A comprehensive translational review *Acta Biomater* **140** 136–48

[239] Ning C, Wang X, Li L, Zhu Y, Li M, Yu P, Zhou L, Zhou Z, Chen J, Tan G, Zhang Y, Wang Y and Mao C 2015 Concentration Ranges of

Antibacterial Cations for Showing the Highest Antibacterial Efficacy but the Least Cytotoxicity against Mammalian Cells: Implications for a New Antibacterial Mechanism *Chem Res Toxicol* **28** 1815–22

[240] Valko M, Morris H and Cronin M T D 2005 *Metals, Toxicity and Oxidative Stress* vol 12

[241] Angelé-Martínez C, Nguyen K V T, Ameer F S, Anker J N and Brumaghim J L 2017 Reactive oxygen species generation by copper(II) oxide nanoparticles determined by DNA damage assays and EPR spectroscopy *Nanotoxicology* **11** 278–88

[242] Yoon K Y, Hoon Byeon J, Park J H and Hwang J 2007 Susceptibility constants of Escherichia coli and Bacillus subtilis to silver and copper nanoparticles *Science of the Total Environment* **373** 572–5

[243] Chatterjee A K, Chakraborty R and Basu T 2014 Mechanism of antibacterial activity of copper nanoparticles *Nanotechnology* **25**

[244] Grass G, Rensing C and Solioz M 2011 Metallic copper as an antimicrobial surface *Appl Environ Microbiol* **77** 1541–7

[245] Anon Daikin Chemicals

[246] Anon United States Environmental Protection Agency - Test Method for Efficacy of Copper Alloy Surfaces as a Sanitizer (United States Environmental Protection Agency, Washington DC, 2008).

[247] Toparli C, Hieke S W, Altin A, Kasian O, Scheu C and Erbe A 2017 State of the Surface of Antibacterial Copper in Phosphate Buffered Saline *J Electrochem Soc* **164** H734–42

[248] Luo J, Hein C, Pierson J F and Mücklich F 2019 Early-stage corrosion, ion release, and the antibacterial effect of copper and cuprous oxide in physiological buffers: Phosphate-buffered saline vs Na-4-(2-hydroxyethyl)-1-piperazineethanesulfonic acid *Biointerphases* **14**

[249] Michels H T, Noyce J O and Keevil C W 2009 Effects of temperature and humidity on the efficacy of methicillin- resistant

Staphylococcus aureus challenged antimicrobial materials containing silver and copper *Lett Appl Microbiol* **49** 191–5

[250] Tarrant E, Riboldi G, McIlvin M R, Stevenson J, Barwinska-Sendra A, Stewart L J, Saito M A and Waldron K J 2019 Copper stress in Staphylococcus aureus leads to adaptive changes in central carbon metabolism *Metallomics* **11** 183–200

[251] McDonald M, Wesgate R, Rubiano M, Holah J, Denyer S P, Jermann C and Maillard J Y 2020 Impact of a dry inoculum deposition on the efficacy of copper-based antimicrobial surfaces *Journal of Hospital Infection* **106** 465–72

[252] Finney L A and O'halloran T v 2002 Transition Metal Speciation in the Cell: Insights from the Chemistry of Metal Ion Receptors *J. Appl. Crystallogr* **277** 869

APPENDIX

A

Table 7 Staphylococcus aureus CFU results for Set A and B **Figure 32** and **Figure 33**

Sample ID	**SiO_2 (nm)**	**Conditions**	**GeoMean (CFU/ml)**	**Standard Deviation**	**LR**
Ctrl Glass coverslip	-	-	5.22×10^5	1.4×10^5	-
Ctrl Steel	-	-	5.37×10^5	1.6×10^5	-0.01
Cu metal	-	-	20	0	4.42
SET A (50 W O_2 Plasma, 2 minutes)					
1-A	20	As rcd	20	0	4.42
2-A	25	As rcd	20	0	4.42
3-A	30	As rcd	20	0	4.42
4-A	35	As rcd	20	0	4.42
5-A	50	As rcd	20	0	4.42
6-A	20	0.012 % ETC	20	0	4.42
7-A	25	0.012 % ETC	20	0	4.42
8-A	30	0.012 % ETC	20	0	4.42
9-A	35	0.012 % ETC	20	0	4.42
10-A	50	0.012 % ETC	6.32	4.24	3.92
11-A	35	0.024 % ETC	1650	0	2.50
12-A	50	0.024 % ETC	4.15×10^4	0	1.10
SET B (300 W O_2 Plasma, 5 minutes)					
1-B	0	As rcd	27.4	0	4.28
2-B	10	As rcd	28.7	0	4.26
3-B	15	As rcd	35.3	0	4.17
4-B	15	0.005 % ETC	131	0	3.6
5-B	25	0.005 % ETC	34.5	0	4.18
6-B	0	0.012 % ETC	52.2	0	4
7-B	10	0.012 % ETC	886	0	2.77
8-B	15	0.012 % ETC	4150	0	2.1
9-B	25	0.012 % ETC	1.09×10^4	0	1.68
10-B	10	0.024 % ETC	2.94×10^4	0	1.25
11-B	15	0.024 % ETC	3.53×10^4	0	1.17

Appendix

AM calculations

The inoculum has a concentration of $5.22\text{x}10^5$ CFU/ml = 522 CFU/µL
If 20 µL of inoculum is used for each coupon it gives 20x1780 = **10400 CFUs per coupon**

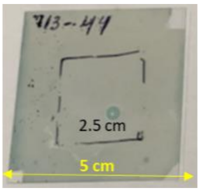

Volume of Cu in test area = Test area x thickness of Cu deposited
= $2.5\ \text{cm}^2 \times 3.5\text{x}10^{-7}$ cm
= $8.75\text{x}10^{-7}\ \text{cm}^3$ of Cu

Total Mass of Cu in test area = density of Cu x volume of Cu
= $8.96\ \text{g/cm}^3 \times 8.75\text{x}10^{-7}\ \text{cm}^3$
=$7.84\ \text{x}10^{-6}$ g Cu per coupon

<u>Inductively coupled mass spectroscopy (ICP-MS) results</u>

<u>Procedure:</u>

1. 20uL of PBS was pipetted onto the test area of 2.5 cm^2.
2. After 2 hours 2x150uL of PBS was used to wash the leachate from the coating.
3. The total Cu content in the leachate and wash (total volume of 320 µL) was determined by ICP-MS.

<u>Calculation of mass of Cu in leachate and % Cu leached:</u>

$$\text{Mass (g) of Cu in leachate} = \frac{c}{v} \qquad \text{(Eq. 1)}$$

c is [Cu] in g/L
v is total volume (L) (leachate + wash = 20uL + 300uL)

$$\%\ \text{Cu mass leached} = 100^* \left(\frac{\text{Cu mass in leachate}}{\text{Total Cu mass deposited}}\right) \qquad \text{(Eq. 2)}$$

Example 1 : 50 nm SiO_2 + ETC (S_1123) 3.41 ppm (mg/L) Cu ions released into 320µL PBS gives:

Mass = 0.00341 g/L x 320×10^{-6} L = 1.09×10^{-6} g of Cu
% mass leached = 100*(1.09×10^{-6} g / 7.84 $\times10^{-6}$ g) = 13.9 %

***Example 2**:* 25 nm SiO_2 + ETC (S_1096): 12.9 ppm (mg/L) Cu ions released into 320µL PBS:

Mass = 0.0129 g/L x 320×10^{-6} L = 4.13×10^{-6} g of Cu
% mass leached = 100*(4.13×10^{-6} g / 7.84 $\times10^{-6}$ g) = 52.7%

Example 3: 20 nm SiO2 + ETC (S_1101) 16 ppm (mg/L) Cu ions released into 320µL PBS gives

Mass = 0.016 g/L x 320×10^{-6} L = 7.84 $\times10^{-6}$ g of Cu
%mass leached = 100*(5.12×10^{-6} g / 7.84 $\times10^{-6}$ g) **=** 65.1%

<u>**AM efficacy calculations:**</u>

Example Sample 6-A:

Geo Mean of glass coverslip control survivors= control glass = 5.22 $\times10^{5}$

Geo Mean of TANC survivors = 20

$$LR_{TANC} = \text{Log}\left(\frac{5.22\ \text{x}10^{5}}{20}\right) = 4.42$$

$$\%\ \text{reduction} = \left(\frac{5.22\ \text{x}10^{5}-20}{5.22\ \text{x}10^{5}}\right)\text{x}\ 100 = 99.99\%$$